Dissertation on

Calibration, Validation and Polarimetry in 2D Aperture Synthesis: Application to MIRAS

Serni Ribó Vedrilla

So eine Arbeit wird eigentlich nie fertig, man muß sie für fertig erklären, wenn man nach Zeit und Umständen das möglichste getan hat.

Johann Wolfgang Goethe

Dedicat a la Maria

Acknowledgements

Contents

List of Figures

List of Tables

Acronyms

2D-STAR . . . . 2-dimensional version of ESTAR

A/D . . . . Analog to Digital

ASTRON/NFRA . . . . . Stichting ASTRonomisch Onderzoek in Nederland /
  Netherlands Foundation for Research in Astronomy

CAS . . . . CAlibration System

CIP . . . . Correlated noise Input Port

DICOS . . . . DIgital COrrelator System

DICOS-2 . . . . DIgital COrrelator System of second generation

DICOS-3 . . . . DIgital COrrelator System of third generation

DFT . . . . Discrete Fourier Transform

EADS-CASA . . . . European Aeronautic Defence and Space company –
  Construcciones Aeronáuticas S.A.

EGSE . . . . Electrical Ground Support Equipment

EMSR . . . . Electrical Scanning Microwave Radiometer

ENR . . . . Excess Noise Ratio

ESA . . . . European Space Agency

ESTAR . . . . Electronically Steered Thinned Array Radiometer

ESTEC . . . . European Space Research and Technology Centre

FPGA . . . . .Field Programmable Gate Array

FWF . . . . .Fringe-Washing Function

GeoSTAR . . . . . . Geostationary atmospheric sounder Steered Thinned Array
    Radiometer

GPS . . . . Global Positioning System

HIP . . . . .Horizontal polarisation Input Port

HUT . . . . Helsinki University of Technology

HUT-2D . . . . .2-dimensional aperture synthesis radiometer of LST/HUT

IEEC . . . . .Institut d'Estudis Espacials de Catalunya

IF . . . . .Intermediate Frequency

IIQI . . . . .Complex correlation obtained with nominal real correlations

IPPC . . . . Intergovernmental Pannel for Climate Change

IV-3B . . . . .Image Validation test 3B

LICEF . . . . .LIght Cost Effective Front-end (the receivers of MIRAS)

LICEF-1 . . . . .LICEF receiver of first generation

LICEF-2 . . . . LICEF receiver of second generation

LST . . . . Laboratory of Space Technology

MDPP-3 . . . . MIRAS Demonstrator Pilot Project 3

MIRAS . . . . Microwave Imaging Radiometer using Aperture Synthesis

NDN . . . . Noise Distribution Network

NIR . . . . .Noise Injection Radiometer

PC . . . . .Personal Computer

PMS . . . . .Power Measurement System

RF . . . . Radio Frequency

QQIQ . . . . Complex correlation obtained with redundant real correlations

SAM . . . . Small Airborne MIRAS

SMOS . . . . Soil Moisture and Ocean Salinity Mission of ESA

TEC . . . . Total Electron Content

TOA . . . . Top Of the Atmosphere

UPC . . . . Universitat Politècnica de Catalunya

UT . . . . Universal Time

VIP . . . . Vertical polarisation Input Port

VLA . . . . Very Large Array

VTEC . . . . Vertical Total Electron Content

WSRT . . . . Westerbork Synthesis Radio Telescope

Chapter 1

Introduction

Many scientists throughout the world are studying the human induced climate change. This climate change is primarily due to the massive and continuous emission of greenhouse gases into the atmosphere, which are changing its chemical composition. In 2001 the Intergovernmental Panel for Climate Change (IPCC) published the third Assessment Report [1], where the work of the scientific community on climate research was collected, showing the scientific basis of the human induced climate change. This report also states that more observations are needed in order to *address the remaining gaps in information and understanding*. The measurement and monitoring of Soil Moisture and Ocean Salinity at global scale are crucial variables that will further improve the understanding of climate monitoring, weather and extreme events forecasting [2].

It is well known that ocean currents regulate our climate through the transport of heat together with important water masses. The Gulf stream transports heat through surface water from the equator to higher latitudes. This water cools during its way to the North increasing its density. Furthermore, evaporation will increase the surface salinity, increasing also its density. At a certain density the surface water will sink to the deep ocean. The water masses will return to the equator at the bottom of the ocean. This is known as *thermohaline circulation*. Additionally, ocean surface salinity is also related to net evaporation (evaporation-precipitation) and thus an indirect measurement of precipitation over the ocean. Sea surface salinity is thus a key variable for studying and modelling ocean circulation and precipitation, which is an important indicator for climate change. [3]

Soil Moisture is a key variable in the water cycle. It changes with time and

is governed by different factors such as the amount of precipitation, evaporation or absorption by the vegetation cover. The properties of the soil determine the amount of water that can be stored determining also plant growth and thus food supplies. Soil moisture is also a key parameter for climate as it influences temperature, evaporation and vegetation in its close environment. [4].

SMOS mission

The Soil Moisture and Ocean Salinity Mission (SMOS) of the European Space Agency (scheduled 2007) is devoted to measure these two key parameters. The single instrument of this mission is the MIRAS (Microwave Imaging Radiometer using Aperture Synthesis), a new kind of instrument devoted to Earth observation. It is a thinned Y-shaped array with 21 elements per arm. With this technique a large synthetic aperture antenna with relative low weight can be obtained. This novel technique has been selected in order to fulfil both criteria ground resolution (35-50km) and revisit time (3 days). The ground resolution is obtained using the synthetic aperture, which results in a narrower synthetic main beam of the antenna. The small revisit time is obtained with a broad observation swath, obtained with the imaging properties of MIRAS.

Similar instruments to MIRAS have already been used for radio astronomy but in that case only sources with a narrow angular size (stars and galaxies) were observed. In the case of MIRAS, the Earth is an extended source of thermal radiation, which almost fills up the complete field of view of MIRAS. The consequence of it is that the calibration techniques developed for radio astronomy may not be used in the SMOS mission [5].

Focus of the thesis

This thesis is mainly focused to experimentally test several calibration techniques and to prove the imaging properties of MIRAS. A second part is devoted to the polarimetric mode of MIRAS and its capability to improve its performance.

Work at ESTEC

This thesis was started thanks to a two year grant (from summer 2000 to summer 2002) at the ESTEC centre of the European Space Agency in the Netherlands. During this time the first experimental campaigns aimed to test calibration methods and imaging capabilities of MIRAS were done. In these so called image validation tests a first MIRAS prototype was used. The planning, preparation, execution and data processing for different tests was done. The capability of the calibration methods was demonstrated, showing also in which direction further research should be undertaken in order to refine them. The imaging properties of MIRAS were also demonstrated with the measurement of its impulsional response. The most important results are presented here.

At the ESTEC centre theoretical work and simulations on polarimetric interferometry have also been done. This research contributed to the formulation of the polarimetric visibility function and the definition of the polarimetric op-

eration mode of MIRAS. Up to that time only the dual polarimetric operation mode had been defined. The dual mode of operation has the disadvantage of presenting non-invertible zones on its field of view, while the polarimetric mode solves this problem being invertible all over the field of view.

After the two years stage at ESTEC, the thesis was continued at the Labora- Work at HUT tory of Space Technology (LST) of the Helsinki University of Technology (HUT) for three months (August 2002 to October 2002), as an invited researcher. There the HUT-2D interferometric radiometer, an airborne demonstrator instrument for MIRAS, was being constructed. The experience gained in the previous campaigns was shared with the HUT-2D team and the calibration methods were tested in a different instrument, confirming the previous results.

In February 2003 this thesis was continued at the *Institut d'Estudis Espa-* Work at IEEC *cials de Catalunya (IEEC)* under a research contract of the Spanish ministry of research [1]. There the effect of Faraday rotation on MIRAS was studied. A solution for compensating it was proposed, making use of the polarimteric operation mode of MIRAS.

The thesis was continued at IEEC, designing and manufacturing the Electrical Ground Support Equipment (EGSE) of an airborne demonstrator of MIRAS, known as SAM (Small Airborne MIRAS). This work was done for ESA.[2] This instrument implements the complete calibration scheme with two-level noise injection, which is a refinement of the calibration schemes used in previous MIRAS prototypes. Preliminary experimental results of this novel calibration technique are also presented in this thesis.

1.1   Thesis Structure

This thesis has been structured in the following way. An introduction is given Thesis structure in chapter 1. Chapter 2 includes a brief historical summary of interferometric radiometers. Also the basic concepts of radiometry and a review of the interferometric equations upon which MIRAS is based are given.

Chapter 3 presents the calibration techniques of MIRAS. The equations that are used to calibrate MIRAS can be found. Chapter 4 is devoted to present the experimental validation of the calibration equations so as to asses their performance and propose advantages and drawbacks. The presented experimental results are

---

[1]Spanish research project number: EPS2001-4523-PE
[2]ESA contract number: 15138/01/NL/SF (CCN5)

- The most important calibration results of the Image Validation Campaigns done at Dwingeloo with the first MIRAS prototype.

- The most important calibration results with the HUT-2D segment.

- Preliminary results on calibration using SAM , which includes a comprehensive calibration procedure based on the results of the previous theoretical and experimental work.

The next two chapters are dedicated to polarimetry. Chapter 5 describes the polarimetric mode of MIRAS and demonstrates that it is superior respect to the dual mode of MIRAS with respect to the invertibility of the modified brightness temperature in the complete field of view. Chapter 6 follows with a proposal to correct the Faraday rotation using the polarimetric mode of MIRAS. In chapter 7 the conclusions are given.

Chapter 2

Interferometric Radiometry (IR) for Earth Observation

This chapter is aimed to briefly review the past, present and future of radiometers. It starts with the origins of radiometry and the evolution of the different sensor types, arriving to the most sophisticated ones, under which MIRAS, object of this thesis, can be found.

The chapter continues with an introduction to radiometry, followed by the review of interferometric equations which describe the fundamentals of MIRAS operation.

2.1 Past, Present and Future Interferometric Sensors

The fundamental equations of radiometry, where the blackbody emission equation is deduced, date back to the early 20th century. However, the firsts measurements were not done until the 1930s by Karl Jansky, while he was investigating the origin of interferences in radio voice transmission. With the 20.5MHz antenna that he built he discovered the radio emission of the centre of the galaxy [6].

The first one to build a radio telescope was Grote Reber in 1937. It was constructed in his backyard and at his own expense while working full time for a radio company. It consisted of a parabolic reflector of 9.5m diameter and a radio

History of radiometry

First radio telescope

receiver at the focus (about 6m above the reflector). He succeeded in making measurements at 160MHz [7] and making the first radio map of the galaxy. After the Second World War, with the technological legacy of radar development and with the incentive of Reber's results, radio astronomy experienced a spectacular growth.

In the Netherlands, under the leadership of Oort, a radio telescope with a dish of 25m came into operation in Dwingeloo in 1956. It operated at L-band and contributed to discovering the size, distribution and motion of neutral hydrogen in the Milky Way. At that time it was the largest radioastronomy antenna. Figure 2.1 shows the radio telescope together with a prototype of MIRAS during the Image Validation campaigns.

The use of arrays to improve the angular resolution came with the use of
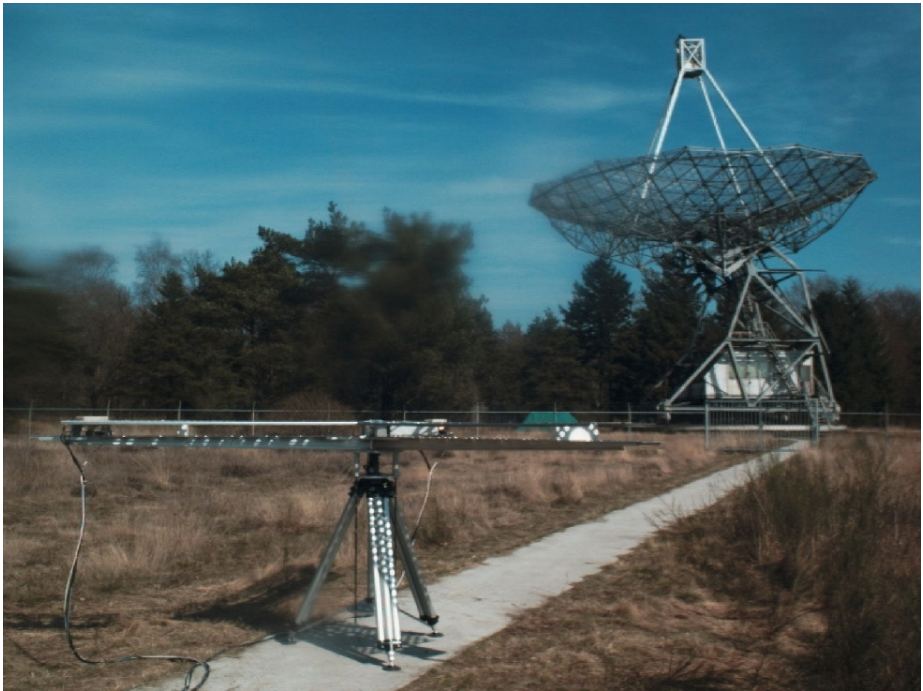
Figure 2.1: Dwingeloo 25m diameter radio telescope with MIRAS prototype in the front during the image validation campaigns of MIRAS.

the Mills Cross. Each arm of the cross produced a fan beam in the sky. By multiplying the two arms a pencil beam was formed. The beam could be steered in the sky by adjusting the phasing of the elements in each arm.

The use of aperture synthesis techniques was the solution to improve the angular resolution avoiding much larger real aperture antennæ. An example of it is the Westerbork Synthesis Radio Telescope (WSRT), which was designed and built in the 1960s. It came into operation in the 1970s and was for over a decade the most powerful. It is an east-west oriented linear array of fourteen dish antennæ with 25m diameters each (see figure 2.2). It makes use of the earth-rotation synthesis technique to increase its angular resolution.

Aperture synthesis

The natural evolution of interferometric arrays was to go a step further from 1-dimensional arrays to 2-dimensional. The maximum exponent of it is the Very Large Array (VLA) [8] in New Mexico, USA, which became fully operative in 1980. It consists of 27 dish antennæ with a diameter of 25m each. They are arranged in a Y-shaped configuration to give a resolution of an antenna 36km across, as seen in figure 2.3. The main advantage over earth-rotation synthesis radio telescopes like WSRT is that it did not need 24 hours to measure all the baselines.

At the beginning, radiometry was used to study extraterrestrial radio sources. It is in 1958 when the first paper with microwave radiometric measurements of terrestrial materials appears [9]. Straiton et al. present the results for measurements of water, grass, gravel, among others at 4.3mm wavelength.

Observing the Earth

Similar to the technological evolution of the instruments used to explore extraterrestrial radio sources, radiometric earth observation has also experienced the transition from real aperture instruments to more sophisticated 2-dimensional interferometric sensors, passing through 1-dimensional ones.

Planetary observation with space borne radiometers starts with the radiometer on board Mariner2 which gave the first close observations of Venus in 1962. The first radiometer measurements of the Earth were taken from the Soviet Cosmos 243 satellite in 1968. The Electrical Scanning Microwave Radiometer (EMSR) systems on board Nimbus5 and Nimbus6 (1970s) are of great importance in space borne radiometry as they gave the first synoptic images of microwave emission of the Earth [10]. Radiometric systems have been used extensively up to the present providing useful information for obtaining physical parameters or contributing to the calibration of other sensors.

Observations from Space

In general, space borne real aperture radiometer systems have a poor spatial resolution (order of kilometres) as their resolution is proportional to the aperture size of the antenna (order of meters) and they are far away from the Earth (hundreds of kilometres). A solution for obtaining larger antennæ for

Earth observation radiometric sensors is aperture synthesis, which was proposed by Ruf et al.[11, 12] in 1988. The result of it was the Electronically Steered Thinned Array Radiometer (ESTAR). Unfortunately, its airborne demonstrator instrument never succeeded in having a space borne version. Nevertheless, this first interferometric radiometer prototype provided extensive results (see for instance, [13, 14]), which proved the concept to be a promising new technique.

ESTAR is an L-band interferometric radiometer, designed for remote sensing of soil moisture. Real aperture antennæ (linear arrays of horizontally polarised

1-D
interferometry
from Space

Figure 2.2: Westerbork radio interferometer. Courtesy of ASTRON, http://www.astron.nl. Photo: Harm Jan Stiepel.

Figure 2.3: The Very Large Array in New Mexico. Image: NRAO/AUI/NSF.
http://www.nrao.edu

dipoles) determine the resolution along-track, while aperture synthesis is used
to obtain resolution across-track. The real antennæ are spaced at integer mul-
tiples of one-half wavelength, obtaining seven unique baselines plus one at zero
spacing. The resolution of the synthetic beam is about $\pm 4.5°$ (between first
nulls), while the resolution along-track at the 3dB point is about $9°$ [15]. A
new version of ESTAR, called 2D-STAR, which does aperture synthesis in two
dimensions and can measure in horizontal and vertical polarisations, is being
developed [16].

The launch of the Soil Moisture and Ocean Salinity (SMOS) mission of
ESA is planned for early 2007[1]. This opportunity mission aims at obtaining soil
moisture and ocean salintiy maps at global scale. The revisit time will be 3 days
and the best achievable spatial resolution 35-50km. The observations will be
done at L-band (1400-1427MHz); therefore, in order to have the desired ground

2-D
interferometry
from Space

---

[1]See http://www.esa.int

Figure 2.4: Artist's impression of MIRAS. Image: ESA, http://www.esa.int

resolution a large and heavy antenna would have to be used in space. This problem has been overcome by using the Microwave Imaging Radiometer using Aperture Synthesis (MIRAS), a 2-dimensional Y-shaped interferometer, which synthesises a large aperture with many small antennæ, reducing its physical size and weight. Figure 2.4 shows an artist impression of MIRAS and it can be observed that the arrangement of the antennæ is similar to the VLA. In MIRAS, however, the spacing between antennæ is much smaller in order to reduce in part

aliasing and to broaden the useful alias-free field of view. This thesis focuses on two aspects of this MIRAS instrument: its calibration procedure and its fully polarimetric operation.

Future interferometric radiometers for earth observation have also been proposed. An instrument that uses a similar approach as MIRAS, but at much higher frequencies (50GHz) is GeoSTAR [17]. It would be placed at geostationary orbit and used for atmospheric sounding.

2.2   Principles of Radiometry

The particles of every solid body are in constant vibrational motion respect to their mean position, involving an fixed amount of energy. The energy of each particle may be transferred to its neighbouring particle, changing its vibration states. The former will be now in a vibrational state with less energy, while the latter will have increased the energy of its vibrational state. The mean energy within the body will remain the same, as it has just been transferred from one particle to another one, being the temperature a measure of the mean vibrational energy within a body. In liquids or gases not only vibrational motion is present, furthermore rotational or kinetic energy is present, including the temperature concept also these kinds of energy.

<div style="text-align: right">**Definition of Temperature**</div>

The exchange of temperature of a body with its surroundings can happen in different ways. The simplest is exchanging the vibrational energy with its surrounding directly. Imagine a cup of hot tea. The tea particles (mainly water) have high kinetic energy as they are hot. They exchange their energy with the neighbouring particles transferring thus part of their energy to the cup particles. These vibrate now at higher vibrational levels, than before, while the water particles vibrate now with less, energy, The cup heats up, while the tea cools down. This kind of temperature exchange is known as *dissipation.*

<div style="text-align: right">**Energy exchange**</div>

At *absolute* zero temperature the exchange of energy between particles of a material is zero. All atoms are in its fundamental vibration state without exchanging energy among them.

Another kind of energy exchange is *thermal emission.* When the average vibrational energy after a collision between two particles is less than the average kinetic energy before it, the remaining energy is emitted as electro-magnetic energy, balancing out the energy budget. The hotter a body, the more energy will be involved in the collisions and thus, more electro-magnetic radiation will be emitted.

Electro-magnetic fields can travel long distances without being absorbed

as in the case of vacuum. When this radiation incides on another body, it will induce its particles to absorb the electric energy and transform it again to vibrational energy. Energy will have been transfered from one body to another one. Alternatively this electric fields, could be captured by an antenna and its intensity measured. This process of measuring the thermally emitted electromagnetic fields is known as *Radiometry*. It may be used for instance, to measure remotely the physical temperature of a body, by measuring the intensity of the emitted radiation.

Blackbody definition

In general, a part of the radiation incident upon the surface of a body (solid or liquid) is absorbed and the remainder is reflected. A *blackbody* is defined as an ideal body which does absorb all the incident radiation.[2] A blackbody is thus an ideal absorber. Blackbodies have also the property of being ideal emitters, as otherwise they would heat up infinitively, while absorbing more energy than emitting.

Planck's radiation law

A general description of the processes that are involved in the emission of thermal radiation can be found in [18] The spectrum and amount of radiation of a blackbody are related to its physical temperature through Planck's radiation law given by

$$B_f = \frac{2hf^3}{c^2} \left(\frac{1}{e^{hf/kT} - 1} \right) \tag{2.1}$$

with
$$
\begin{aligned}
B_f &= \text{Blackbody spectral brightness, } [\text{Wm}^{-2}\text{sr}^{-1}\text{Hz}^{-1}] \\
h &= \text{Planck's constant} = 6.63 \times 10^{-34} [\text{J s}] \\
f &= \text{Frequency, } [\text{Hz}] \\
k &= \text{Boltzmann's constant} = 1.38 \times 10^{-23} [\text{J K}^{-1}] \\
T &= \text{Absolute Temperature of the body, } [\text{K}] \\
c &= \text{Speed of light} = 3 \times 10^8 [\text{m s}^{-1}]
\end{aligned}
$$

The spectral brightness is the amount of energy radiated in a second, per square meter, per stereo radian and per Hertz. Figure 2.5 shows the spectral brightness as a function of frequency, for different temperatures of the blackbody.

Rayleigh-Jeans Law

In the microwave frequency range Planck's radiation law can be simplified by using the approximation

$$
\begin{aligned}
e^x - 1 &= \left(1 + x + \frac{x^2}{2} + \ldots \right) - 1 \\
&\approx x \qquad \text{for} \quad x \ll 1
\end{aligned}
$$

---

[2]The term *blackbody* has been taken from the fact that a body that absorbs all visible radiation appears to our eyes as black.
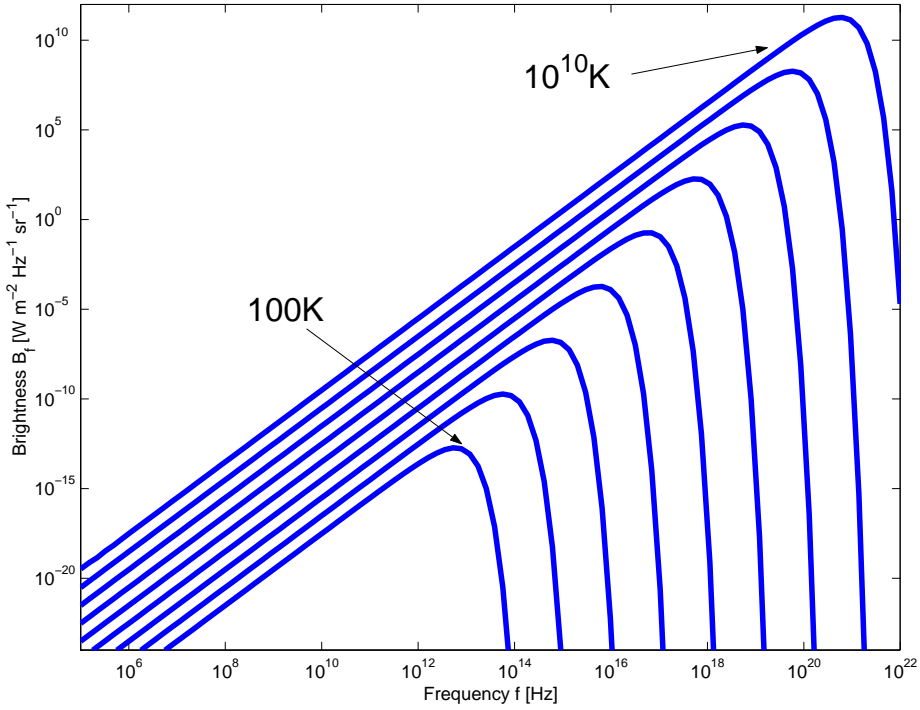
Figure 2.5: Planck's radiation-law curves.

For the case where $hf/kT \ll 1$ equation (2.1) can be approximated with the Rayleigh-Jeans Law

$$B_f = \frac{2f^2 kT}{c^2} = \frac{2kT}{\lambda^2} \tag{2.2}$$

The relationship between the physical temperature of the blackbody and the emitted power can obtained computing the available power of an antenna which has been placed inside a blackbody enclosure.

$$P_{bb} = \frac{1}{2} A_r \int_f^{f+\Delta f} \iint_{4\pi} \frac{2kT}{\lambda^2} F_n(\theta, \phi) \, \mathrm{d}\Omega \mathrm{d}f \tag{2.3}$$

P_{bb} is the available power at the antenna terminals, the factor $\frac{1}{2}$ appears because the antenna measures only in one polarisation, A_r is the effective aperture of the

antenna and $F_n(\theta, \phi)$ is the normalised radiation pattern. For an increment of frequency Δf where B_f is kept almost constant the equation can be rewritten as

$$P_{bb} = kT\Delta f \frac{A_r}{\lambda^2} \iint_{4\pi} F_n(\theta, \phi) \, \mathrm{d}\Omega \qquad (2.4)$$

and knowing that

$$\iint_{4\pi} F_n(\theta, \phi) \, \mathrm{d}\Omega = \Omega_P = \frac{\lambda^2}{A_r} \qquad (2.5)$$

where Ω_P is the antenna pattern solid angle. Equation (2.4) becomes

$$P_{bb} = kT\Delta f \qquad (2.6)$$

Equation (2.6) is of great importance in microwave radiometry as it shows a direct relationship between the physical temperature T of a blackbody and the emitted power P_{bb}.

Brigthness temperature and emissivity   A blackbody in fact an ideal abstraction of reality. Real bodies do not absorb all the incident power. They absorb just one fraction of it and absorb the rest. They are called grey bodies. The brightness temperature $T_B(\theta, \phi)$ of a material is defined as

$$T_B(\theta, \phi) = e(\theta, \phi) T \qquad (2.7)$$

where $0 \leq e(\theta, \phi) \leq 1$ is the emissivity. The brightness temperature of a grey body expresses its emission properties (with angular dependence) compared to blackbody. That is, the equivalent brightness is the temperature that the grey body would have, it was a blackbody radiating the same amount of power. The brightness temperature is always smaller or equal to its physical temperature. The emissivity expresses how close to a blackbody the material is: the higher the emissivity the closer is the behaviour to a blackbody.

The emissivity e is related to the reflectivity r through

$$e + r = 1 \qquad (2.8)$$

being the reflectivity the quotient between the reflected power on a surface and the incident power onto it.

Elemental radiometer   The basic concept of a radiometers consist of a real aperture antenna, a tune radio receiver and a power detector, as shown in figure 2.6. The antenna captures the RF-power emitted by the observed material, a low noise RF amplifier increases the power of the acquired noise signal. The bandpass filter selects the desired band Δf, which is then down converted at the mixer. The signal is amplified again before being detected by a square law detector. Finally a low
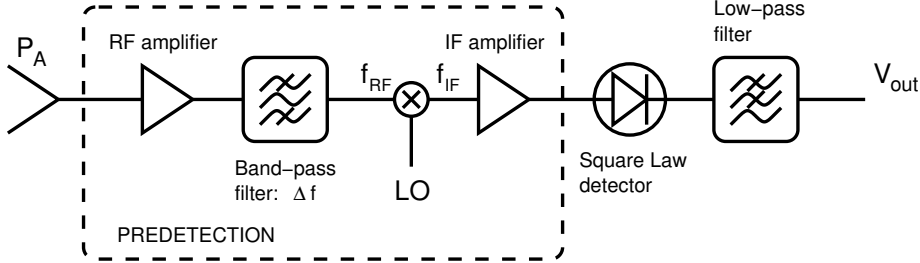
Figure 2.6: Basic arquitecture of a total power radiometer.

pass filter is used to average the obtained voltage, which is proportional to the system noise temperature. In a total power radiometer we have that the output voltage is proportional to the system noise temperature

$$V_{out} = kT_{sys}B \qquad (2.9)$$

being $T_{sys} = T_A + T_R$, with T_A the equivalent noise temperature captured by the antenna, T_R the receiver noise temperature and B the bandwidth of the receiver. The sensitivity of such a radiometer is given by

$$\Delta T = \frac{T_{sys}}{\sqrt{B\tau}} = \frac{T_A + T_R}{\sqrt{B\tau}} \qquad (2.10)$$

where τ is the time constant of the low pass filter after the square law detector.

2.3 Principles of Interferometry

The operation principles of a radiometric interferometer like MIRAS have been thoroughly revised in [19, 20] and are summarised in this section. In the previous section it has been said that radiometry deals with the measurement of the power of emitted radiation. Interferometry additionally deals with the measurement of the *phase information* of this radiation. Usually this is done by computing the cross-correlation between the signals acquired by two or more antennæ.

Let us have two antennæ placed on the xy-plane of the Σ reference frame pointing towards the z axis as it is shown in figure 2.7. The electric field expressed in the Σ' reference frame $d\vec{\mathbf{E}}(t; \theta', \phi')$ radiated by an elemental surface da in the (θ', ϕ') direction induces an elemental voltage $d\mathbf{v}^v(t)$ at the output of

Elemental voltages
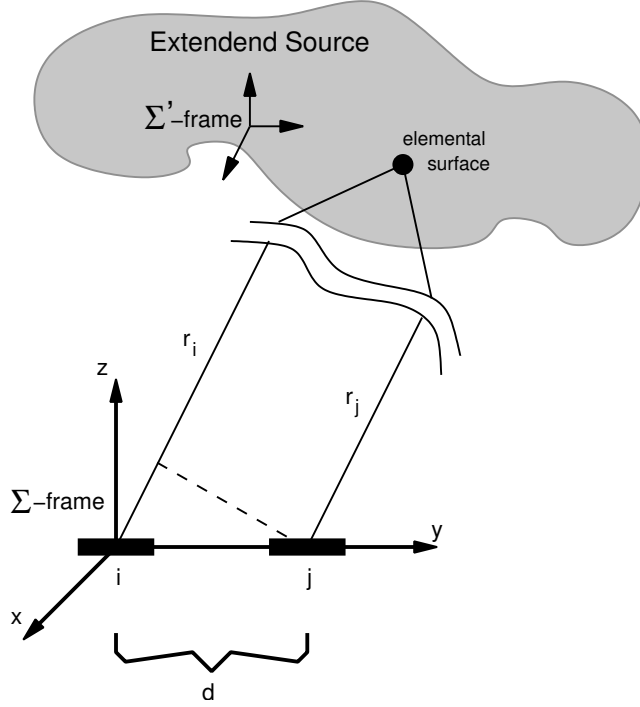
Figure 2.7: Elemental interferometer setup.

the vertical antenna probe. This voltage is given by

$$d\mathbf{v}^v\left(t\right) = \sqrt{\frac{\lambda_0^2}{4\pi}G_0^v}F_n^v(\theta,\phi)\ \hat{L}_e^v(\theta,\phi)\cdot d\vec{\mathbf{E}}\left(t;\theta',\phi'\right) \tag{2.11}$$

if the antenna is connected to a matched load. G_0^v is the maximum power gain, $F_n^v\left(\theta,\phi\right)$ the normalised voltage radiation pattern and $\hat{L}_e^v\left(\theta,\phi\right)$ the effective length vector of the vertical antenna probe, the last two computed for the (θ,ϕ) direction.

The vertical (and horizontal) effective length unit vector are taken following Ludwig's third definition [21]

$$\hat{L}_e^v = \sin\left(\phi+n\pi\right)\hat{\theta} + \cos\left(\phi+n\pi\right)\hat{\phi} \tag{2.12}$$

$$\hat{L}_e^h = -\cos\left(\phi+n\pi\right)\hat{\theta} + \sin\left(\phi+n\pi\right)\hat{\phi} \tag{2.13}$$

where the $n\pi$ term represents sign ambiguity. In [20] is is shown that this sign ambiguity causes no problem in the complete mathematical development and it is thus irrelevant.

Directions (θ, ϕ) and (θ', ϕ') are the same but expressed in different frames. The first one in the antenna frame, the second one in the emission frame. Thus, (θ', ϕ') will be replaced by (θ, ϕ) as follows as they represent the same physical direction. r represents the distance between any elemental surface and any antenna of the array. This distance may be expressed in the antenna frame or in the emission frame having $r = r'$.

The antenna voltage at the output of the vertical and horizontal antenna probes induced not only by an elemental surface element, but by the whole scene is obtained by the integral sum of elementary voltages.

Antenna voltages

$$\mathbf{v}^v(t) = \int_{\text{all } d\mathbf{v}^v} d\mathbf{v}^v(t) = \sqrt{\frac{\lambda_0^2}{4\pi} G_0^v} \int_{\text{all } (\theta, \phi)} F_n^v(\theta, \phi) \; \hat{L}_e^v(\theta, \phi) \cdot d\vec{\mathbf{E}}(t; \theta, \phi)$$

(2.14)

$$\mathbf{v}^h(t) = \int_{\text{all } d\mathbf{v}^h} d\mathbf{v}^h(t) = \sqrt{\frac{\lambda_0^2}{4\pi} G_0^h} \int_{\text{all } (\theta, \phi)} F_n^h(\theta, \phi) \; \hat{L}_e^h(\theta, \phi) \cdot d\vec{\mathbf{E}}(t; \theta, \phi)$$

(2.15)

If we now compute the cross-correlation between the antenna voltages of two different antennæ denoted with i and j, at polarisations p and q respectively we have that

Cross-correlation of antenna voltages

$$\Gamma_{\mathbf{v}_i^p \mathbf{v}_j^q}(\tau) = \left\langle \mathbf{v}_i^p(t) \, \mathbf{v}_i^{p*}(t - \tau) \right\rangle \qquad (2.16)$$

can be written, taking into account equations (2.14) and (2.15), as

$$\Gamma_{\mathbf{v}_i^p \mathbf{v}_j^q}(\tau) = \frac{\lambda_0^2}{4\pi} \sqrt{G_{0,i}^p G_{0,j}^q} \int_{\text{all } (\theta_1, \phi_1)} \int_{\text{all } (\theta_2, \phi_2)} F_{n,i}^p(\theta_1, \phi_1) F_{n,j}^{q*}(\theta_2, \phi_2)$$

$$\left\langle \left[\hat{L}_e^p(\theta_1, \phi_1) \cdot d\vec{\mathbf{E}}(t; \theta_1, \phi_1) \right] \left[\hat{L}_e^q(\theta_2, \phi_2) \cdot d\vec{\mathbf{E}}^*(t - \tau; \theta_2, \phi_2) \right] \right\rangle \quad (2.17)$$

where (θ_1, ϕ_1) and (θ_2, ϕ_2) represent two different directions in the observed scene.

Since thermal noise generated at different source points is uncorrelated the double integral of (2.17) reduces to a single integral

$$\Gamma_{\mathbf{v}_i^p \mathbf{v}_j^q}(\tau) = \frac{\lambda_0^2}{4\pi} \sqrt{G_{0,i}^p G_{0,j}^q} \int_{\text{all } (\theta, \phi)} F_{n,i}^p(\theta_1, \phi_1) F_{n,j}^{q*}(\theta, \phi)$$

$$\left\langle \left[\hat{L}_e^p(\theta, \phi) \cdot d\vec{\mathbf{E}}(t; \theta, \phi) \right] \left[\hat{L}_e^q(\theta, \phi) \cdot d\vec{\mathbf{E}}^*(t - \tau; \theta, \phi) \right] \right\rangle \qquad (2.18)$$

The projections of the incident electric field $\mathrm{d}\vec{\mathbf{E}}$ along the effective length unit vectors can be written as

$$\mathrm{d}\mathbf{E}_i^p\left(t;\theta,\phi\right) \equiv \hat{L}_e^p\left(\theta,\phi\right)\cdot\mathrm{d}\vec{\mathbf{E}}_i\left(t;\theta,\phi\right) \tag{2.19}$$

$$\mathrm{d}\mathbf{E}_j^q\left(t;\theta,\phi\right) \equiv \hat{L}_e^q\left(\theta,\phi\right)\cdot\mathrm{d}\vec{\mathbf{E}}_j\left(t;\theta,\phi\right) \tag{2.20}$$

and (2.18) can be further simplified with

$$\Gamma_{\mathbf{v}_i^p\mathbf{v}_j^q}\left(\tau\right) = \frac{\lambda_0^2}{4\pi}\sqrt{G_{0,i}^p G_{0,j}^q}$$

$$\int_{\text{all }(\theta,\phi)} F_{n,i}^p(\theta_1,\phi_1)F_{n,j}^{q*}(\theta,\phi)\left\langle\mathrm{d}\vec{\mathbf{E}}_i^p\left(t;\theta,\phi\right)\mathrm{d}\vec{\mathbf{E}}_j^{q*}\left(t-\tau;\theta,\phi\right)\right\rangle \tag{2.21}$$

The distance from any particular source point to the two antennæ is designated with r_i and r_j respectively. The path difference r_{ij} will then be

$$r_{ij} = r_i - r_j \tag{2.22}$$

and the electric field at one antenna can be expressed in terms of the field on the other antenna (for the same polarisation) with the corresponding delay

$$\mathrm{d}\mathbf{E}_j^p\left(t;\theta,\phi\right) = \mathrm{d}\mathbf{E}_j^p\left(t+\frac{r_{ij}}{c};\theta,\phi\right) \tag{2.23}$$

The assumption that the separation of the antennæ d is much smaller than the distance of the radiometer to the source r

$$d \ll r \tag{2.24}$$

allows us to make use of the paraxial approximation. This assumption justifies to use the same r^2 term for all receivers in the denominator for the propagation losses of the electric field, which is implicitly expressed in (2.23). In the phase, it allows to treat the incidence field on both antennæ and originated at the same source point as being parallel rays. The assumption of (2.24) is true, as the antenna separation is of the order of centimetres, while the distance from the radiometer to the source, the earth in a space born mission, is of the order of hundreds of kilometres.

The cross-correlation inside the integral of (2.21) becomes the polarimetric correlation function of the electric field

$$\left\langle\mathrm{d}\mathbf{E}_i^p\left(t;\theta,\phi\right)\mathrm{d}\mathbf{E}_j^{q*}\left(t-\tau;\theta,\phi\right)\right\rangle =$$
$$= \left\langle\mathrm{d}\mathbf{E}_i^p\left(t;\theta,\phi\right)\mathrm{d}\mathbf{E}_i^q\left(t-\tau+\frac{r_{ij}}{c};\theta,\phi\right)\right\rangle = \mathbf{\Gamma}_{\mathrm{d}\mathbf{E}^p\mathrm{d}\mathbf{E}^q}\left(\tau-\frac{r_{ij}}{c};\theta,\phi\right) \tag{2.25}$$

and thus (2.21) can be rewritten as

$$\Gamma_{\mathbf{V}_i^p \mathbf{v}_j^q}(\tau) = \frac{\lambda_0^2}{4\pi}\sqrt{G_{0,i}^p G_{0,j}^q} \int_{\text{all }(\theta,\phi)} F_{n,i}^p(\theta_1,\phi_1)F_{n,j}^{q*}(\theta,\phi)\mathbf{\Gamma}_{\mathrm{d}\mathbf{E}^p\mathrm{d}\mathbf{E}^q}\left(\tau - \frac{r_{ij}}{c};\theta,\phi\right)$$
(2.26)

In this development it is implicitly assumed that the polarisation frame of the antenna probes is the same as polarisation frame at emission. This is not true in general. A conversion between the emission polarisation frame and the antenna polarisation frame has to be applied to the electric fields. As this is part of the thesis it has been omitted in this introductory part, but included in chapter 5. For the time being it is enough to related the correlation of antenna (or receiver) voltages to the electric fields at the antennæ. In chapter 5 the conversion from the antenna frame to the emission frame is explained.

The mutual coherency matrix is expressed in terms of the polarimetric cross-correlations of the infinitesimal electric field with

$$\left[\mathbf{J}^{ij}(\tau)\right] \equiv \left[\begin{array}{cc} \mathbf{J}_{hh}^{ij}(\tau) & \mathbf{J}_{hv}^{ij}(\tau) \\ \mathbf{J}_{vh}^{ij}(\tau) & \mathbf{J}_{vv}^{ij}(\tau) \end{array}\right] = \left[\begin{array}{cc} \mathbf{\Gamma}_{\mathrm{d}\mathbf{E}^h\mathrm{d}\mathbf{E}^h}^{ij}(\tau) & \mathbf{\Gamma}_{\mathrm{d}\mathbf{E}^h\mathrm{d}\mathbf{E}^h}^{ij}(\tau) \\ \mathbf{\Gamma}_{\mathrm{d}\mathbf{E}^h\mathrm{d}\mathbf{E}^h}^{ij}(\tau) & \mathbf{\Gamma}_{\mathrm{d}\mathbf{E}^h\mathrm{d}\mathbf{E}^h}^{ij}(\tau) \end{array}\right]$$
(2.27)

since

$$\left[\begin{array}{cc} \mathbf{\Gamma}_{\mathrm{d}\mathbf{E}^h\mathrm{d}\mathbf{E}^h}^{ij}(\tau) & \mathbf{\Gamma}_{\mathrm{d}\mathbf{E}^h\mathrm{d}\mathbf{E}^h}^{ij}(\tau) \\ \mathbf{\Gamma}_{\mathrm{d}\mathbf{E}^h\mathrm{d}\mathbf{E}^h}^{ij}(\tau) & \mathbf{\Gamma}_{\mathrm{d}\mathbf{E}^h\mathrm{d}\mathbf{E}^h}^{ij}(\tau) \end{array}\right] = \left\langle \begin{array}{c} \mathrm{d}\mathbf{E}_i^h(\tau) \\ \mathrm{d}\mathbf{E}_i^v(\tau) \end{array} \quad \mathrm{d}\mathbf{E}_i^h(t-\tau) \quad \mathrm{d}\mathbf{E}_i^h(t-\tau)^* \right\rangle$$
(2.28)

The coherency matrix of the fields emitted by a grey body in a 1Ω medium impedance is given by [20]

$$[\mathbf{J}(\tau)] = \frac{kT_{ph}}{\lambda_0^2}\frac{\mathrm{d}a}{r^2}\boldsymbol{\delta}_a(\tau)[e]$$
(2.29)

where $k = 1.38 \times 10^{-23} J/K$ is the Boltzmann constant, T_{ph} is the physical temperature, $\mathrm{d}a$ is the emitting infinitesimal element of area, r is its distance to the radiometer, $\boldsymbol{\delta}_a(\tau)$ is the analytic delta function and $[e]$ is the polarimetric spectral emissivity matrix

$$[e] = \left[\begin{array}{cc} e^H(\theta,\phi) & e^HV(\theta,\phi) \\ e^VH(\theta,\phi) & e^H(\theta,\phi) \end{array}\right]$$
(2.30)

The cross-correlation between receiver voltages can now be rewritten as

$$\Gamma_{\mathbf{v}_i^p \mathbf{v}_j^q}(\tau) = \frac{\lambda_0^2}{4\pi}\sqrt{G_{0,i}^p G_{0,j}^q} \int_{\text{all }(\theta,\phi)} F_{n,i}^p(\theta_1,\phi_1)F_{n,j}^{q*}(\theta,\phi)\mathbf{J}_{pq}\left(\tau - \frac{r_{ij}}{c};\theta,\phi\right)$$
(2.31)

and using the polarimetric emissivities as

$$\Gamma_{\mathbf{v}_i^p \mathbf{v}_j^q}(\tau) = \frac{k}{4\pi}\sqrt{G_{0,i}^p G_{0,j}^q} \int_0^{\pi/2} \int_0^{2\pi} F_{n,i}^p(\theta,\phi)F_{n,j}^{q*}(\theta,\phi)$$

$$\cdot T_{ph}(\theta,\phi)\,e^{pq}(\theta,\phi)\,\boldsymbol{\delta}_a\left(\tau - \frac{r_{ij}}{c}\right)\sin\theta\mathrm{d}\phi\mathrm{d}\theta \tag{2.32}$$

where the following solid angle relation has been used

$$\mathrm{d}\Omega = \sin\theta\mathrm{d}\phi\mathrm{d}\theta = \frac{\mathrm{d}a}{r^2} \tag{2.33}$$

The polarimetric cross-correlation of the antenna voltages in the domain of direction cosine coordinates is

$$\Gamma_{\mathbf{v}_i^p \mathbf{v}_j^q}(\tau) = \frac{k}{4\pi}\sqrt{G_{0,i}^p G_{0,j}^q} \iint_{\xi^2+\eta^2\leq 1} F_{n,i}^p(\xi,\eta)F_{n,j}^{q*}(\xi,\eta)$$

$$\cdot \frac{T_{ph}(\xi,\eta)\,e^{pq}(\xi,\eta)}{\sqrt{1-\xi^2-\eta^2}}\boldsymbol{\delta}_a\left(\tau - \frac{u\xi + v\eta}{f_0}\right)\sin\xi\mathrm{d}\eta\mathrm{d}\theta \tag{2.34}$$

with

$$\xi = \sin\theta\cos\phi \qquad \eta = \sin\theta\sin\phi \tag{2.35}$$

being the direction cosines and

$$u \equiv \frac{x_j - x_i}{\lambda_0} \tag{2.36}$$

$$v \equiv \frac{y_j - y_i}{\lambda_0} \tag{2.37}$$

the baseline component in the plane of the antenna, normalised to the centre wavelength.

The brightness temperature introduced in section 2.2 can be extended to its polarimetric formulation with

$$T_B^{pq}(\xi,\eta) = T_{ph}(\xi,\eta)\,e^{pq}(\xi,\eta) \tag{2.38}$$

where the superscripts pq denote the polarisation state. According to its definition T_B^h and T_B^v are real numbers representing the brightness temperature in the vertical and horizontal polarisations. T_B^{hv} and T_B^{vh} are complex cross polarisation brightness temperatures. The matrix of polarimetric brightness
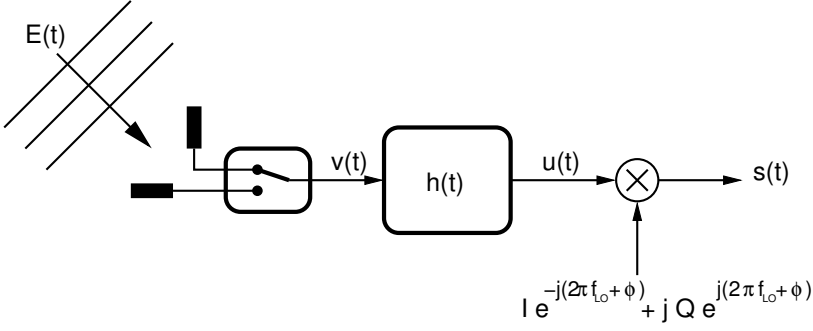
Figure 2.8: Single-channel receiver configuration.

temperature is Hermitian, as is the case with the polarimetric emissivity matrix. Finally, the cross-correlation of receiver voltages can be written as

$$
\Gamma_{\mathbf{v}_i^p \mathbf{v}_j^q} (\tau) = \frac{k}{4\pi} \sqrt{G_{0,i}^p G_{0,j}^q} \iint_{\xi^2 + \eta^2 \leq 1} F_{n,i}^p(\xi, \eta) F_{n,j}^{q*}(\xi, \eta)
$$
$$
\cdot \frac{T_B^{pq}(\xi, \eta)}{\sqrt{1 - \xi^2 - \eta^2}} \boldsymbol{\delta}_a \left(\tau - \frac{u\xi + v\eta}{f_0} \right) \sin \xi \mathrm{d}\eta \mathrm{d}\theta \qquad (2.39)
$$

Equation (2.39) relates the cross-correlation of antenna voltages with the brightness temperature of the scene T_B^{pq}. The cross-correlation between voltages at the output of two receivers will be deduced now. Figure 2.8 shows the block diagram of a receiver. It consists of a polarisation switch, which is used to elect the horizontal or the vertical probe of the antenna and connect it to the amplifier-filter. The signal is the down-converted at the mixer. The amplifier block includes the gain and filtering characteristics of the receiver.

The voltage input response $h(t)$ of the amplifier-filter block is assumed to be effectively band limited in $f_1 \leq |f| \leq f_2$. The bandwidth of the receiver i, B_i, is defined in terms of a noise equivalent bandwidth, which accomplishes $B_i < f_2 - f_1$. The transfer function of receiver i $H_i(f)$ is expressed as

$$
H(f) = \alpha_i H_{n,i}(f) \qquad (2.40)
$$

where α_i is its maximum amplitude and $H_{n,i}(f)$ is the normalised transfer function.

The local oscillator frequency f_{LO} is assumed to be identical for all receivers. A double side band conversion is assumed for the purpose of the derivation of

the visibility function, which implies that the local oscillator frequency is equal to the centre frequency: $f_{LO} = f_0$.

Being $\boldsymbol{v}(t)$ the voltage at the antenna probe, $\boldsymbol{u}(t)$ the voltage after the amplifier-filter block and $\boldsymbol{s}(t)$ the voltage after down conversion we can write

$$\boldsymbol{u}(t) = \boldsymbol{h}(t) * h(t) \tag{2.41}$$

$$\boldsymbol{s}(t) = \boldsymbol{u}(t) e^{-j2\pi f_0 t} e^{j\Phi} \tag{2.42}$$

where $h(t)$ is the voltage impulse response of the amplifier-filter circuit, and $f_0 = F_{LO}$ and Φ are the local oscillator frequency and phase. (2.42) can be expressed using its equivalent low-pass signal with respect to f_0 with

$$\boldsymbol{s}(t) = \tilde{\boldsymbol{u}}(t) e^{-j\Phi} \tag{2.43}$$

showing that the output of the of the receiver $\boldsymbol{s}(t)$ is the equivalent low-pass signal $\tilde{\boldsymbol{u}}(t)$ with respect to the local local oscillator frequency f_0, of the output of the amplifier-filter circuit, except for the the local oscillator phase term.

Cross-correlation of receiver voltages We can now compute the cross-correlation between the output voltages of receivers i and j with

$$\Gamma_{\boldsymbol{s}_i \boldsymbol{s}_j}(\tau) = \left\langle \boldsymbol{s}_i(t)\, \boldsymbol{s}_j^*(t-\tau) \right\rangle \tag{2.44}$$

and using (2.43) yields

$$\Gamma_{\boldsymbol{s}_i \boldsymbol{s}_j}(\tau) = \Gamma_{\tilde{\boldsymbol{u}}_i \tilde{\boldsymbol{u}}_j}(\tau) \tag{2.45}$$

where it has been used that the local oscillator frequency and phase is the same for both receivers. The cross-correlation between the outputs of the amplifier-filter circuit is related to that of their inputs through

$$\Gamma_{\boldsymbol{u}_i \boldsymbol{u}_j}(\tau) = \Gamma_{\boldsymbol{v}_i \boldsymbol{v}_j}(\tau) * R_{h_i h_j}(\tau) \tag{2.46}$$

The cross-correlation between the analytic signals of the voltage impulse responses $\boldsymbol{h}_i(t)$, $\boldsymbol{h}_j(t)$ can be expressed in terms of the cross-correlation of their real impulse responses $h_i(t)$, $h_i(t)$ with

$$\boldsymbol{R}_{\boldsymbol{h}_i \boldsymbol{h}_j}(\tau) = 2R_{h_i h_j}(\tau) * \boldsymbol{\delta}_a(\tau) \tag{2.47}$$

This is used, after inserting (2.39) into (2.46) to obtain the cross-correlation function between the voltages at the output of the amplifier-filter circuit

$$\Gamma_{\boldsymbol{u}_i^p \boldsymbol{u}_j^q}(\tau) = \frac{k}{8\pi} \sqrt{G_{0,i}^p G_{0,j}^q} \iint_{\xi^2 + \eta^2 \le 1} F_{n,i}^p(\xi, \eta)\, F_{n,i}^{p*}(\xi, \eta)$$

$$\cdot \frac{T_B^{pq}(\xi, \eta)}{\sqrt{1 - \xi^2 - \eta^2}} \boldsymbol{R}_{\boldsymbol{h}_i \boldsymbol{h}_j}\left(\tau - \frac{u\xi + v\eta}{f_0}\right) \mathrm{d}\xi \mathrm{d}\eta \tag{2.48}$$

which can be further developed using (2.45) and

$$\Gamma_{\tilde{\boldsymbol{u}}_i \tilde{\boldsymbol{u}}_j}(\tau) = \Gamma_{\boldsymbol{u}_i \boldsymbol{u}_j}(\tau) e^{-j2\pi f_0 \tau} \tag{2.49}$$

$$\boldsymbol{R}_{\boldsymbol{h}_i \boldsymbol{h}_j}(\tau - \tau_0) e^{-j2\pi f_0 \tau} = \boldsymbol{R}_{\tilde{\boldsymbol{h}}_i \tilde{\boldsymbol{h}}_j}(\tau - \tau_0) e^{-j2\pi f_0 \tau_0} \tag{2.50}$$

to yield the cross-correlation between receiver voltages

$$\Gamma_{\boldsymbol{s}_i^p \boldsymbol{s}_j^q}(\tau) = \frac{k}{8\pi} \sqrt{G_{0,i}^p G_{0,j}^q} \iint_{\xi^2 + \eta^2 \leq 1} F_{n,i}^p(\xi, \eta) F_{n,i}^{p*}(\xi, \eta)$$

$$\cdot \frac{T_B^{pq}(\xi, \eta)}{\sqrt{1 - \xi^2 - \eta^2}} \boldsymbol{R}_{\tilde{\boldsymbol{h}}_i \tilde{\boldsymbol{h}}_j}\left(\tau - \frac{u\xi + v\eta}{f_0}\right) e^{-j2\pi(u\xi + v\eta)} \mathrm{d}\xi \mathrm{d}\eta \tag{2.51}$$

where $\tilde{\boldsymbol{h}}_i(t)$ and $\tilde{\boldsymbol{h}}_j(t)$ are the equivalent low-pass signals with respect to f_0 of the analytic impulse response functions.

Since

$$\boldsymbol{R}_{\tilde{\boldsymbol{h}}_i \tilde{\boldsymbol{h}}_j}(\tau) = \tilde{\boldsymbol{R}}_{\boldsymbol{h}_i \boldsymbol{h}_j}(\tau) \tag{2.52}$$

with $\boldsymbol{R}_{\tilde{\boldsymbol{h}}_i \tilde{\boldsymbol{h}}_j}(\tau)$ being the equivalent low-pass signal with respect to f_0, of $\tilde{\boldsymbol{R}}_{\boldsymbol{h}_i \boldsymbol{h}_j}(\tau)$, the cross-correlation of receiver voltages becomes

$$\Gamma_{\boldsymbol{s}_i^p \boldsymbol{s}_j^q}(\tau) = \frac{k}{8\pi} \sqrt{G_{0,i}^p G_{0,j}^q} \iint_{\xi^2 + \eta^2 \leq 1} F_{n,i}^p(\xi, \eta) F_{n,i}^{p*}(\xi, \eta)$$

$$\cdot \frac{T_B^{pq}(\xi, \eta)}{\sqrt{1 - \xi^2 - \eta^2}} \tilde{\boldsymbol{R}}_{\boldsymbol{h}_i \boldsymbol{h}_j}\left(\tau - \frac{u\xi + v\eta}{f_0}\right) e^{-j2\pi(u\xi + v\eta)} \mathrm{d}\xi \mathrm{d}\eta \tag{2.53}$$

The cross-correlation function $\tilde{\boldsymbol{R}}_{\boldsymbol{h}_i \boldsymbol{h}_j}(\tau)$ can be normalised to its maximum value

$$\tilde{\boldsymbol{R}}_{\boldsymbol{h}_i \boldsymbol{h}_j}(\tau) = \int_0^\infty 4H_i(f + f_0) H_j^*(f + f_0) e^{j2\pi f \tau} \mathrm{d}f$$

$$\leq 4\sqrt{B_i B_j} \alpha_i \alpha_j \tag{2.54}$$

where B_i, B_j are the noise-equivalent bandwidth and α_i, α_j the voltage gain of each receiver. The normalised function $\tilde{\boldsymbol{r}}_{\boldsymbol{h}_i \boldsymbol{h}_j}(\tau)$ is called *fringe-washing function* and it is

$$\tilde{\boldsymbol{R}}_{\boldsymbol{h}_i \boldsymbol{h}_j}(\tau) \equiv 4\sqrt{B_i B_j} \alpha_i \alpha_j \tilde{\boldsymbol{r}}_{\boldsymbol{h}_i \boldsymbol{h}_j}(\tau) \tag{2.55}$$

Finally, assuming lossless antennæ, where the antenna gain can be expressed in terms of its solid angle Ω

$$G_0 = \frac{4\pi}{\Omega} \tag{2.56}$$

the cross-correlation of receiver voltages can be rewritten using (2.55) as

$$
\Gamma_{\boldsymbol{s}_i^p \boldsymbol{s}_j^q}(\tau) = \frac{2k\sqrt{B_i B_j}\alpha_i \alpha_j}{\sqrt{\Omega_i^p \Omega_j^q}} \iint_{\xi^2 + \eta^2 \leq 1} F_{n,i}^p(\xi, \eta)\, F_{n,i}^{p*}(\xi, \eta)
$$

$$
\cdot \frac{T_B^{pq}(\xi, \eta)}{\sqrt{1 - \xi^2 - \eta^2}} \tilde{\boldsymbol{r}}_{\boldsymbol{h}_i \boldsymbol{h}_j} \left(\tau - \frac{u\xi + v\eta}{f_0}\right) e^{-j2\pi(u\xi + v\eta)} \mathrm{d}\xi \mathrm{d}\eta \qquad (2.57)
$$

If $\tau = 0$ is taken, then we talk of the *visibility function* expressed in Kelvin

$$
V_{ij}^{pq}(u, v) \equiv \frac{1}{2} \frac{1}{k\sqrt{B_i B_j}\alpha_i \alpha_j} \Gamma_{\boldsymbol{s}_i^p \boldsymbol{s}_j^q}(0) \qquad (2.58)
$$

and we have that

$$
V_{ij}^{pq}(u, v) = \iint_{\xi^2 + \eta^2 \leq 1} T_{mod}^{pq}(\xi, \eta)\, \tilde{\boldsymbol{r}}_{\boldsymbol{h}_i \boldsymbol{h}_j} \left(-\frac{u\xi + v\eta}{f_0}\right) e^{-j2\pi(u\xi + v\eta)} \mathrm{d}\xi \mathrm{d}\eta \quad (2.59)
$$

with

$$
T_{mod}^{pq}(\xi, \eta) = \frac{F_{n,i}^p(\xi, \eta)\, F_{n,i}^{p*}(\xi, \eta)}{\sqrt{\Omega_i^p \Omega_j^q}} \frac{T_B^{pq}(\xi, \eta)}{\sqrt{1 - \xi^2 - \eta^2}} \qquad (2.60)
$$

being the modified brightness temperature, represents the correlation between the signals of two receivers, i and j, as a function of their position in the (u,v) plane. Equation (2.59) shows a Fourier Transform relationship between the visibility function $V_{ij}^{pq}(u, v)$ and the brightness temperature map T_B^{pq}, modified by the normalised antenna pattern $F_{n,i}^p(\xi, \eta)$, $F_{n,j}^{q*}(\xi, \eta)$, the fringe-washing function $\tilde{\boldsymbol{r}}_{\boldsymbol{h}_i \boldsymbol{h}_j}$ and the obliquity factor $\left(1 - \xi^2 - \eta^2\right)^{-\frac{1}{2}}$.

Equation (2.59) tells us how a broad field of view interferometer like MIRAS has to be. In first place, it is obvious that the antenna patterns $F_{n,i}^p(\xi, \eta)$, $F_{n,j}^{q*}(\xi, \eta)$, will have a broad main beam in order to have information of all desired directions (ξ, η) at the visibility function. In second place and not so obvious is the effect of the fringe-washing function $\tilde{\boldsymbol{r}}_{\boldsymbol{h}_i \boldsymbol{h}_j} \left(-\frac{u\xi + v\eta}{f_0}\right)$. All the directions (ξ, η) or antennæ positions (u,v), for which the fringe-washing function vanishes, will have a negligible influence on the visibility function. That means, that the shape of the fringe-washing function determines the direction at which the interferometer will not be *blind*. Imagine for instance an interferometer for which the transfer functions $H_i(f)$ have a very broad band. From (2.54) we know that the fringe-washing function will be narrow and thus, it will attenuate

very much the noise signals inciding on the antenna with a large angle respect to bore sight. Thus, in order to have a broad field of view interferometer, the fringe-washing function cannot be narrow.

Alternatively, if we have the same receivers, but we separate them very much from each other, a noise signal inciding onto them with a direction close to bore sight, may not be detected as the relative delay between the signals at antenna i and j is larger than the correlation time of the fringe-washing function. Thus, if a large array is desired (to increase the spatial resolution, for instance) the fringe-washing function cannot be narrow either.

It must be pointed out, that the formulation of visibility function described above is the one that has been used during this thesis. A more advanced description of the visibility function, which includes the effect of the thermal noise of each receiver coupled through the antennæ has been recently presented [22].

As a last comment, equation (2.59) gives the ideal visibilities as those measured by noiseless, error free receivers. The next chapter will present the impact in this equation of different real receiver parameters, which will result in the need for calibration. Once the receiver parameters are estimated and extracted from the measured visibility (calibration) an estimation of equation (2.59) is available

$$\hat{V}_{ij}^{pq}(u,v) = \iint_{\xi^2 + \eta^2 \leq 1} \hat{T}_{mod}^{pq}(\xi,\eta)\, \tilde{r}_{h_i h_j}\left(-\frac{u\xi + v\eta}{f_0}\right) e^{-j2\pi(u\xi + v\eta)} \mathrm{d}\xi \mathrm{d}\eta \quad (2.61)$$

and an estimation of the brightness temperature $\hat{T}_B^{pq}(\xi,\eta)$ is then obtained by inverting by any method equation (2.61).

The following chapters will be devoted to the calibration process: experimental validation and calibration performance assessment.

Chapter 3

Calibration Methods in IR

In the previous chapter we have seen the visibility function for ideal receivers. In this chapter the modelling of the receiver errors is presented. The error model used for calibrating a MIRAS baseline is [23, 24]

$$
\begin{pmatrix} \mu_{ij_{real}} \\ \mu_{ij_{imag}} \end{pmatrix} =
$$

$$
= g_i g_j \tilde{\mathbf{r}}(0) [Q] \quad \begin{pmatrix} \Re \\ \Im \end{pmatrix} \left\{ \iint_{\xi^2+\eta^2 \leq 1} \hat{T}_B^{pq}(\xi,\eta) \, \tilde{\mathbf{r}}_{n_{ij}}(\xi,\eta) \, e^{-j2\pi(u_{ij}\xi+v_{ij}\eta)} \mathrm{d}\xi \mathrm{d}\eta \right\}
$$

$$
+ \begin{pmatrix} \mu_{ij_{roff}} \\ \mu_{ij_{ioff}} \end{pmatrix} \qquad (3.1)
$$

being $\mu_{ij_{real}}$ and $\mu_{ij_{imag}}$ the real and imaginary parts of the measured normalised correlations of receiver voltages, g_i and g_j the gain parameters expressed as

$$
g_i = \sqrt{\frac{T_{Ai}}{T_{Ai} + T_{Ri}}} \qquad (3.2)
$$

$$
g_j = \sqrt{\frac{T_{Aj}}{T_{Aj} + T_{Rj}}} \qquad (3.3)
$$

with T_A and T_R the antenna and receiver temperatures of receivers i and j. The fringe-washing function at the origin is

$$
\tilde{\mathbf{r}}(0) = g_{ij} e^{j(\theta_i - \theta_j + \theta_{ij})} \qquad (3.4)
$$

where g_{ij} is the amplitude term of the fringe-washing function, θ_i, θ_j are the separable phase errors of receivers i and j and θ_{ij} is the non separable phase error. The normalised fringe-washing function is expressed as

$$\tilde{\mathbf{r}}_{n_{ij}}\left(\xi,\eta\right) = \tilde{\mathbf{r}}_{ij}\left(\xi,\eta\right)\tilde{\mathbf{r}}\left(0\right)^{-1} \tag{3.5}$$

The quadrature error matrix is

$$[Q] = \begin{bmatrix} \cos\left(\frac{\theta_{q_j}}{2} - \frac{\theta_{q_i}}{2}\right) & \sin\left(\frac{\theta_{q_j}}{2} - \frac{\theta_{q_i}}{2}\right) \\ -\sin\left(\frac{\theta_{q_j}}{2} + \frac{\theta_{q_i}}{2}\right) & \cos\left(\frac{\theta_{q_j}}{2} + \frac{\theta_{q_i}}{2}\right) \end{bmatrix} \tag{3.6}$$

The model of a baseline is presented in figure 3.1. Two receivers are shown. Four different inputs can be selected by the polswitch of each receiver. In the U-position the power of an matched load, internal to each receiver, can be selected;
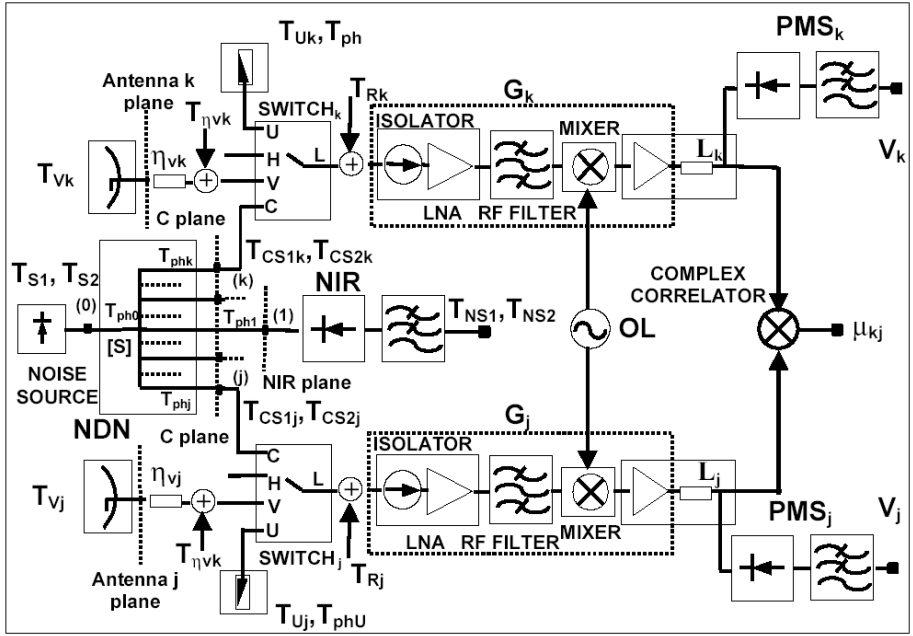
Figure 3.1: Schematic diagram of a baseline composed by two receivers and the noise distribution network used for internal calibration purposes. The definition of the magnitudes is given in section 3.1
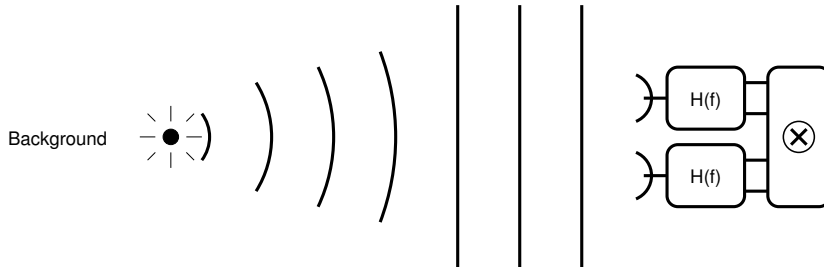
Figure 3.2: Measurement of the impulsional response of a baseline.

H and V positions select the horizontal an vertical antenna probes, respectively; while the C-port is used to inject correlated noise into both receivers forming a baseline. This noise is generated by a noise source and fed into the receivers through a Noise Distribution Network (NDN). The NDN together with the noise source is called CAlibration System (CAS). The schematic shows the main magnitudes involved in the calibration process. Of particular importance are the definition of the planes at which calibration takes place. The calibration plane will be at the C input port of the receivers (CIP), which will then be translated to the antenna input port (HIP or VIP) during antenna measurements.

The subject that must be measured in an interferometer like MIRAS is the receiver pair known as baseline. The calibration of a baseline could be done by measuring its impulsional response. Therefore a punctual source should be available at bore sight and at the far field of the antenna. This situation is described in figure 3.2. The figure shows a receiver pair that feed their output signals to a correlator unit, which computes the complex cross-correlation between the received signals. A point source is located at bore sight of the antennas and far away enough so that the incident wave has a plane wave front. Thus the punctual noise source is located in the far field of the antennas. In such a situation exact replicas of the noise signal emanating from the punctual noise source arrive in phase at the receivers. In the case of ideal and identical receivers the signals at the output of the receivers have not been distorted and continue being in phase. The correlator unit computes then the cross correlation between these signals, which coincides with the autocorrelation of the signal as both replicas are identical. Thus a correlation maximum is obtained.

In the case that the receivers are not ideal, the signals in each of the receivers will suffer different delays, the coherent demodulation will be non ideal in both

Impulsional
response

receivers and some noise will be added due to the noise factor of the receivers. All these factors and others that have not been described yet will make that the resulting cross-correlation of the signals differs from the ideal one.

This calibration approach has some disadvantages. The first one is the availability of a point source which is close to an ideal one. A radiating antenna could be used as point source. But this possibility is not practical in radiometric systems as any radiation in the protected radiometry bands is forbidden. Thus only natural targets as sun, moon or radiating galaxies could be used. These have the drawback that they are neither isolated nor controlled. Other radiation sources close to the desired one would difficult the calibration, as the overall radiation captured by the receivers would include all radiation available in the field of view of the antennas. This is described in figure 3.2 as *Background*.

Another factor which makes unfeasible this calibration approach in the SMOS mission is the fact that the receiver antennas have a broad field of view. In the situation of figure 3.2 the baseline would be calibrated for the bore sight direction. Differences in the antenna patterns should be calibrated for each direction, implying thus a measurement for each direction.. This is known as the G-matrix method. It is obvious that making a calibration for each direction is a time consuming procedure and it is thus not feasible for a 2-D space borne interferometer like MIRAS. Moreover, the G-matrix should be recalculated periodically in order to track and correct system drifts due to temperature, aging, etc.

Noise injection calibration

Other calibration methods have been proposed which separate the effect of the antenna patterns from the receiver errors. The principle of these methods are shown in figure 3.3. The plane wave front which enters the receivers has now been generated with a microwave noise source connected to a balanced power dividing network, with equal phase in each of the output branches. These signal replicas are fed into the receivers after the antennas, using an additional input connector. A microwave switch is used to select this calibration port C or the antenna ports V (vertical) and H (horizontal) polarisation. This microwave switch is called *polswitch*. In this way the baseline errors (quadrature errors, in-phase errors and receiver noise temperature), may be calibrated independently of the antenna. The antenna patterns must be measured separately in an anechoic chamber in order to correct for them.

The next sections go into deeper detail on noise injection methods proposed for calibrating MIRAS.
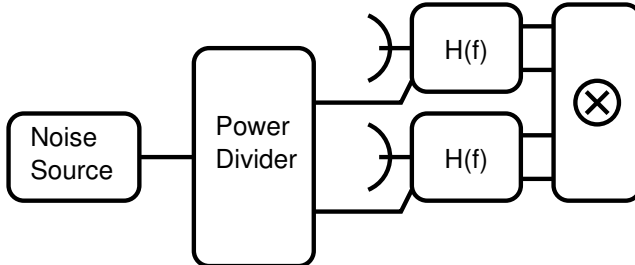
Figure 3.3: Noise injection principle for baseline calibration.

3.1   Single Power Noise Injection

The baseline calibration methods proposed in [25, 26] are the ones that have been tested during the first part of this thesis. The basic principle of these calibration methods conisists in injecting correlated and uncorrelated noise into the receivers. The measured correlations are used to obtain the correlation offset, receiver quadrature errors, in-phase baseline error and amplitude errors. Additionally, a method for correcting the correlation offset introduced by non-ideal A/D converters [27, 28] has also been tested. These methods are reviewed in this section.

Figure 3.4 shows the block diagram for a single baseline. It consists of a pair of LICEF receivers. These are total power radiometers with digitised in-phase and quadrature outputs. The polswitch at the input of the receivers allows to select one of four possible input signals. Horizontal (H) and vertical (V) polarisation antenna probes are selected when measuring a scene. The (C) port is used for correlated noise injection measurements, where the same replica of noise is injected into both receivers of a baseline. The (U) port is used to have uncorrelated noise at the input of both receivers. In this case the polswitch selects the noise signal generated by a matched load at the input of the receivers. As the thermal noise is generated by different loads, the noise signals at the input of the receivers are uncorrelated.

Let's call the signal at the input of the receivers $s_m(t)$, where the subindex m is related to each receiver. The noise signals are filtered by the frontend filter and amplified by the receiver before reaching the mixer. This is represented in the figure by $H_m(f)$, which takes into account the end-to-end receiver frequency response. It is assumed that all the receiver noise is added to the signal at this

Baseline description
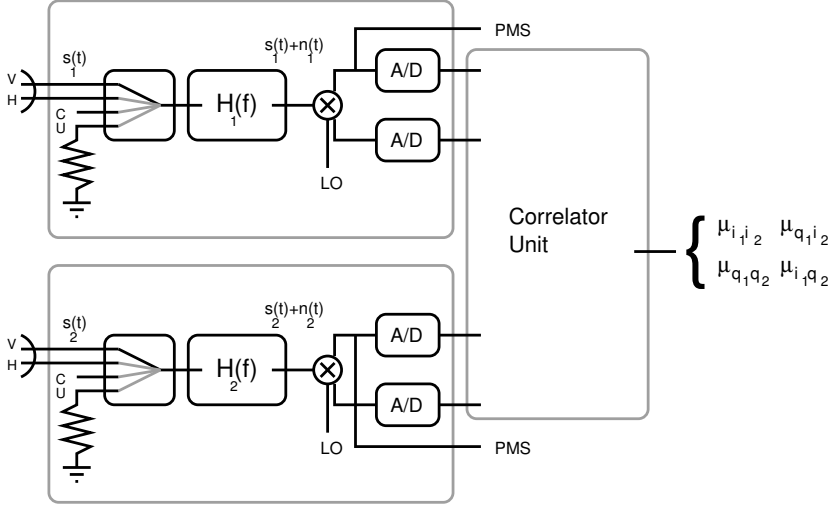
Figure 3.4: Simplified block diagram of a single baseline.

RF stage. The receiver noise of receiver m is called $n_m(t)$.

The downconversion takes place at the mixer, where the bandpass signal $s_m(t) + n_m(t)$ is separated into its in-phase and quadrature components. A diode detector gives the PMS voltage of the receivers, which is proportional to the equivalent noise power at the input of the receiver. In-phase and quadrature components of the bandpass signals are then sampled at a rate of $55.84MHz$ and quantised with a single bit. If the signal is positive it is coded with a one, if it is negative with a zero. Finally, the DIgital COrrelator System (DICOS) computes the cross-correlations of the baseline.

A/D offset   As shown in [28], if the A/D conversor presents an offset, this translates into correlation errors. A method to measure and correct this offset was proposed in [27]. Experimental results have been first presented during this thesis [29, 30]

As the A/D conversor offset is present in the correlations independently of what signal (H-pol, V-pol or calibration) was demodulated by the receiver it must be always removed at first from all the measured correlations. The method is explained in section 3.4.

Residual offset   Once the A/D conversor offset has been removed a residual offset may be present in the correlations. The origin of this residual offset may be found in the

cross-coupling between receivers. The signal from one receiver may couple to the neighbouring receiver. When both output signals of the receivers are cross-correlated a residual correlation value will be present. The way of measuring this residual offset is to inject uncorrelated noise into the baseline receivers. This is achieved by selecting the U port of the LICEF receivers, which is connected to a matched load inside each receiver (figure 3.1). This thermal noise shows zero cross-correlation, because it has been generated at different loads. Thus, any correlation value will be due to the cross-coupling effect. Note that during this U-calibration, the antennas are not connected to the receivers, thus, any possible cross-couping through the antennas, during the measurement of a scene will not be calibrated.

Up to this point offset errors have been taken into account. The next step is to calibrate the phase errors. The downconversion can have two possible errors, *quadrature* and *in-phase* error. The quadrature error of each receiver is the angular difference between the demodulated in-phase and quadrature components, respect to the ideal 90°. The quadrature error of each receiver can be estimated with

Quadrature error

$$\mu_{i_m q_m} = -\sin\theta_{q_m} \tag{3.7}$$

where $\mu_{q_m i_m}$ is the cross correlation between the in-phase and quadrature components of receiver m and θ_{q_m} is the quadrature error of receiver m. [26]

The in-phase error is the phase difference between the two demodulated in-phase signals of one baseline. Equation (3.8) and (3.9) show the relationship between the correlation at the input of the receiver (or ideal correlation for ideal receivers) and the correlations at the output of the receivers [25, 26]

In-phase error

$$\begin{pmatrix} \mu_{ii} \\ \mu_{qi} \end{pmatrix} = \tilde{g}_{mn} \begin{bmatrix} \cos(\alpha_{mn} + Q_{mn}) & \sin(\alpha_{mn} + Q_{mn}) \\ -\sin(\alpha_{mn} + Q'_{mn}) & \cos(\alpha_{mn} + Q'_{mn}) \end{bmatrix} \begin{pmatrix} V_{Re} \\ V_{Im} \end{pmatrix} \tag{3.8}$$

$$\begin{pmatrix} \mu_{qq} \\ \mu_{iq} \end{pmatrix} = \tilde{g}_{mn} \begin{bmatrix} \cos(\alpha_{mn} - Q_{mn}) & \sin(\alpha_{mn} - Q_{mn}) \\ \sin(\alpha_{mn} - Q'_{mn}) & -\cos(\alpha_{mn} - Q'_{mn}) \end{bmatrix} \begin{pmatrix} V_{Re} \\ V_{Im} \end{pmatrix} \tag{3.9}$$

where the baseline gain factor $\tilde{g}_{mn}$ has been included.[1] Equation (3.8) corresponds to the solution when using the μ_{ii} and μ_{qi} correlations; equation (3.9) to the redundant case with μ_{qq} and μ_{iq}.[2]

---

[1]The gain factor is explained later in this section.

[2]Sub-indices m and n have been dropped from the measured normalised correlations $\mu_{i_m i_n}$, $\mu_{q_m i_n}$, $\mu_{q_m q_n}$ and $\mu_{i_m q_n}$ for simplicity in the notation. The first signal corresponds always to receiver m, while the second signal corresponds to receiver n, yielding the notation μ_{ii}, μ_{qi}, μ_{qq} and μ_{iq} for the measured normalised correlations.

The normalised correlations on the right side of the equation, V_{Re} and V_{Im} represent the real and imaginary part of the measured normalised correlations if the receiver would be noiseless and with no phase errors, that is, at the input of the receiver. The angular terms are

$$\alpha_{mn} = \theta_n - \theta_m - \theta_{mn} \tag{3.10}$$

$$Q_{mn} = \frac{1}{2}(\theta_{qn} - \theta_{qm}) \tag{3.11}$$

$$Q'_{mn} = \frac{1}{2}(\theta_{qn} + \theta_{qm}) \tag{3.12}$$

with θ_m, θ_n and θ_{qm}, θ_{qn} being the phase and quadrature errors of the receivers and θ_{mn} the phase difference introduced by the Fringe-Washing Function (FWF) of the baseline.

From any of equations (3.8) or (3.9) the in-phase error of the baseline α_{mn} can be estimated. Therefor it is necessary to know the correlation at the input of the receiver. With a correlated noise injection measurement, where the pol-switch of the receivers in connected the the C input port, this is possible. In the ideal case were perfectly correlated noise is injected into the baseline $V_{Re} = 1$ and $V_{Im} = 0$ and equations (3.8) and (3.9) can be inverted. In [25] it is proposed to use theses equations for many baselines at once and then invert them numerically in order to obtain the in-phase errors α_{mn} for many baselines at the same time. This approach has the advantage of having an over determined system.

In [26] the value of α_{mn} is obtained from one single baseline analytically, for the ideal case where $V_{Re} = 1$ and $V_{Im} = 0$. In this situation equations (3.8) and (3.9) simplify very much due to the V_{Im} being zero. The value for the in-phase error is given by

$$\tan \alpha_{mn} = \frac{\mu_{qi} \cos Q_{mn} + \mu_{ii} \sin Q'_{12}}{\mu_{qi} \sin Q_{mn} - \mu_{ii} \cos Q'_{12}} \tag{3.13}$$

$$\tan \alpha_{mn} = \frac{\mu_{iq} \cos Q_{mn} + \mu_{qq} \sin Q'_{12}}{\mu_{qi} \cos Q'_{mn} - \mu_{ii} \sin Q_{12}} \tag{3.14}$$

where equation (3.13) is nominal correlations and equation (3.14) for the redundant ones. This method has been used during the Image Validation Tests described in the experimental part of this thesis.

In appendix A equations (3.8) have been solved analytically for α_{mn} without any restriction for the value of the input correlation V_{Re}, V_{Im}, allowing thus to calibrate the in-phase and quadrature errors with any arbitrary input correlation. The only obvious exception is for the case when $V_{Re} = V_{Im} = 0$, that is, when no correlated noise is present at the input of the receivers.

Continuing with the baseline calibration, the remaining parameter to be obtained from equations (3.8) or (3.9) is the gain factor   **Gain factors**

$$\tilde{g}_{mn} = g_m^c g_n^c g_{mn} \tag{3.15}$$

with

$$g_m^c = \sqrt{\frac{T_C}{T_C + T_{R_m}}} \tag{3.16}$$

$$g_n^c = \sqrt{\frac{T_C}{T_C + T_{R_n}}} \tag{3.17}$$

being T_C the correlated noise temperature and T_{R_m}, T_{R_n} the receiver noise temperatures. g_{mn} is the non-separable error term due to the FWF.

When an antenna measurement is being done, the gain factor is

$$\tilde{g}_{mn} = g_m g_n g_{mn} \tag{3.18}$$

with

$$g_m = \sqrt{\frac{T_A}{T_A + T_{R_m}}} \tag{3.19}$$

$$g_n = \sqrt{\frac{T_A}{T_A + T_{R_n}}} \tag{3.20}$$

being T_A the antenna temperature and T_{R_m}, T_{R_n} the receiver noise temperatures. The antenna temperature T_A has been assumed to be equal for both receivers. Note that the gain factor during noise injection calibration is not directly required. What is needed indeed is the gain factor during antenna measurement in order to be able to invert equations (3.8) or (3.9) during antenna measurements.

If two consecutive measurements of the PMS are done, one for the noise injection measurement N_{C_m} and another for the antenna measurement N_{A_m},

we can take the quotient of both yielding

$$Y_m = \frac{N_{C_m}}{N_{A_m}} = \frac{k_B \left(T_C + T_{R_m}\right) B_m G_m}{k_B \left(T_A + T_{R_m}\right) B_m G_m} = \frac{T_C + T_{R_m}}{T_A + T_{R_m}} = \frac{T_C}{T_A} \left(\frac{g_m}{g_m^c}\right)^2 \quad (3.21)$$

The gain factor during antenna measurement can thus be estimated with

$$g_m g_n g_{mn} = g_m^c g_n^c g_{mn} \frac{T_A}{T_C} \sqrt{Y_m Y_n} \quad (3.22)$$

showing that only the Y ratio has to be measured in order to obtain the gain factor during antenna measurement. The values for T_C and T_A are measured with a dedicated Noise Injection Radiometer (NIR). A consequence of this is that the antenna temperature T_A is assumed to be the same for all receivers, including the NIR. The product $g_m^c g_n^c g_{mn}$ can easily obtained from (3.8) during noise injection when $V_{Re} = 1$ and $V_{Im} = 0$ obtaining

$$\tilde{g}_{mn} = \frac{\mu_{ii}}{\cos\left(\alpha_{mn} + Q_{mn}\right)} = -\frac{\mu_{qi}}{\sin\left(\alpha_{mn} + Q'_{mn}\right)} \quad (3.23)$$

When the redundant correlations are used the gain factor can be obtained with

$$\tilde{g}_{mn} = \frac{\mu_{qq}}{\cos\left(\alpha_{mn} - Q_{mn}\right)} = -\frac{\mu_{iq}}{\sin\left(\alpha_{mn} - Q'_{mn}\right)} \quad (3.24)$$

In appendix A an expression is deduced for obtaining $\tilde{g}_{mn}$ for any arbitrary input correlation V_{Re}, V_{Im}.

NDN effect on gain parameters The previous equations assume that the correlation at the input of the receivers is ideal, that is, $V_{Re} = 1$, $V_{Im} = 0$. This would be the case for a lossless NDN with equal phase shift at each output branch. If this is taken into account, the relationship between the gain factors during calibration and during antenna measurement of equation (3.22) is rewritten as [26]

$$g_m g_n g_{mn} = g_m^c g_n^c g_{mn} \frac{T_A}{(T_{ref} - T)) |S_{0m}| |S_{0n}|} \sqrt{Y_m Y_n} \quad (3.25)$$

being S_{0m} and S_{0n} the S-parameters from the input port of the NDN to the m and n output ports, T_{ref} the injected temperature into the NDN and T the physical temperature of the NDN and the receivers. It is assumed that S_{0m} and S_{0n} have the same phase.

3.2   NDN Effect on Calibration

In the previous section 3.1 the calibration parameters for the single power noise injection method were obtained. This was done assuming that the correlation at the input was the ideal correlation value $V_{Re} = 1$, $V_{Im} = 0$. The effect of the NDN on the amplitude of the correlations was taken into equation (3.25). The effect of the phase of the phase at the correlations was not taken into account, as it was still assumed that the imaginary part of the input correlations, $V_{Im} = 0$. Another calibration approach would be to assume that the input correlations were different from its ideal value. In such an approach the calibration equations would also be (3.8) and (3.9), but now V_{Re} and V_{Im} might take any value. It is possible to solve these two equations for the in-phase error α_{mn} and the gain factor $\tilde{g}_{mn}$ from the measured correlations μ_{ii}, μ_{qi}, μ_{qq}, μ_{iq} and the correlations at the input V_{Re}, V_{Im}.

The in-phase error can be obtained with

$$\tan \alpha_{mn} = \frac{\mathbf{v}^T \mathbf{A} \mu_{iiqi}}{\mathbf{v}^T \mathbf{B} \mu_{iiqi}} \tag{3.26}$$

where A and B are two by two matrices with angular terms, $v = (V_{Re}, V_{Im})^\top$ and $\mu_{iiqi} = (\mu_{ii}, \mu_{qi})^\top$. while the gain factor is obtained with

$$\tilde{g}_{mn}^2 = \frac{\mu_{ii} + \mu_{qi} + 2\mu_{ii}\mu_{qi} \sin(Q'_{mn} - Q_{mn})}{(V_{Re}^2 + V_{Im}^2) \cos^2(Q'_{mn} - Q_{mn})} \tag{3.27}$$

Please refer to appendix A for further details.

This approach assumes that the correlation at the input of the receivers is
known. In order to know these exact correlation values Bosma's noise theory [31] may be used, which states that the correlation and power of the noise waves emerging from a passive network can be predicted, provided its s-parameters are known and the power and correlation of the noise waves entering the network are also known. In appendix B it is shown how the correlation of the noise signals emerging from the NDN can be computed. These correlation values could then be used in equations (A.13) or (A.18) to obtain the in-phase error of the baseline and in (A.29) to obtain its gain factor.

3.3   Two Level Noise Injection

Experimental results have presented in this thesis [29, 32, 33] and in [34] show that the single noise injection calibration approach gives good results to estimate

the calibration phase terms. However, this is not the case relating the amplitude calibration. The two main problems are:

- The offset given by the diode detector is not calibrated.

- It is required to estimate the absolute correlated noise injected via the NDN, including the contribution of the the NDN losses.

The calibration method proposed in [35, 36] uses the block diagram of figure 3.1. The figure shows two receivers, which can select their input signals through the polswitch. Correlated noise is generated by the noise source and it is distributed to the receivers through the NDN. This noise source can generate two different noise temperature levels T_{S1} and T_{S2}. The LICEFs output the in-phase and quadrature signals, which are cross correlated at the complex correlator. The PMS output voltage of the LICEFs is also available. An attenuator L at the PMS path of the receiver can be switched between two different values. Quadrature and in-phase errors are calibrated the same way as in single power level noise injection.

In [36] it is found that the so-called calibrated visibility can be written as

$$\hat{V}_{ij} = \frac{\sqrt{T_{sys_i}T_{sys_j}}}{G_{ij}} M_{ij} \qquad (3.28)$$

where, $T_{sys_i} = T_{a_i} + T_{r_i}$ is the system temperature, T_{A_i} the antenna temperature and T_{r_i} the receiver noise temperature referred to the antenna phase centre, G_{ij} is the fringe-washing function at the origin and M_{ij} is the *quadrature-corrected normalised correlation*. The baseline is amplitude calibrated once the instrumental amplitude error term H_{ij} is known:

$$H_{ij} = \frac{1}{|G_{ij}|} \sqrt{T_{sys_i}T_{sys_j}} \qquad (3.29)$$

The four-points calibration technique, as proposed in [37, 35], is used to calibrate the PMS and it is based on a linear model of the diode response. The measured voltage out of the PMS when an equivalent system temperature T_{sys} is present at system input (port C of the switch receiver i, figure 3.1), is given by

$$V_i = V_{off_i} + G_i T_{sys_i} \qquad (3.30)$$

where now $T_{sys_i} = T_{ext_i} + T_{r_i}$, with T_{ext_i} being the noise temperature injected into port C of the switch through the NDN. V_{off} is a voltage offset of the

PMS circuit, G is the gain in V/K. Remember that within the single power calibration this voltage offset was not taken into account. The PMS of receiver i is calibrated once the unknown parameters V_{off_i} and G_i are estimated. Note that in such cases where only differential knowledge of T_{ext_i} is required, the term T_{r_i} is irrelevant.

The PMS is fully calibrated once the parameters V_{off_i}, G_i and T_{R_i} have been obtained. In order to estimate these parameters two different noise powers levels are injected into the receiver T_{C1_i} and T_{C2_i} with $T_{C1_i} < T_{C2_i}$. T_{C1_i} is known as *warm noise*, while T_{C2_i} as *hot noise*. Additionally the overall system gain can be switched between two values G_i and G_i/L_i, by adding an attenuator in the IF part of the receiver [37]. It can be assumed to be noiseless because it is at the IF stage. In total four measurements are done combining the two input temperatures with the two attenuation values

$$
\begin{aligned}
V_{1_i} &= V_{off_i} + G_i(T_{C1_i} + T_{R_i}) & \text{warm, no attenuation} & \quad (3.31) \\
V_{2_i} &= V_{off_i} + G_i(T_{C2_i} + T_{R_i}) & \text{hot, no attenuation} & \quad (3.32) \\
V_{3_i} &= V_{off_i} + \frac{G_i}{L_i}(T_{C1_i} + T_{R_i}) & \text{warm, with attenuation} & \quad (3.33) \\
V_{4_i} &= V_{off_i} + \frac{G_i}{L_i}(T_{C2_i} + T_{R_i}) & \text{hot, with attenuation} & \quad (3.34)
\end{aligned}
$$

Note that, by this method, the PMS will be calibrated at the plane where the calibration temperatures T_{C1_i} and T_{C2_j} are known. In this case this is the C plane. Therefore, in measurement mode, a plane translation must be performed from the calibration plane C to the antenna plane. When the polswitch is in antenna position (for instance in H), the PMS voltage is V_{H_i} and the estimated system temperature at the C plane is obtained through

$$
T^C_{sysH_i} = \frac{V_{H_i} - V_{off_i}}{V_{2_i} - V_{1_i}}\left(T_{C2_i} - T_{C1_i}\right) \tag{3.35}
$$

where the offset voltage can be obtained from the PMS measurements with

$$
V_{off_i} = \frac{V_{2_i}V_{3_i} - V_{1_i}V_{4_i}}{(V_{2_i} - V_{4_i}) - (V_{1_i} - V_{3_i})} \tag{3.36}
$$

In order to generate the warm temperature T_{C1_i} it is possible to use the U source (matched load). The hot temperature T_{C2_i} is obtained using the noise source of the CAS. In this case the equivalent system temperature at the plane C when the switch is in H position can be written as

$$
T^C_{sysH_i} = \frac{V_{H_i} - V_{off_i}}{V_{2_i} - V_{1_i}}\left(T_S|S_{i0}|^2 - T_U + \Delta T_{[s],T_{ph}}\right) \tag{3.37}
$$

where T_U is the physical temperature of the matched load at the U port, T_S is the temperature of the hot noise source connected to port "0" of the NDN and S_{k0} is the s-parameter from the noise source and the "k" port of the NDN. The term $\Delta T_{[s],T_{ph}}$ stands for the noise contribution of the NDN itself. It depends on its physical temperature and the uncertainty in the measurement of its S-parameters. As it is readily seen, this approach has significant sources of error since uncertainty in the measure of the different terms are uncorrelated and add in a quadratic sense. The relative calibration overrides these problems.

Relative amplitude calibration

As shown in figure 3.1, both the hot and the warm temperatures are synthesised by a common external noise source. That is, two equivalent noise temperatures T_{S_1} (warm) and T_{S_2} (hot) are delivered to port "0" of the NDN (fig. 3.1). Theses temperatures are measured by the NIR, giving the equivalent external temperatures at NIR plane T_{NS1} and T_{NS2} (port "1" of the NDN). The equivalent external temperatures at the calibration plane of the receiver units (ports "i" and "j" of the NDN) are T_{C2_i}, T_{C2_j}, T_{C1_i} and T_{C1_j}. However, it must be taken into account that the NDN is a lossy network which introduces additional temperature terms related to its physical temperature. In a general sense, the equivalent system temperatures at ports "1" and "i" of the NDN when the hot temperature is injected are given by:

$$T_{sys_i}^{C2} = T_{S2}|S_{i0}|^2 + T_{r_i} + \Delta T_{[s],T_{ph}} \tag{3.38}$$

$$T_{sys_i}^{N2} = T_{S2}|S_{10}|^2 + T_{r_{NIR}} + \Delta T'_{[s],T_{ph}} \tag{3.39}$$

where the ΔT and $\Delta T'$ terms are the contribution of the NDN due to its physical temperature [38] and T_{ri} and $T_{r_{NIR}}$ are the equivalent receiver temperatures at the calibration planes. Taking into account a similar expression for T_{S1}, now $T_{sysH_k}^{C}$ can be written as

$$T_{sysH_i}^{C} = \frac{V_{H_i} - V_{off_i}}{V_{2_i} - V_{1-i}} |S_{i0}|^2 \left(T_{S2} - T_{S1}\right) \tag{3.40}$$

and, as a function of NIR measured temperatures

$$T_{sysH_i}^{C} = \frac{V_{H_i} - V_{off_i}}{V_{2i} - V_{2i}} \frac{|S_{i0}|^2}{|S_{10}|^2} \left(T_{sys_i}^{N2} - T_{sys_i}^{N1}\right) \tag{3.41}$$

where the dependence with the physical temperature of the NDN has been removed due to the different approach. Finally, in order to get the system temperature at antenna H phase centre, in horizontal mode, a plane translation

is performed.

$$T^H_{sysH_i} = \frac{V_{H_i} - V_{off_i}}{V_{2i} - V_{2i}} \frac{|S_{i0}|^2}{|S_{10}|^2} \frac{|S_{LC_i}|^2}{|S_{LH_i}|^2 \eta_{H_i}} \left(T^{N2}_{sys} - T^{N1}_{sys}\right) \tag{3.42}$$

where S_{LC_i} and S_{LH_i} are the switch S-parameters of receiver i for the C and H paths, respectively, and η_{H_i} is the antenna ohmic efficiency in horizontal mode. The same procedure can be applied to receiver j so as to retrieve the system temperatures T_{sys_i} and T_{sys_j} which are required to obtain the calibrated visibility (eq. 3.28).

Now, the fringe-washing term G_{ij} in equation (3.28) can also be obtained by the two-level noise injection procedure (see figure 3.1). The correlated temperature $T_{C1_{ij}}$ (referred to ports C of receivers i and j) when the noise source is in warm mode is given by (eq. (22a) in [38]):

$$T_{C1_{ij}} = S_{i0} S^*_{j0} T_{S1} + \sum_{n=1}^{N} S_{in} S^*_{jn} T_{rn} - T_{ph} \sum_{n=0}^{N} S_{in} S^*_{jn} \tag{3.43}$$

In this case, since the contribution of the NDN to $T_{C1_{ij}}$ must be removed, its physical temperature has to be monitorired and the absolute value of its S-parameters must be known. However, a robust estimation of G_{ij} can be obtained by making two measurements at two different correlated temperatures (hot and warm). In this case, equation (3.28) yields the complex correlation temperatures

$$T_{C1_{ij}} = \frac{1}{G_{ij}} \sqrt{T^{C1}_{sys_i} T^{C1}_{sys_j}} M^{C1}_{ij} \tag{3.44}$$

$$T_{C2_{ij}} = \frac{1}{G_{ij}} \sqrt{T^{C2}_{sys_i} T^{C2}_{sys_j}} M^{C2}_{ij} \tag{3.45}$$

Subtracting one equation from the other, arranging terms and taking into account that the equivalent temperatures of the noise source are measured by the NIR as

$$T^{N2}_{sys} - T^{N1}_{sys} = |S_{10}|^2 \left(T_{S2} - T_{S1}\right) \tag{3.46}$$

and equation (3.43)

$$T_{C2_{ij}} - T_{C1_{ij}} = S_{i0} S^*_{j0} \left(T_{S2} - T_{S1}\right) = \frac{S_{i0} S^*_{j0}}{|S_{10}|^2} \left(T^{N2}_{sys} - T^{N1}_{sys}\right) \tag{3.47}$$

the fringe-washing term at switch C input plane is obtained as

$$G_{ij}^C = \frac{|S_{10}|^2}{S_{i0}S_{j0}^*} \frac{M_{ij}^{C2}\sqrt{T_{sys_i}^{C2} T_{sys_j}^{C2}} - M_{ij}^{C1}\sqrt{T_{sys_i}^{C1} T_{sys_j}^{C1}}}{T_{sys}^{N2} - T_{sys}^{N1}} \tag{3.48}$$

where the dependence on the physical temperature T_{ph} has been removed. More-over, taking into account (3.40)

$$T_{sys_i}^{C2} = \frac{V_{2_i} - V_{off_i}}{V_{2_i} - V_{1_i}} \frac{|S_{i0}|^2}{|S_{10}|^2} \left(T_{sys}^{N2} - T_{sys}^{N1}\right) \tag{3.49}$$

$$T_{sys_i}^{C1} = \frac{V_{1_i} - V_{off_i}}{V_{2_i} - V_{1_i}} \frac{|S_{i0}|^2}{|S_{10}|^2} \left(T_{sys}^{N2} - T_{sys}^{N1}\right) \tag{3.50}$$

the fringe-washing amplitude term can be written as a function of the measured PMS voltages

$$G_{ij}^C = \frac{M_{ij}^{C2}\sqrt{\left(V_{2_i} - V_{off_i}\right)\left(V_{2_j} - V_{off_j}\right)} - M_{ij}^{C1}\sqrt{\left(V_{1_i} - V_{off_i}\right)\left(V_{1_j} - V_{off_j}\right)}}{\sqrt{\left(V_{2_i} - V_{1_i}\right)\left(V_{2_j} - V_{1_j}\right)}} \frac{|S_{i0}||S_{j0}|}{S_{i0}S_{j0}^*}$$

$$\tag{3.51}$$

giving a very robust estimated of G_{ij}, as it does only depend on PMS linearity and measured *quadrature corrected correlations*. Note that the fringe-washing function is measured at plane C, since the LICEFs are calibrated at this plane.

3.4 A/D Offset Correction Method

The visibilities are obtained by cross-correlating complex signals. Complex cor-relations can also be performed as a combination of two real-signal correla-tions [19]. If the *nominal* correlations are used (IIQI)

$$V_{mn} = 2\Gamma_{i_m i_n} + j2\Gamma_{q_m i_n} \tag{3.52}$$

and if the *redundant* (QQIQ) correlations are used

$$V_{mn} = 2\Gamma_{q_m q_n} + j2\Gamma_{i_m q_n} \tag{3.53}$$

Figure 3.5 shows how a cross-correlation of two real signals is performed in MIRAS including additional correlations for A/D offset correction with 1&0s. In figure 3.5 the real signals are sampled fulfilling the Nyquist rate and are then

coded with one bit. If the sample of the signal is positive it is coded with 1 otherwise with 0. As the comparator in the is not ideal a small offset a in the comparator will exist. Thus we will have as coding rule

$$X = \begin{cases} 1 & \text{if } x > a \\ 0 & \text{otherwise} \end{cases} \qquad (3.54)$$

The same is valid for the comparator in the other branch where we have a comparator offset b.

$$Y = \begin{cases} 1 & \text{if } y > b \\ 0 & \text{otherwise} \end{cases} \qquad (3.55)$$

These sequences of ones and zeros are then correlated by counting coincidences of bits in the two branches. In [27] it is shown that the obtained correlations are related to the correlation of the real signals $\mu = R_{xy}(0)$ by

$$E\{XY\} = \frac{1}{2} + \frac{1}{\pi}\arcsin\mu - \frac{1}{\sqrt{1-\mu^2}}(\mu X_{01}^2 + \mu Y_{01}^2 - 2X_{01}Y_{01}) \qquad (3.56)$$
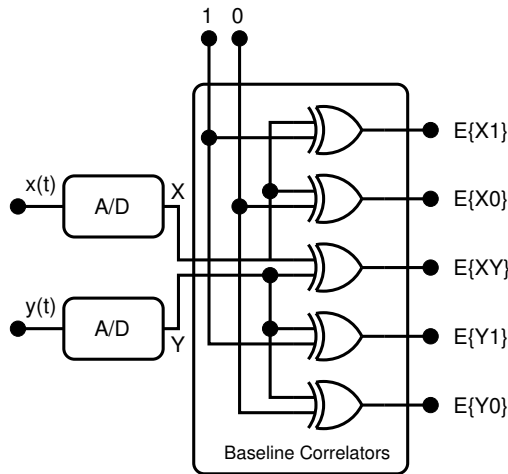
Figure 3.5: Real Signal Correlation with 1&0 correlations for A/D calibration.

where $E\{XY\}$ is the correlation between the digital sequences X and Y obtained with the digital correlator

$$E\{XY\} = \frac{\text{Number of coincidences}}{\text{Number of observed samples}} \tag{3.57}$$

and

$$X_{01} = \frac{E\{X0\} - E\{X1\}}{2} \tag{3.58}$$

$$Y_{01} = \frac{E\{Y0\} - E\{Y1\}}{2} \tag{3.59}$$

$E\{X0\}$ and $E\{Y0\}$ are the number of zeros in the X and Y sequences and $E\{X1\}$ and $E\{Y1\}$ the number of ones, all normalised by the total number of observed samples. It has to be noted that the total number of observed samples equals the sum of ones and zeros. Equation (3.56) is transcendental and thus μ cannot be isolated, but its value can be obtained by numerical methods.

In the ideal case where the offset is negligible $(a, b \rightarrow 0)$, equation (3.56) reduces to the ideal case as presented in [39].

$$E\{XY\} = \frac{1}{2} + \frac{1}{\pi} \arcsin \mu \tag{3.60}$$

Chapter 4

Experimental Validation of Calibration Methods

4.1   Sun Image Validation Tests

A series of *Image Validation Tests* for MIRAS have been done, in order to vali-
date different calibration, technological and image generation aspects. A small
prototype of MIRAS radiometer has been used with only two LICEF-1 receivers.
Instead of measuring all the baselines at once with many receivers, they have
been measured with one single pair of receivers that have been moved to all the
positions of the array consecutively. The scene that has been observed was a
delta type image, with only a bright (hot) spot on a dark (cold) background in
order to be able to measure the impulsional response of the system. A natural
scene consisting of the bright Sun and the cold sky was used. The Sun served
as the delta of the image, as the angular resolution of the prototype instrument
was far worse than the angular size of the Sun. In other tests the Moon was
used as the punctual source in order to measure a less brighter source than the
Sun. Table 4.1 shows a summary of the tests that have been done. All these
tests were done at ASTRON/NFRA[1] premises in Dwingeloo, the Netherlands
and carried out during my stage at ESTEC, ESA.

Here only the results for the Sun test of IV-3B are presented; a complete
report on all the Image Validation campaigns is given in [29]. This Sun imaging
test was named *Test 02*. It gave the best results as several technical problems

Image Validation test

---

[1]ASTRON/NFRA: Netherlands Foundation for Research in Astronomy

Table 4.1: Image validation test campaign summary

Name	Date	Measurement	Successful
IV-1	3/09 - 6/09 2001	Sun Image	Yes
IV-3	24/2 - 1/03 2002	Moon Image	No
IV-3B	23/3 - 26/3 2002	Sun Image	Yes
		Sun Fringes	Yes
		Moon Image	No
		Moon Fringes	No

of the initial campaigns were solved or reduced. Some of the most important problems were interference from the digital lines to the radiometer antennas, receiver failure due to cold ambient temperature or simply strong rain and wind.

4.1.1   Experiment Setup

Experiment Setup

Figure 4.1 shows the experiment concept. A Y-shaped structure, with 9 elements per arm and a spacing of 20cm (0.94λ) between elements, placed on a tripod has been used to support the two LICEF-1 receivers. The receivers were moved from one position to the next along the arms of the array in order to measure all the baselines. In this way the measurement of a complete scene took between 2 and 3 hours depending on the number of measured baselines and the chosen correlation time. During this interval the Sun changed its position in the sky and thus no correct image of the Sun could be obtained if this was not taken

Sun Tracking

into account. To correct for the Sun movement, a rotation of the array around its vertical axis in steps of $1.5°$ has been performed. In this way the Sun was kept inside the synthetic lobe of the antenna for all baseline measurements. It has to be noted that the experiments were done close to noon, when the Sun's elevation is almost constant and therefore only a correction in azimuth was necessary. Ground planes from position one (the closest to the centre of the array) up to position eight were available in order to reduce back lobe radiation.

In the presented test, a MIRAS of eight elements per arm was implemented, resulting in 213 baseline measurements. The arm A of the array was pointing in the opposite direction to the Sun. In this way the imaged Sun would appear in the centre of an alias zone and not at the edge of it. This was chosen so, to prevent from possible unknown effects in the transition part between alias zones.
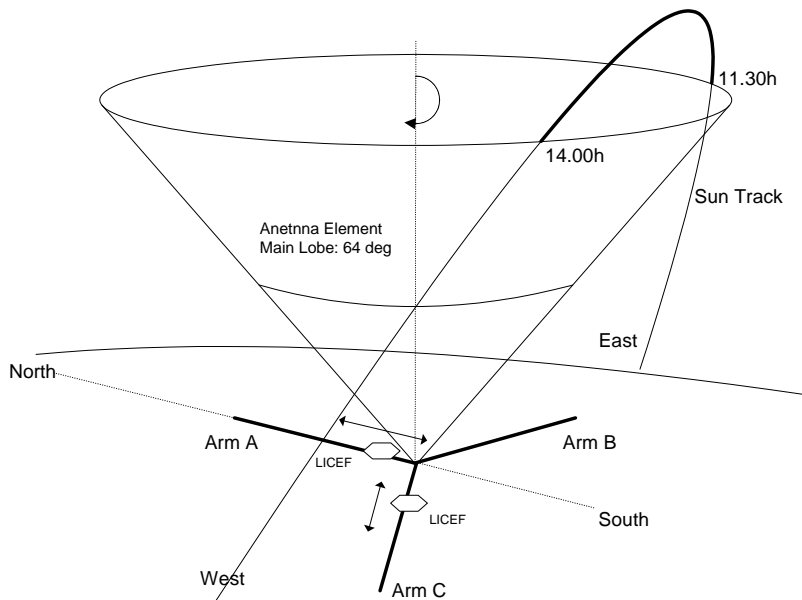
Figure 4.1: MIRAS pointing towards zenith when imaging the Sun.

The tracking of the Sun movement was done according to table 4.2, where the position of the sun was computed previously using [40]. Each position represents an angular increment of $1.5°$. Figure 4.2 shows how this tracking kept the synthetic beam pointing to the Sun. There the sky hemisphere is projected on the ξ, η plane. The unit circle represents the horizon; its aliases are also shown. The synthetic main beam for each tracking position of the array is shown by the small circles. The line with dots represents the path of the sun along the sky. The sun is pointed by the synthetic main beam in each tracking position. Figure 4.3 shows in a single picture the azimuth of the Sun and the tracking angle. It can be seen that this azimuth tracking follows almost perfectly the azimuth change of the sun.

The electrical setup is shown in figure 4.4. A common clock generator was connected to both receivers in order to demodulate the acquired signals coherently. The clock was also connected to the correlator. During calibration correlated noise was injected into the LICEF-1 receivers. This noise was generated

Electrical setup

Figure 4.2: Sun tracking for *Test 02* of IV-3B.

Figure 4.3: Sun azimuth and tracking for *Test 02* of IV-3B.

Table 4.2: Tracking position and time for *Test 02* of IV-test 3B.
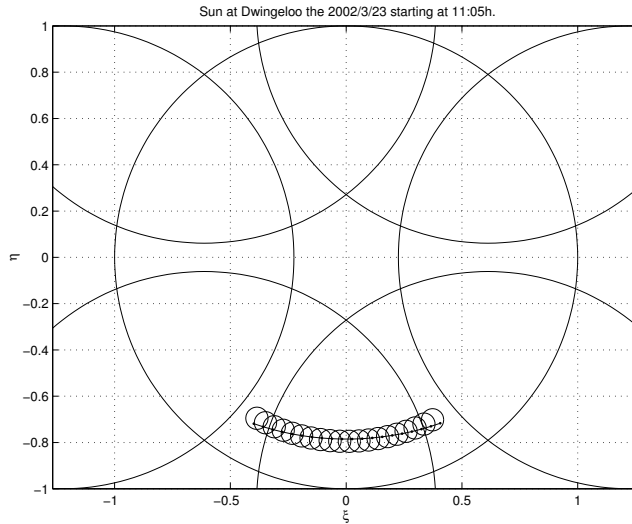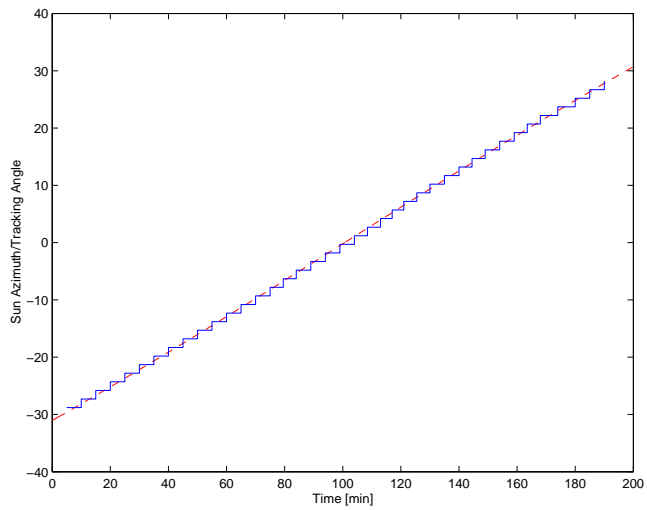
Tracking Position	Time	Tracking Position	Time
1	11:05	21	12:44
2	11:10	22	12:48.5
3	11:15	23	12:53
4	11:20	24	12:57
5	11:25	25	13:01
6	11:30	26	13:05.5
7	11:35	27	13:10
8	11:40	28	13:15
9	11:45	29	13:20
10	11:50	30	13:24.5
11	11:55	31	13:29
12	12:00	32	13:34
13	12:05	33	13:39
14	12:10	34	13:43.5
15	12:15	35	13:48
16	12:19.5	36	13:54
17	12:24	37	14:00
18	12:29	38	14:05
19	12:34	39	14:10
20	12:39		

by a noise source (ENR in the figure) and distributed to the receivers through a Noise Distribution Network (NDN). The digitised in-phase and quadrature signals (DI & DQ) of the receivers were fed into the correlator unit DICOS-3. The resulting correlations were saved with a PC. In parallel, the PMS of the LICEF-1's and the physical temperatures of the receivers were measured with a data acquisition unit. The PMS signal is an output voltage proportional to the input power to the receiver. This signal is generated by passing the input signal through a quadratic detector and then filtering it with a 0.641Hz low-pass filter. For measuring the physical temperature one thermocouple was attached to each of the receivers. PMS and temperature data were stored in another PC. The data was processed after all measurements had been taken.

A picture of the array is shown in figure 4.5. The control computers were
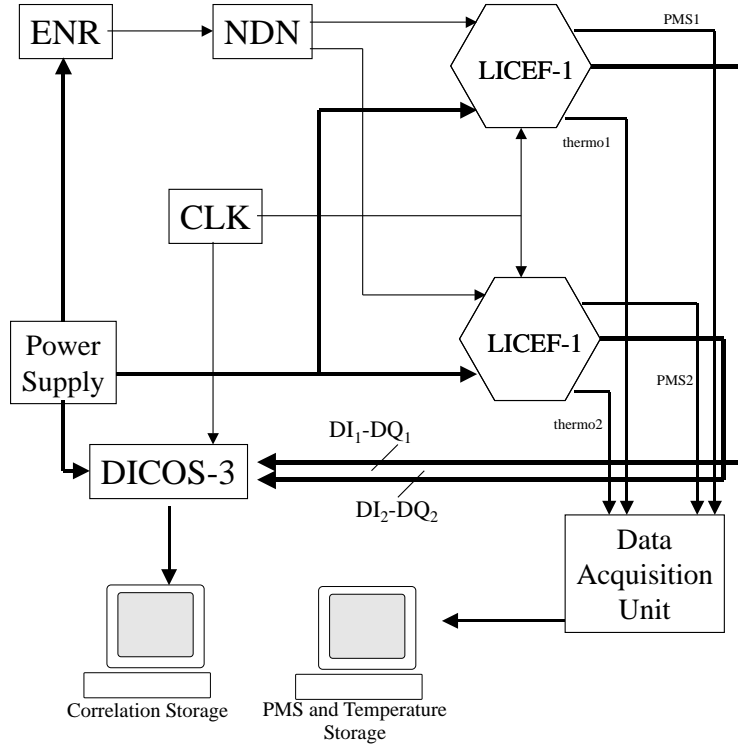
Figure 4.4: Electrical setup for the image validation tests.

placed inside a van, which acted as a Faraday cage, in order to reduce interferences to the LICEF-1 receivers. This is shown in figure 4.6. Table 4.3 summarises the tasks that have been carried out in order to prepare and perform the tests and the post processing of the acquired data.

Test procedure   The procedure of the test consisted in doing calibration measurements at the beginning and at the end of the experiment; the antenna measurements were done in between both calibrations. Figure 4.7 shows the PMS measurements of the Sun measurement *Test 02*. Calibration measurements at the beginning and at the end can be clearly distinguished from antenna measurements in between. Correlated and uncorrelated noise measurements can be observed. During the antenna measurements it can be seen that the PMS was very stable, despite

Figure 4.5: Image validation test 3B setup, MIRAS prototype with 9 elements per arm

Figure 4.6: Image validation test 3B auxiliary instrumentation setup inside a van

Table 4.3: Tasks performed during the image validation tests

Task	Description
Planning	The general setup and needed resources for making the test were identified.
Date selection and tracking	Code development and simulation on the Sun position and tracking requirements for keeping the Sun inside one synthetic beam.
Supporting structure	The supporting structure was designed to meet sub-millimetre bending requirements.
PMS and temperature acquisition	The PMS and temperature acquisition system was designed and implemented, using a data acquisition unit and writing the appropriate program.
Logistics	The logistic aspect of the campaign was managed.
Experiment coordination and execution	The experiment was carried out, coordinating baseline selection, baseline measurement and Sun tracking.
Data processing software	The data processing software responsible of calibrating the measurements and generating the modified brightness temperature image was done.
Data processing	The processing of the data and evaluation of the results was carried out.

the small peaks corresponding to the moments where the receivers were moved to a new baseline position. It was measured in H-polarisation only. The single power noise injection method was used to calibrate the Image Validation data. Only slight variations were done in order to adapt the method to the specificity of the test. Calibration and antenna measurements consisted in 100 and 20 measurements of 300ms respectively, which were averaged before any correction on the measurements were done.

4.1.2   A/D Converter Offset Calibration

A/D offset correction

The selected image for the experiment was a 2D delta type image. All the
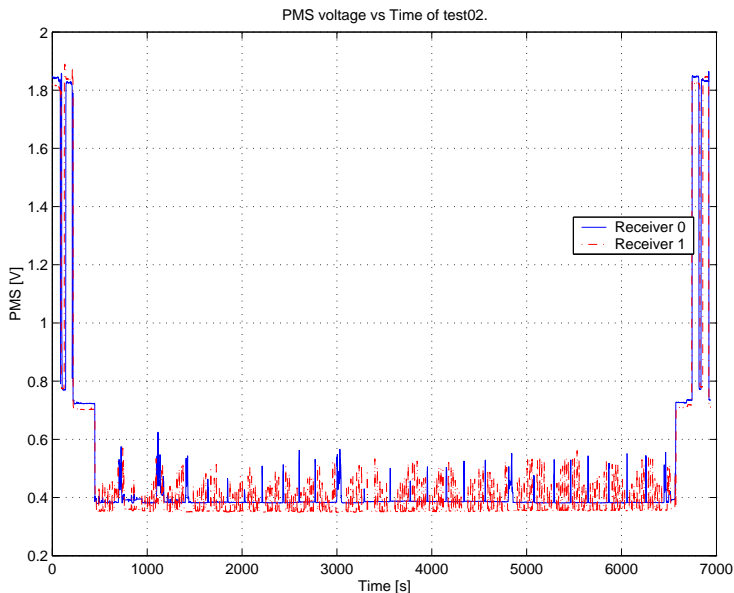
Figure 4.7: PMS sequence for Sun measurement *Test 02* of IV-3B.

measured complex correlations should present a similar amplitude, but a different phase. Thus an origin centred circumference should be observed when all measured complex correlations were plotted in the complex plain. Representing the measured correlations in the complex plane is a useful way to observe the baseline calibration method.

Figure 4.8 shows the raw correlations plotted in the complex plain. Two circumferences can be observed, one belonging to the IIQI correlations (blue circles), while the second one to the QQIQ correlations (green crosses). The former are called *nominal* correlations while the latter *redundant* correlations. However, the measured correlations do not give a circle centred at the origin due to the presence of an offset. This offset in the correlations is due to the non ideal A/D converters in the LICEF-1 receivers. This non-ideality introduces an offset in the measured correlations. After applying the 1&0 correction method described in section 3.4 and in [27, 30], the offset can be totally corrected for. No other source of repeatable correlation offset was observed, which should be
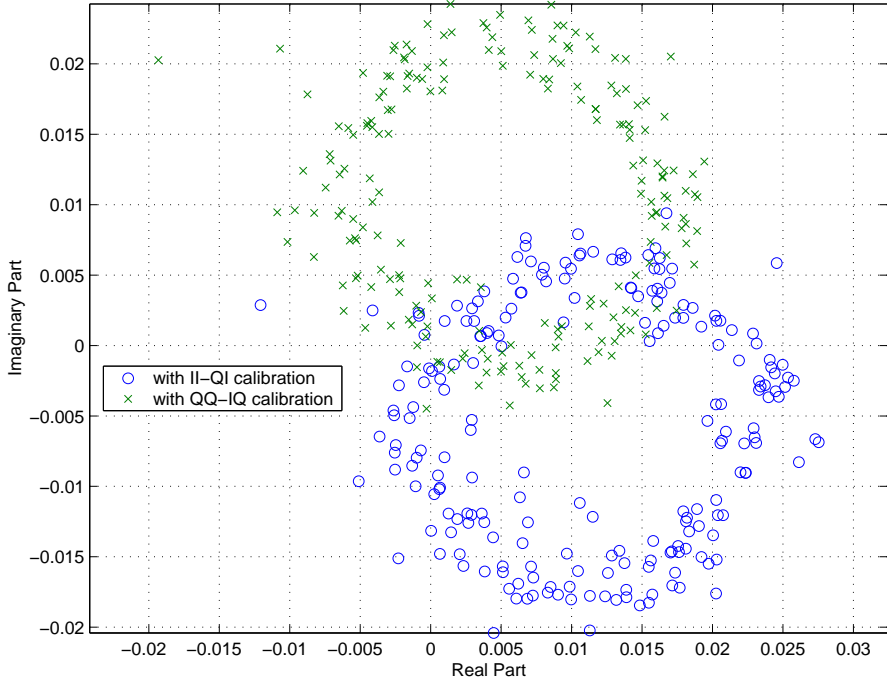
Figure 4.8: Raw correlations for the Sun imaging test *Test 02*.

corrected with the uncorrelated noise injection. Figure 4.9 shows that now the correlation circles are centred at the origin. It can also be appreciated that to each *nominal* correlation there is the corresponding *redundant* correlation with a similar value.

4.1.3 Phase-Error Calibration

Once the A/D induced offset in the correlations has been compensated for, the quadrature and in-phase errors are corrected using the equations of section 3.1 or [25, 26]. A slight modification has been made to this method in order to be able to evaluate the effect of the Noise Distribution Network on the retrieved
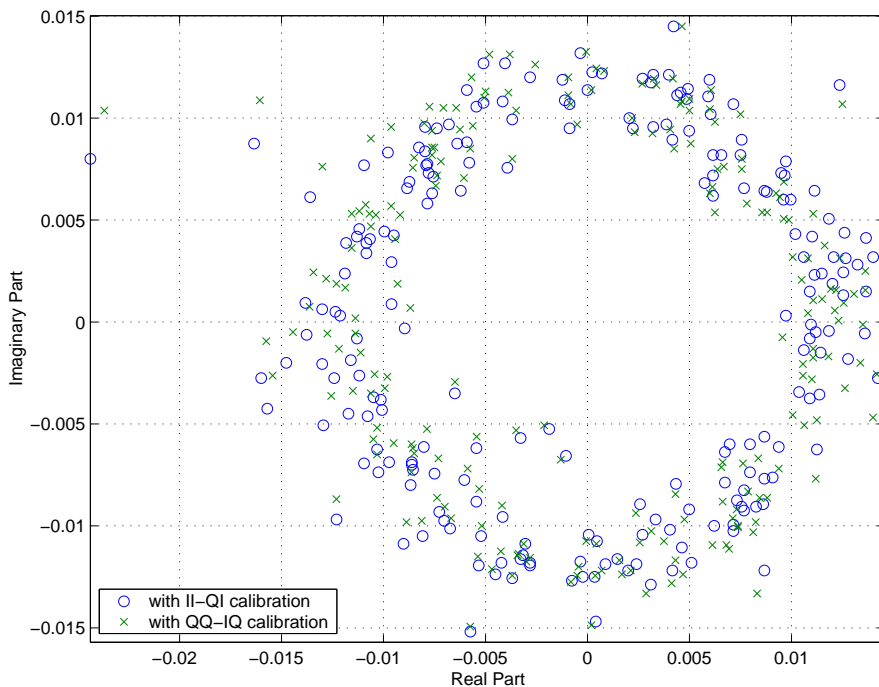
Figure 4.9: Offset corrected correlations for the Sun imaging test *Test 02*.

phase errors.

Figure 4.10 shows the setup of the noise injection during calibration. The noise generated by a noise source is fed into a passive network and then further on to the C-input of both receivers. The noise signals at the receivers input have suffered a phase shift β_1 and β_2 due to the branches 1 and 2 of the NDN. The phase difference between the signals of receivers 1 and 2 will be now

Phase errors

$$\alpha_{21} = (\theta_2 + \beta_2) - (\theta_1 + \beta_1) - \theta_{12} \tag{4.1}$$

as the phase shift introduced by the NDN adds directly to the phase shift introduced by the receivers. The angular term in the first parenthesis corresponds to the phase shift suffered by the signal, which passes the second branch of the
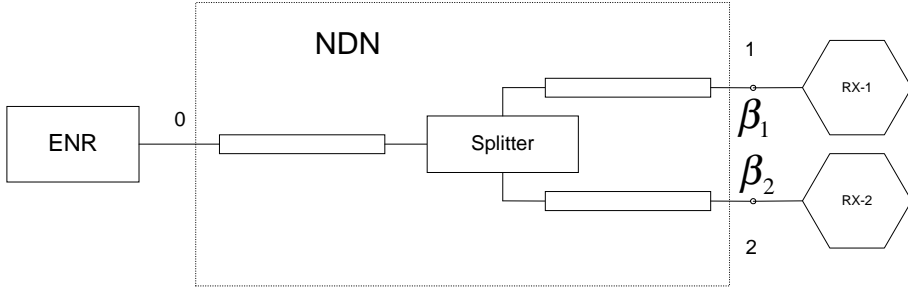
Figure 4.10: The Noise Distribution Network (NDN) introduces a phase error and an amplitude error during calibration if it is not well balanced.

NDN and the second LICEF. The second parenthesis corresponds to the phase shift suffered by the signal passing through the first branch of the NDN and the first LICEF. The α_{21} term can be estimated directly by using equation (3.13) or (3.14) of section 3.1, as if the NDN did not add any phase shift and the phase error was only due to the baseline.

During an antenna measurement, the NDN will not be present and thus the phase shifts β_2 and β_1 will not apply. Only the phase shifts θ_2, θ_1 and θ_{12} are of interests. A method for getting rid of the NDN induced phase shifts is the following.

NDN swapping If a new correlated noise measurement is done, but the output ports 1 and 2 of the NDN are now swapped and connected to the opposite LICEF-1, a new equation does apply for the phase shifts

$$\alpha'_{12} = (\theta_2 + \beta_1) - (\theta_1 + \beta_2) - \theta_{12} \tag{4.2}$$

Note that in (4.2) the phase errors β_1 and β_2 due to the NDN have now changed their sign with respect to (4.1). Combining the two in-phase measurements yields

$$\frac{1}{2}(\alpha_{12} + \alpha'_{12}) = \theta_2 - \theta_1 - \theta_{12} \tag{4.3}$$

$$\frac{1}{2}(\alpha_{12} - \alpha'_{12}) = \beta_2 - \beta_1 \tag{4.4}$$

Table 4.4: Error on the retrieval of the in-phase error of the noise distribution network compared to the network analyser measurement.

Measurement	$\Delta\beta$ (Error)
II/QI Start	$-0.15°$
II/QI Stop	$0.26°$
QQ/IQ Start	$0.26°$
QQ/IQ Stop	$-0.696°$

that is, we can separate the contribution to the phase error of the NDN from that of the LICEF-1's. Equation (4.4) gives the phase difference between the two paths of the NDN. Equation (4.3) gives the in-phase error only due to the receivers, which applies to every baseline measurement, when we are looking through the antenna.

When calibrating a baseline measurement, the in-phase error that should be taken into account is

$$\alpha_{12}^{cal} = \frac{1}{2}\left(\alpha_{12} + \alpha'_{12}\right) \tag{4.5}$$

Table 4.4 shows the error between the retrieved phases of the NDN with the procedure described previously and the phases measured with the network analyser. This can be used to evaluate the accuracy of the in-phase error calibration. A calibration at the beginning of the experiment and another one at the end were done. For both cases the difference is below one degree.

The in-phase error stability was also studied. For the the noise injection measurements 100 correlations of 300ms each were done. The in-phase error was estimated for each of these measurements. The results for the correlated noise measurement *ccorr1* are shown in figure 4.11. The same was done for three baseline chosen by random (*A2-B6*, *B4-C1* and *C7-A3*).Now 20 correlation measurements of 300ms each were taken. Figure 4.12 shows the in-phase error obtained from baseline measurement *C7-A3*. Both measurements show a certain degree of phase jitter, but it is much less in the case of correlated noise injection, about 1°, while the baseline measurement has a phase jitter of about 4°. An explanation for that may be found in the fact the correlated noise measurement is done with much more power, leading to larger amplitudes of the correlations, which results in a better phase stability.

The long term stability of the in-phase error was also studied. The in-phase
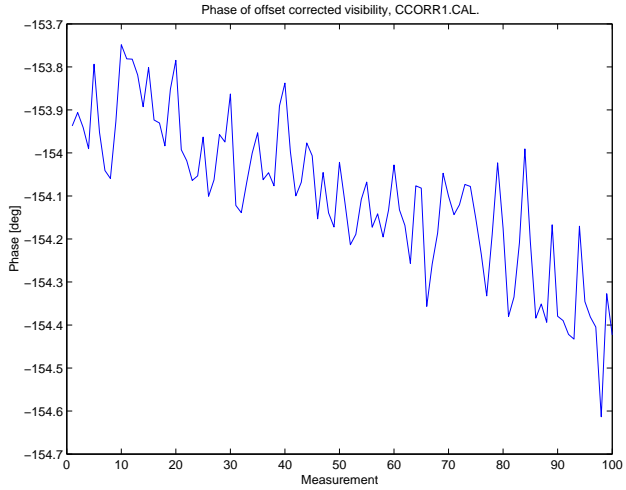
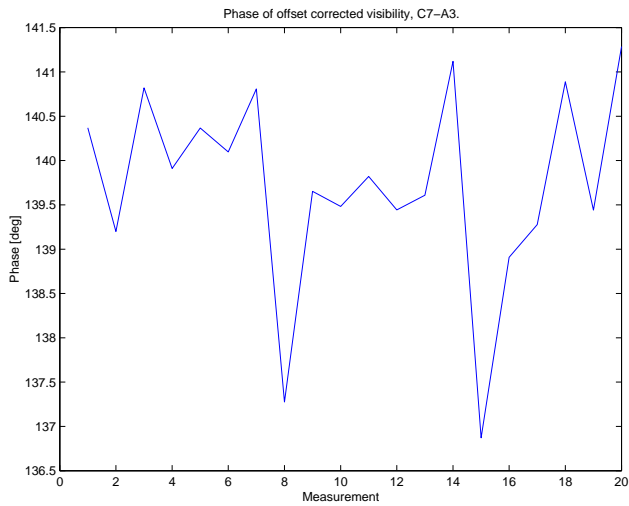Figure 4.11: Phase error estimation for correlated noise injection 1 $(100 \times 300\text{ms})$.

Figure 4.12: Phase error estimation for baseline *C7-A3*. $(20 \times 300\text{ms})$

Table 4.5: In-phase error for beginning and end calibrations

In-phase error	IIQI	QQIQ
$\alpha_{mn_{begin}}$	138.65°	138.59°
$\alpha_{mn_{end}}$	188.06°	188.09°

error at the beginning and end calibrations were obtained. Table 4.5 shows the obtained in-phase errors α_{12} for nominal (IIQI) and redundant correlations (QQIQ). The results show that very similar values were obtained for both correlation types, but they also show an important change in the in-phase error. Its value changed about 50° during a period of about two hours. This in-phase error drift can already be observed in the short time stability results of figure 4.11, besides the phase jitter a clear drift on the measured correlation phase can be observed. This drift of the in-phase error has been taken into account during calibration. The in-phase error that has been used to calibrated each individual baseline has been obtained from making a linear interpolation of the beginning and end value of α_{12} and taking into account the time that passed between the calibration events and the baseline measurement. This improved the Sun image notably, making the synthetic main beams very sharp, as will be shown later.

4.1.4 Amplitude Calibration

The last step to be applied in the single-power noise-injection calibration-method is the calibration of the amplitude of the measured baselines. In MIRAS a dedicated noise injection radiometer (NIR) measures the antenna temperature corresponding to the observed scene. Unfortunately, in the MIRAS prototype used during the image validation tests this device was not available. Thus, the antenna temperature T_A had to be estimated in another way. For that the PMS output of the receivers was used. The calibration of the PMS response was done as a typical linear response calibration, measuring two points of the straight line.

$$v = mT_{in}^C + b \tag{4.6}$$

where T_{in}^C corresponds to the equivalent noise temperature injected into the port C and v to the obtained PMS voltage. m and b are the calibration parameters that have to be estimated. During the injection of correlated noise through the C-port for the measurement of the phase errors of the receivers the PMS voltage was also measured. In that measurement also the input noise temperature to

the receivers was known. This was the so called *hot* measurement. A second measurement using the internal matched load connected to the U-port of the LICEF-1, was also done. As this load was at ambient temperature it is referred to as *warm* measurement.

With this consideration a hot temperature, corresponding to the correlated noise injection and a warm temperature corresponding to the uncorrelated noise injection have been used as reference points to estimate as a first step the PMS response at the C-port.

The signal paths from the different input ports to the input switch are physically different in LICEF-1. Thus, the model for the input part of the receivers of figure 4.13 has been used. The figure shows the input switch, which is considered ideal, i.e., with equal behaviour for each channel of the switch, and a lossy line from the input ports of the receiver to the switch. The attenuation of these lines is different for each port.
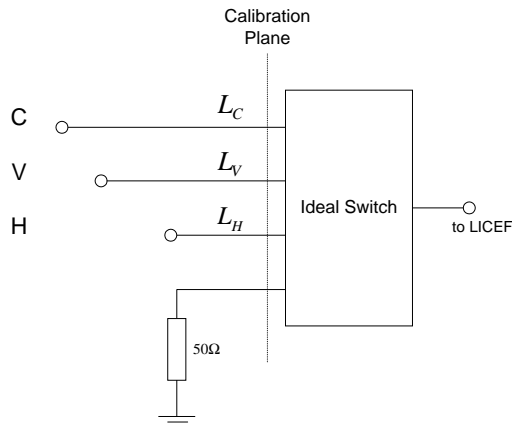
Figure 4.13: Ideal input switch model for LICEF-1.

During calibration port C is used and thus, in principle, the calibration is only valid for this port. With hot and warm noise injections into port C the parameters m and b of equation (4.6) are obtained. The warm noise injection was in fact done by connecting the switch to the U-position where a matched load is directly connected to the switch. This is equivalent to connect a matched load at the C-port, when the whole system (loads and lossy line) is at the same

physical temperature.

But during the scene measurement the switch is connected to the port H and the previous calibration is useless if the different attenuations of the lines at the C-port and the H-port are not taken into account. Thus the following calibration curve is valid for the antenna port H

$$v = m'T_{in}^H + b' \tag{4.7}$$

where now T_{in}^H is the equivalent input temperature at port H and v the corresponding measured voltage. m' and b' are the calibration parameters of port H.

The calibration parameters of port C, m and b can be related to the calibration parameters of port H, m' and b'. During noise injection into port C we can compute the equivalent noise temperature at the input plane of the switch. This is given by

$$T_{switch} = \frac{T_{in}^C}{L_C} + \frac{L_C - 1}{L_C}T_0 \tag{4.8}$$

where T_{switch} is the equivalent noise temperature at the input of the switch (in figure 4.13 indicated as *Calibration Plane*), T_{in}^C is the injected noise temperature at port C, L_C is the attenuation of the line that goes from port C to the switch input and T_0 is the physical temperature of the line.

A similar equation can be written for port H, when this port is selected by the input switch

$$T_{switch} = \frac{T_{in}^H}{L_H} + \frac{L_H - 1}{L_H}T_0 \tag{4.9}$$

being T_{switch} the equivalent noise temperature at the input of the switch, T_{in}^H the antenna temperature fed into port H, L_H the attenuation of the line between port H and the switch and T_0 the physical temperature of the line.

Combining equations (4.8) and (4.9) yields

$$\frac{T_{in}^C}{L_C} + \frac{L_C - 1}{L_C}T_0 = \frac{T_{in}^H}{L_H} + \frac{L_H - 1}{L_H}T_0 \tag{4.10}$$

Using (4.6) and making some operations the result

$$T_{in}^H = \frac{L_H}{L_C}\left(\frac{v - b}{m}\right) - \frac{L_H}{L_C}T_0 + T_0 \tag{4.11}$$

is obtained. This equation can be rewritten as

$$v = m\frac{L_C}{L_H}T_{in}^H + mT_0 - m\frac{L_C}{L_H}T_0 + b \tag{4.12}$$

From this equation can be seen that only the ratio L_H/L_C between the attenuations of both lines has to be known and not their absolute values, in order to obtain the equivalent temperature injected in port H, with a calibration corresponding to port C. Furthermore, the calibration parameters m' and b' are related to m and b by

$$m' = m\frac{L_C}{L_H} \tag{4.13}$$

$$b' = b + mT_0(1 - \frac{L_C}{L_H}) \tag{4.14}$$

These results say that any calibration plane can be used for the PMS calibration, provided the ratio between attenuations of the calibration plane to the input port for the C and H ports is known. The inconvenient of these results are that the uncertainty in the estimation of L_C/L_H is multiplied by the physical temperature $T_0 \approx 300\text{K}$, resulting in a higher uncertainty in the estimation of b'.

In practice it will be much easier to define a calibration plane just at the switch plane (see figure 4.13) and relate all the measurements to that plane. Another approach is to put the calibration plane at the H-port. In this way the additional attenuation of the transmission line of port H can be supposed equal to zero as it will be included in the calibration, while the additional attenuation of port C will be L_C/L_H, making the computations easier. The factor L_C/L_H describes the additional attenuation in port C of the receiver respect to a calibration plane defined at port H.

Figure 4.14 shows a typical PMS response curve and its calibration points, related to the calibration plane at port H. Thus the *warm* and *hot* temperature points shown in the figure do not correspond to the injected temperature into port C, but to this injected temperature transformed to the calibration plane of port H.

The amplitude response of LICEF-1 receivers have been measured for all input ports. The gain difference between ports C and H has been assumed to be only due to the different attenuations of the input lines. In this case the values were $L_{C1}/L_{H1} = 0.94\text{dB}$ and $L_{C2}/L_{H2} = 0.85\text{dB}$.[2]

Temporal interpolation of PMS

A refinement of this PMS calibration method has also been done to take into account drifts of the instrument during time. A PMS calibration has been done before starting to measure all the baselines (at $t = t_0$) and after having done all

---

[2]These values were obtained from the mean value of the amplitude responses (C and H channels) in the 8-27MHz band of the LICEF's.

the measurements $(t = t_1)$, obtaining thus

$$v_{PMS_0} = m_0 T_{in} + b_0 \tag{4.15}$$

$$v_{PMS_1} = m_1 T_{in} + b_1 \tag{4.16}$$

The subindex 0 means *calibration at the beginning* and 1 *calibration at the end.* When the PMS voltage corresponding to an antenna temperature measurement has been done, also the time of measurement has been recorded $(t = t_A)$. The antenna temperature for begin (T_{A0}) and end (T_{A1}) has been be obtained from the previous equations and finally a linear interpolation taking into account the measurement time has been done.

$$T_A = T_{A0} + \frac{t_A - t_0}{t_1 - t_0}(T_{A1} - T_{A0}) \tag{4.17}$$

This is the estimation of the antenna temperature that has been used in this
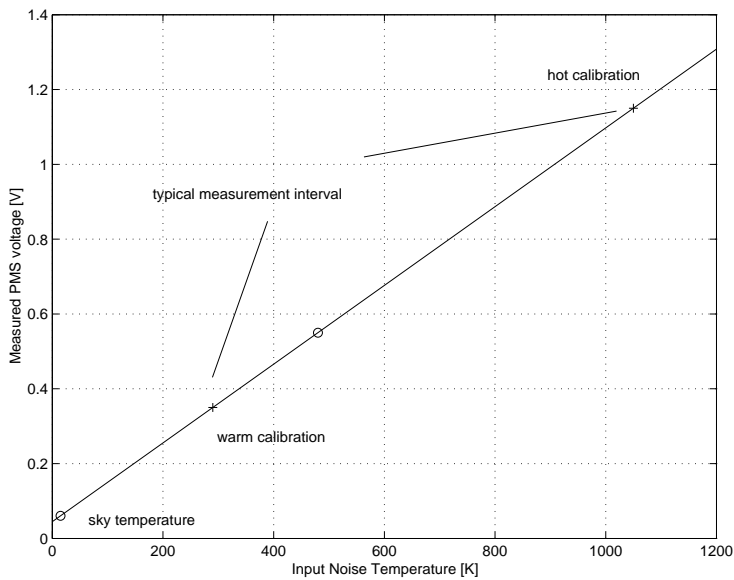
Figure 4.14: PMS calibration curve example, with hot and warm calibration points, typical measurement interval and antenna temperature measurements for the sky.

image validation test, due to the absence of a NIR.

The amplitude calibration equations of [25, 26] given in section 3.1 were used to fully calibrate the measured correlations, obtaining the result which is presented in figure 4.15. It should be remarked that at this point the *nominal* and *redundant* correlations got scattered respect to each other. This is an indicator that the amplitude calibration is not good enough. This will get clearer when the absolute value of the sun brightness temperature is estimated.

Figure 4.15: Totally calibrated correlations for the Sun imaging test *Test 02*.

4.1.5 Fringe-Washing Function

The normalised fringe-washing function (FWF) for the LICEF receiver pair
FWF shape has been measured, (although the obtained results have not been used for the

Figure 4.16: Schematic diagram for the fringe-washing function measurement setup.

image processing). This has been done using the correlated noise injection measurement at the beginning of the experiment. The schematic diagram of the setup is shown in figure 4.16. The DI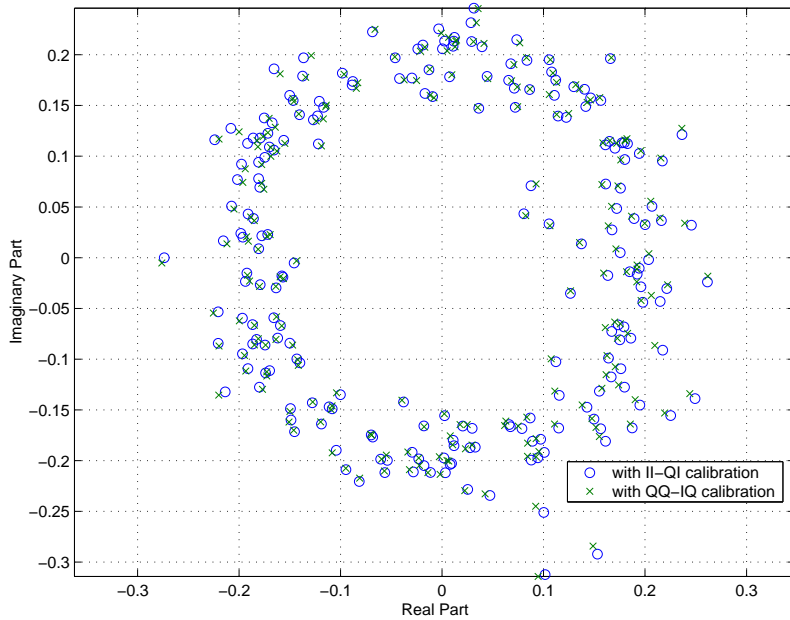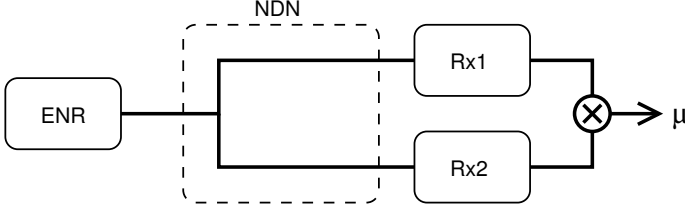COS-3 correlator performs correlations simultaneously at $\tau = 0$ (*punctual*), $tau = +T$ (*early*) and $\tau = -T$ (*late*), being $T = 1/55.84MHz$ one time lag. With these three correlation measurements the fringe-washing function can be estimated using the three delay method [41, 42]. This method consists in adjusting a *sinc* function to the modulus of the fringe-washing function and a 2nd degree polymonial to its phase.

$$
\begin{aligned}
|\tilde{r}_{ij}| &\approx A \cdot \text{sinc}\left[B\left(\tau - C\right)\right] & (4.18)\\
\arg\left(\tilde{r}_{ij}\right) &\approx D\tau^2 + E\tau + F & (4.19)
\end{aligned}
$$

with

$$
\begin{aligned}
D &= \left[\frac{\phi_T + \phi_{-T}}{2} - \phi_0\right]\frac{1}{T^2} & (4.20)\\
E &= \frac{\phi_T - \phi_{-T}}{2}\frac{1}{T} & (4.21)\\
F &= \phi_0 & (4.22)
\end{aligned}
$$

Note that during the calibration, the phase error introduced by the NDN is also calibrated as it would be part of the receiver. Similarly happens to the amplitude factor introduced by the NDN, but this does not represent a problem since the normalised and not the absolute fringe-washing function is measured.

Figure 4.17 shows the measured fringe-washing functions obtained for the IIQI correlations and the QQIQ correlations. The fringe-washing function has been measured for the two possible positions of the NDN, the nominal and the one swapping both output channels and connecting them to the opposite
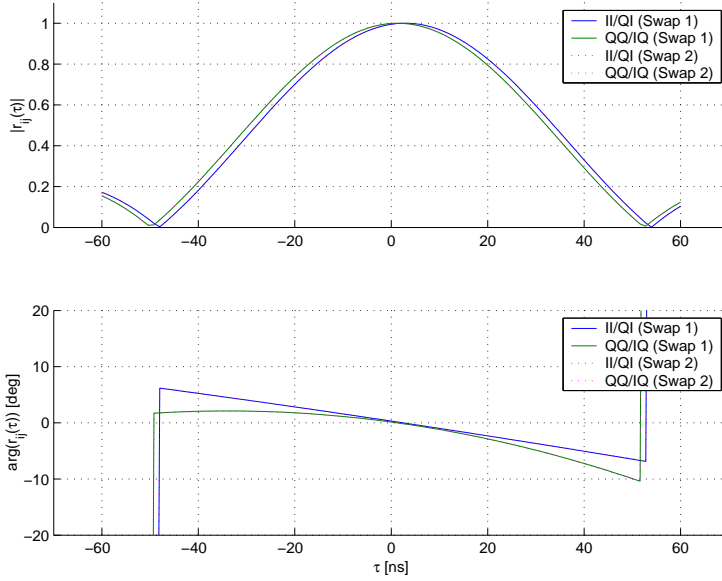
Figure 4.17: Measured (3 delay method) fringe-washing functions.

receivers. The obtained results show that there is no dependence in the position of the NDN, but that there is a slight difference when the fringe-washing function is measured with the nominal (IIQI) correlations or the redundant ones (QQIQ). The exact values for A, B, C, D, E and F are given in table 4.6. The only important difference can be found for parameter D when comparing the result using the nominal or redundant correlations. This is due to the fact that we are estimating the quadratic term of the phase and the phase itself behaves very linearly, inducing thus an important error in the estimation of D.

The estimated fringe-washing functions have been compared to the ones of figure 5 of [42]. There the front-end filter-response of exact the same LICEF's has been used to compute the fringe-washing function with

$$|\tilde{r}_{ij}| = \frac{1}{\sqrt{B_1 B_2}} \int_{-f_0}^{\infty} H_{1,n}(f) H_{2,n}(f) e^{j2\pi f\tau} \mathrm{d}f \qquad (4.23)$$

The coincidence between both results is very good.

Table 4.6: Fringe-washing function estimation parameters

Parameter	Swap 1 IIQI	Swap 1 QQIQ	Swap 2 IIQI	Swap 2 QQIQ
A[†]	1.0053	1.0011	1.0083	0.9989
B [MHz]	19.597	19.551	19.590	19.558
C [ns]	2.8802	1.3115	2.8799	1.3135
D [kHz/ns]	-0.765	-9.4872	-0.6346	-9.6375
E [kHz]	-394.39	-322.37	-357.10	-322.94
F [deg]	0	0	0	0

[†] Note that some values for A are larger than one, because the FWF has been normalised by its value at the origin. In figure 4.17 the FWF have been scaled down in order to have a maximum value of 1.

4.1.6 Sun Image

Once all the baselines have been calibrated obtaining the visibilities, the modified brightness temperature of the measured scene in the direction cosine domain (ξ, η) plane was obtained with a DFT[3]

$$\hat{T}(\xi, \eta) = \Delta s \sum_k w(u_k, v_k) V(u_k, v_k) e^{j2\pi(u_k\xi + v_k\eta)} \qquad (4.24)$$

where the summation over k is the summation for all the measured visibilities, $w(u_k, v_k)$ is the apodisation window, $V_k = V(u_k, v_k)$ are the visibility samples and u_k, v_k are the points where the visibility function has been sampled. $\Delta s = d^2\sqrt{3}/2$ is the area of the grid's elementary cell and d the spacing between antenna elements.

The Blackman appodisation window has been used in the results presented here. The window has circular geometry around the origin of the (u,v) plane and is given by

$$w(u, v) = 0.42 + 0.5\cos\left(\pi\frac{\rho}{\rho_{max}}\right) + 0.08\cos\left(2\pi\frac{\rho}{\rho_{max}}\right) \qquad (4.25)$$

with

$$\rho^2 = u^2 + v^2, \quad \rho_{max} = \sqrt{3}N_{EL}d \qquad (4.26)$$

being N_{EL} the maximum number of elements per arm, d the spacing between elements and u, v the coordinates of the baseline.

---
[3]DFT stands for Discrete Fourier Transform
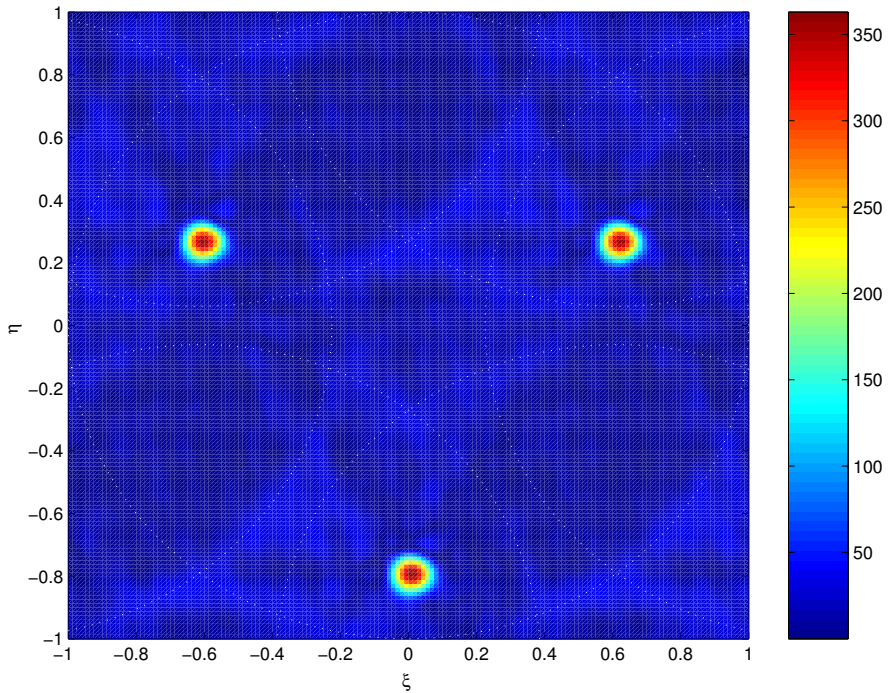
Figure 4.18: Modified brightness temperature with Blackman apodisation window for the Sun imaging test *Test 02*.

Imaging with Blackman window

Figure 4.18 shows the absolute value of the modified brightness temperature of the Sun image generated with the Blackman apodisation window. The axes correspond to the (ξ,η) plane, being the area inside the unity circle a projection of the sky hemisphere. The unity circle corresponds to the horizon, while the other circles are the aliases of the horizon. The real sun image is the one at the lower side of the image at the position were it was expected to appear. The other two suns are only alias images. The main lobe is defined clearly and even the secondary lobe structure can be seen although not perfectly. Even at the horizon a small increment of the modified brightness temperature can be appreciated. The same can be seen at the aliases of the horizon.
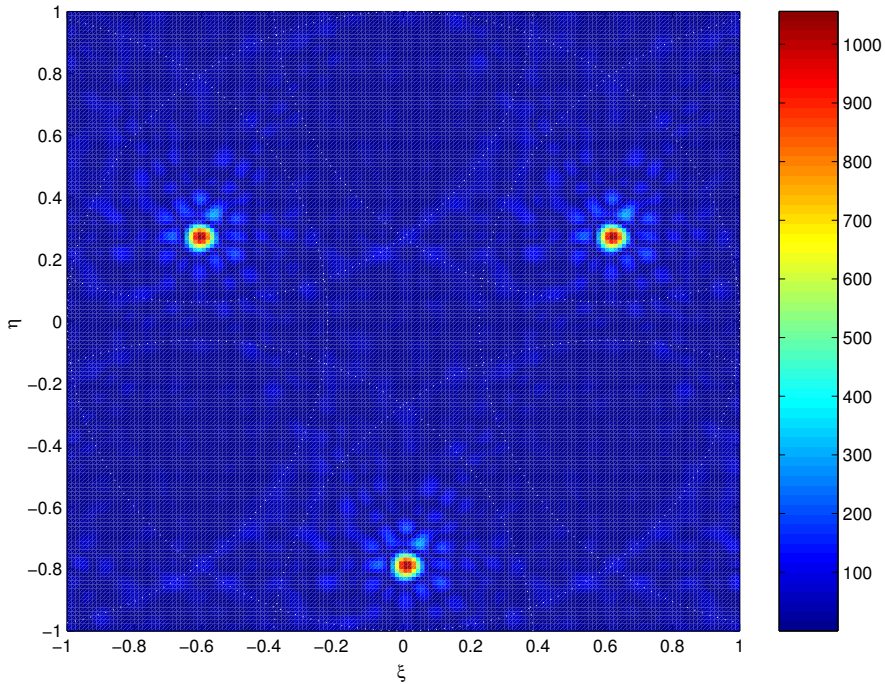
Figure 4.19: Modified brightness temperature with rectangular apodisation window for the Sun imaging test *Test 02*.

If a rectangular apodisation window is used, instead of Blackman, the secondary lobe structure gets much defined, as the secondary lobes are higher and narrower. This also makes that the horizon signature to be a narrower as with the Blackman window generate image. This is shown in figure 4.19.

Making a zoom of the alias free zone of Blackman window generated image it can be seen that the modified brightness temperature of the sky is below 20K (see figure 4.20)[4]. Some variations on the modified brightness temperature can

Imaging with rectangular window

Alias free sky image

---

[4]In fact, using the most up to date formulation of the visibility function [22] the modified brightness temperature for the sky zone should be negative as it is proportional to $T_{sky} - T_r \approx -200K$, being T_r the receiver noise temperature. This was not known at the time of

Figure 4.20: Modified brightness temperature (alias free zone) with Blackman apodisation window for the Sun imaging test *Test 02*.

be observed. The reason for that may be found in the secondary lobes of the horizons, which enter the alias free field of view of the centre of the image. Note also that during the experiment the sun was tracked with an azimuthal rotation, keeping the sun within the same synthetic beam all the time, but blurring the rest of the image, as other parts of the image were not tracked. This originates a blurring of the other parts of the image and thus some unpredictable undulations may appear there.

---

the experiment and thus the absolute value of the brightness temperature was plotted and interpreted.
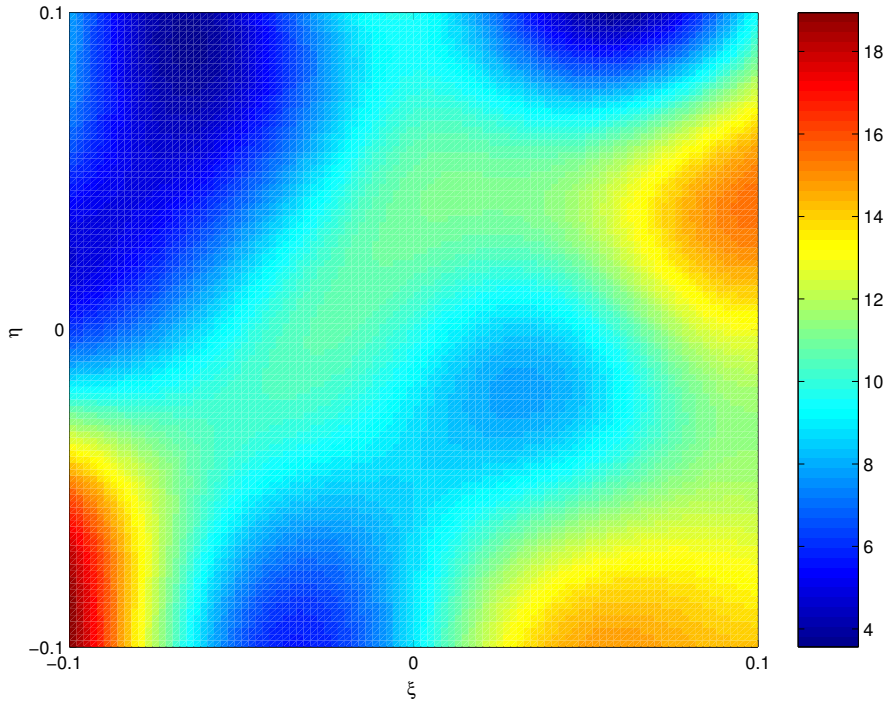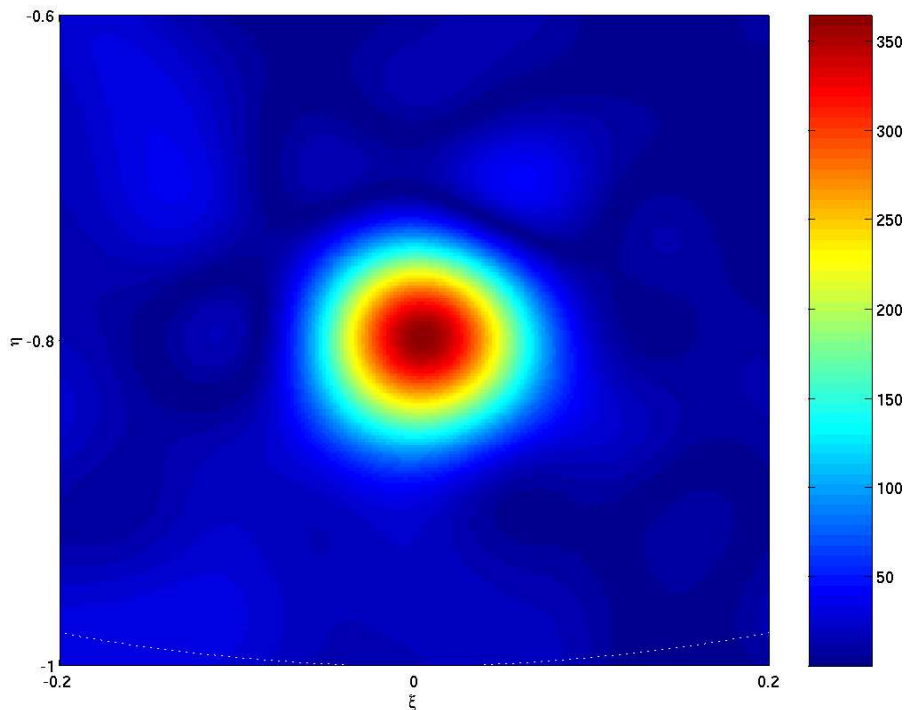
Figure 4.21: Modified brightness temperature (main beam) with Blackman apodisation window for the Sun imaging test *Test 02*.

The main beam, corresponding to the real sun (Blackman window) can be appreciated in figure 4.21, where it is very clearly shown. The shape of it is almost perfectly circular indicating that calibration procedures have been successful. Because the sun is practically a point source for the synthesised antenna, the sun image can be used to obtain a good estimate the synthesised beam width. Its measured size at 3dB using the Blackman apodisation window is $5.7° \times 10\circ$, which is in good accordance with the theoretical beam of $5.5° \times 9.7°$. [33].

Around the main lobe six secondary lobes should appear (as can be seen in the simulated main lobes of figure 5.4(b) of page 113). The measurement shows them also, although some of them appear completely blurred.

4.2 HUT-2D Segment Calibration

During a three month stage at the Laboratory of Space Technology (LST) of the Helsinki University of Technology (HUT) from August to October 2002 research on the calibration of the HUT-2D radiometer was done. The design of HUT-2D is based on segments consisting of four receivers. Several four-receivers segments are joined to give the complete HUT-2D instrument. This research consisted basically in performing calibration tests with the first four-receivers segment of the HUT-2D synthetic aperture radiometer [43, 44] and investigate new ways to improve its performance.

The HUT-2D radiometer is a synthetic aperture radiometer based on the same concept as MIRAS. It was designed to be a prototype aircraft demonstrator of the technology to be used during the SMOS mission. Thus, the same calibration techniques as the ones designed for the MIRAS radiometer are used in HUT-2D. The principal differences are their shapes (MIRAS has three-arm Y-shape, while HUT-2D has U-shape), receiver spacing and bandwidth, but conceptually they are the same.

4.2.1 Experiment Setup

HUT-2D experiment setup

The first manufactured four-receiver segment was tested. Figure 4.22 shows the schematics of the setup with the four-receivers segment. Each of the four receivers had on the top of it two patch atennæ at horizontal and vertical polarisations. Four input signals could be selected for each receiver (C, U, H, V). This was done controlling the input switch of each receiver. C port was used to inject correlated noise to the receivers, which had been generated with a noise source (ENR) and then distributed to each of the receivers using the passive noise distribution network (NDN). U port was connected to an internal matched load at ambient temperature. Using this port uncorrelated noise was injected into each receiver. Finally, H and V ports were connected to the horizontally and vertically polarised antennas of each receiver, respectively. C and U ports should be used during calibration of the baselines, while H and V during antenna measurements.

The digitised I and Q signals of each receiver is input into the correlator unit, which computes the correlations between all receiver pairs. A computer reads this data and stores the correlations.

With these four receivers, named 1 to 4, six different baselines could be formed, namely, (1-2), (1-3), (1-4), (2-3), (2-4) and (3-4). This allowed to test the calibration procedures not only on one receiver pair, as was done in the
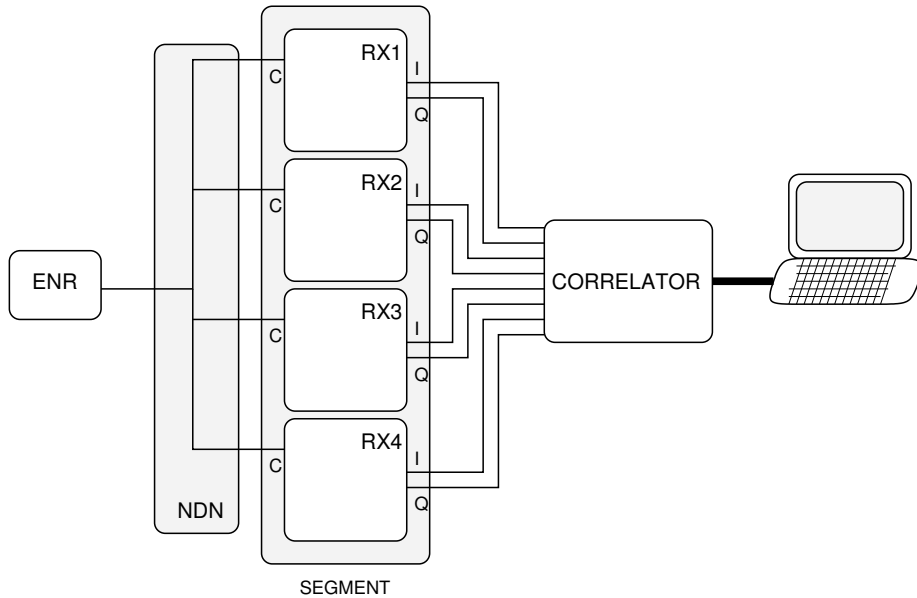
Figure 4.22: Schematic of the HUT-2D segment used to validate calibration procedures.

Dwingeloo experiments, but to test them directly for six different baselines.

4.2.2 A/D Converter Offset Calibration

Uncorrelated noise was injected into the four receivers, with the aim of proving the 1&0 A/D offset correction technique from [27, 30] with this new hardware. The results are shown below.

A/D offset
calibration

Figure 4.23 shows the measurement of the complex correlation of uncorrelated noise for baseline 1-2. The ideal correlation value is thus zero, but due to finite integration time some additive noise will be present in the measurements. Thus, a cloud of measurements close to zero (with its mean value equal to zero) is expected. The offset of the sampling comparators has artificially been put different to zero by adjusting the voltage at one input of the comparator, and this translates to an offset in the correlation value as can be seen in the figure (with a crosses). After applying the offset correction method the cloud (with circles) moves to the origin confirming that the method is able to correct the
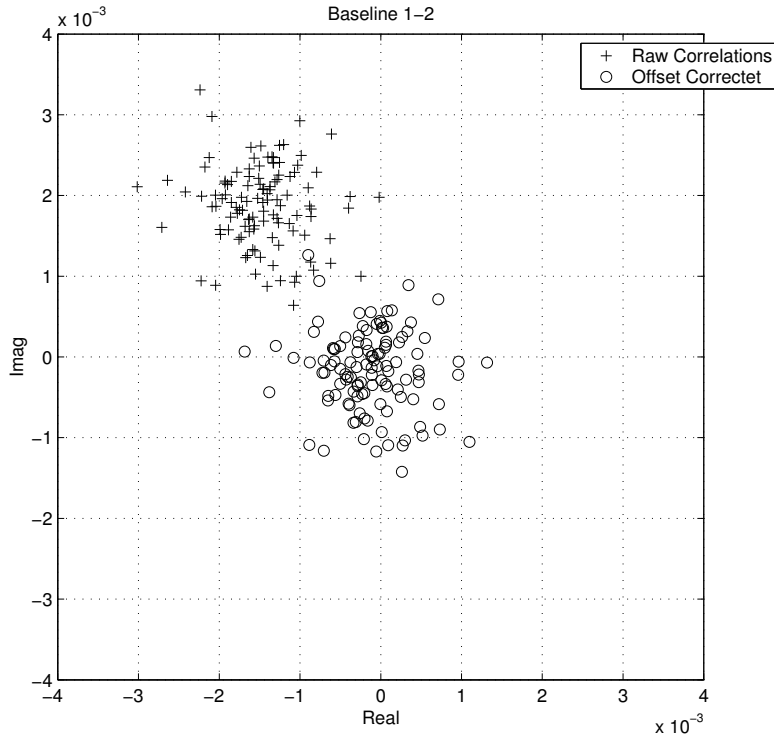
Figure 4.23: Offset correction for baseline 1-2 with unbalanced sampling comparators.

correlation offset due to non ideal A/D converters.

Figure 4.24 shows the correlations when the offset voltage of the A/D converters has been adjusted very close to zero for baseline 1-2. It can be observed that in that case the correlations have no offset (with crosses) and that after applying the corrections (with circles) the measured values remain the same, that is, the 1&0's method does not act when there is not offset. This results complement the previous ones, confirming that it is a robust method for compensating the effect of A/D comparator offset on the measured correlations.
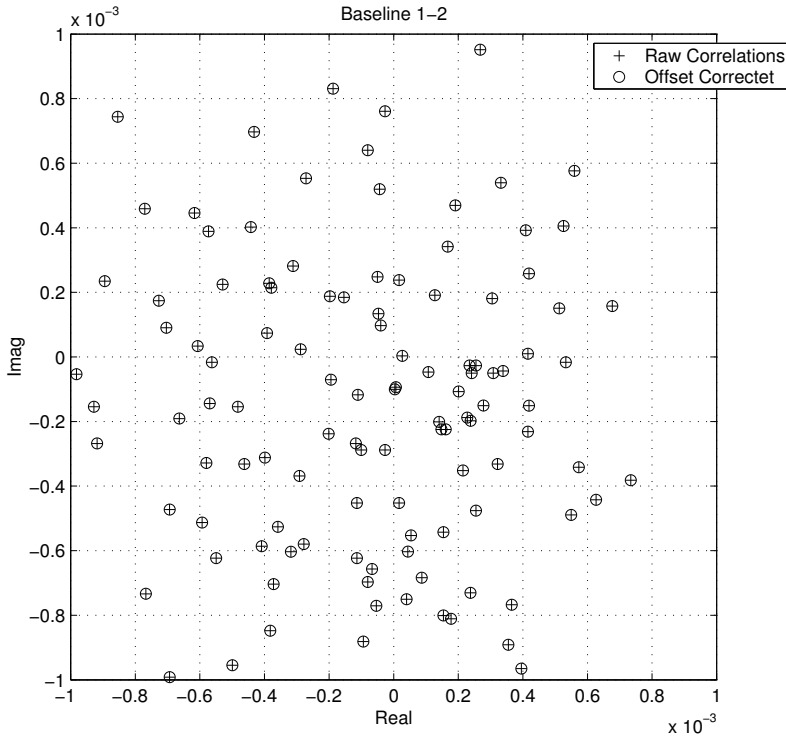
Figure 4.24: Baseline 1-2, when no offset is present 1&0 correction has no effect.

4.2.3   Quadrature Error Calibration

Many calibrations have been done in order to check the time stability of the instrument. 13 different noise injection calibrations have been performed during one hour, one every 5 minutes. Each calibration consisted in 60 measurements with a correlation time of 1000ms. Each of the 60 measurements has been used as a calibration and from this results mean values and standard deviation have been obtained.

> Quadrature error stability

The results of the calibration using the method described in [26] are presented. Table 4.7 shows the quadrature error results when the correlation between I and Q signals of a single receiver are used. The measured standard

Table 4.7: Quadrature error during stability test using CAS-D method (mean value).

RX: Meas.	1	2	3	4
CAL01	2.28°	13.42°	8.77°	3.68°
CAL02	2.29°	13.43°	8.78°	3.70°
CAL03	2.29°	13.43°	8.78°	3.71°
CAL04	2.29°	13.43°	8.78°	3.71°
CAL05	2.30°	13.43°	8.78°	3.71°
CAL06	2.29°	13.43°	8.78°	3.71°
CAL07	2.30°	13.43°	8.78°	3.71°
CAL08	2.29°	13.43°	8.78°	3.70°
CAL09	2.29°	13.43°	8.78°	3.71°
CAL10	2.29°	13.43°	8.79°	3.71°
CAL11	2.29°	13.43°	8.78°	3.70°
CAL12	2.29°	13.43°	8.78°	3.71°
CAL13	2.29°	13.43°	8.78°	3.71°

deviation in the retrieval of the quadrature error is 0.01° for all cases.

The quadrature errors have also been estimated using the method described in [25], equation (16), where in-phase errors and quadrature errors are retrieved simultaneously from the noise injection measurements using numerical methods. The results for the quadrature error of the receivers are presented in table 4.8 It can be clearly seen that the mean value is almost constant. The standard deviation of the retrieved quadrature errors is 0.02 degrees for almost all cases except two where it is 0.03.

This low standard deviation for both cases shows that the calibration method is very precise for obtaining the quadrature error of the receivers and that the receivers are very stable in the period of one hour and in a stable ambient.

4.2.4   In-Phase Error Calibration

In-phase error stability

The in-phase errors have been also estimated using [25] for the four-receiver segment, using the same measurements as for the quadrature error calibration. 13 different noise injection calibrations have been performed during one hour,

Table 4.8: Quadrature error retrieval using [25] during stability test (mean value).

RX: Meas.	1	2	3	4
CAL01	2.29°	13.37°	8.80°	3.77°
CAL02	2.30°	13.39°	8.81°	3.79°
CAL03	2.30°	13.39°	8.81°	3.79°
CAL04	2.30°	13.39°	8.81°	3.79°
CAL05	2.30°	13.39°	8.81°	3.79°
CAL06	2.30°	13.39°	8.81°	3.79°
CAL07	2.30°	13.39°	8.81°	3.79°
CAL08	2.30°	13.38°	8.81°	3.79°
CAL09	2.30°	13.39°	8.81°	3.80°
CAL10	2.30°	13.39°	8.81°	3.79°
CAL11	2.30°	13.39°	8.81°	3.79°
CAL12	2.30°	13.39°	8.81°	3.79°
CAL13	2.30°	13.39°	8.81°	3.80°

one every 5 minutes. Each calibration consisted in 60 measurements with a correlation time of 1000ms. Each of the 60 measurements has been used as a calibration and from this results mean values and standard deviation have been obtained. The in-phase errors retrieved for the four receivers are presented in tables 4.9. Also for the in-phase error retrieval it can be seen that the standard deviation is very small (0.03 degrees), showing that the proposed calibration method is very precise for obtaining the in-phase and quadrature method. The results also show that the receivers have a very stable in-phase error, when they are in a stable environment.

4.2.5 Phase-Calibration as a Function of Injected Power

Injecting high-power correlated noise improves the calibration of the phase errors of the baselines, as the signal to noise ratio is increased, but it also demands a higher dynamic range to the receivers in order to handle the high power. Thus, a series of calibrations with different input power levels have been done in order to evaluate which is the best power range to be used during calibration. For

Table 4.9: In-phase error during stability test (mean value).

RX: Meas.	1	2	3	4
CAL01	0.00°	0.75°	31.09°	-12.38°
CAL02	0.00°	0.83°	31.09°	-12.33°
CAL03	0.00°	0.73°	31.08°	-12.31°
CAL04	0.00°	0.77°	31.09°	-12.30°
CAL05	0.00°	0.66°	31.05°	-12.33°
CAL06	0.00°	0.68°	31.03°	-12.35°
CAL07	0.00°	0.73°	31.02°	-12.35°
CAL08	0.00°	0.74°	31.01°	-12.35°
CAL09	0.00°	0.80°	31.02°	-12.34°
CAL10	0.00°	0.78°	31.01°	-12.32°
CAL11	0.00°	0.78°	30.98°	-12.32°
CAL12	0.00°	0.82°	30.99°	-12.30°
CAL13	0.00°	0.87°	31.01°	-12.29°

Table 4.10: Attenuator values for phase-calibration

Name	Attenuation [dB]	Temperature [K]
L_A	0	2838
L_B	0.872	2376
L_C	2.997	1571
L_D	6.016	932
L_E	10.166	541
L_{DE}	16.182	357
L_{BCDE}	20.051	321
50Ω	∞	296

every configuration about 120 measurement with a correlation time of 500ms have been done. The results shown here have been obtained with the method described in [25], where in-phase and quadrature errors are retrieved simultaneously.

The different powers levels were obtained by placing different attenuators between the noise source and the input of the noise distribution network. The attenuation values and the corresponding power at the output of the noise distribution network are shown in table 4.10. All attenuators were measured precisely with a network analyser. In one case also a load at ambient temperature was connected to the noise distribution network, which is equivalent to have an infinite attenuation if the load is at the same temperature as the network.

Tables 4.11 and 4.12 show the mean value and the standard deviation of the in-phase error for the same measurements, respectively. The temperature column refers to total injected temperature to the receivers. The complete S-parameters matrix of the NDN should be known in order to calculate precisely the correlation temperature injected into the receivers. It can be observed that the mean value of the in-phase error is rather constant when relatively high power is injected into the receivers, but the standard deviation shows an increase in uncertainty in the in-phase error estimation when the injected power is decreased. Note that it is very high when no correlated noise is injected, that is, for the infinite attenuation case. This is in accordance with theory, as in that case no correlated noise is present, and thus, the estimation of the in-phase error is not possible.

In-phase error as a function of power

Table 4.11: In-phase error as a function of input power (mean value).

RX: Tin [K]	1	2	3	4
2838	0.00°	1.74°	30.25°	-17.20°
2376	0.00°	1.54°	30.47°	-16.83°
1571	0.00°	1.39°	30.57°	-16.81°
932	0.00°	1.34°	30.78°	-16.43°
541	0.00°	1.09°	31.37°	-15.90°
357	0.00°	0.34°	32.56°	-14.84°
321	0.00°	-0.46°	25.45°	-19.71°
296	0.00°	-4.55°	31.74°	-13.83°

Table 4.12: In-phase error standard deviation as a function of input power.

RX:	1	2	3	4
Tin [K]				
2838	0.00°	0.02°	0.02°	0.03°
2376	0.00°	0.02°	0.02°	0.02°
1571	0.00°	0.03°	0.03°	0.04°
932	0.00°	0.04°	0.04°	0.04°
541	0.00°	0.06°	0.07°	0.07°
357	0.00°	0.26°	0.23°	0.26°
321	0.00°	0.60°	0.57°	0.52°
296	0.00°	24.06°	21.55°	19.81°

Quadrature error as a function of power

As in-phase and quadrature errors have been retrieved simultaneously, the obtained quadrature error is also very noisy when few power is injected (see tables 4.13 and 4.14). The error in the in-phase error estimation is distributed between the in-phase error and the quadrature error. This would have not happened if the quadrature error would have been retrieved independently from the in-phase error, using the cross-correlations of the I and Q signals of the same receiver [26]. The standard deviation in the quadrature error is below 0.6° for all cases,except for infinite attenuation.

These results indicate that quadrature errors should be estimated independently from in-phase errors, as they can be obtained directly in measurement mode. In this way, quadrature error estimations are made independent from noise injection temperature. In fact, quadrature errors can be estimated individually for each single measurement. In-phase errors, show a high tolerance to noise injection power, as their standard deviation is only affected severely for very low power noise injections. Thus, the injected noise power will be limited by the dynamic range of the receivers.

Table 4.13: Quadrature error as a function of input power (mean value)

RX: Tin [K]	1	2	3	4
2838	2.39°	13.66°	8.91°	3.68°
2376	2.39°	13.65°	8.90°	3.67°
1571	2.38°	13.63°	8.90°	3.66°
932	2.38°	13.65°	8.90°	3.65°
541	2.38°	13.66°	8.90°	3.63°
357	2.45°	13.73°	8.89°	3.61°
321	2.40°	13.70°	8.81°	3.66°
296	6.21°	22.79°	13.65°	1.20°

Table 4.14: Quadrature error standard deviation as a function of input power

RX: Tin [K]	1	2	3	4
2838	0.02°	0.02°	0.02°	0.02°
2376	0.02°	0.02°	0.02°	0.02°
1571	0.02°	0.02°	0.02°	0.02°
932	0.03°	0.03°	0.03°	0.02°
541	0.06°	0.06°	0.05°	0.04°
357	0.23°	0.21°	0.18°	0.15°
321	0.53°	0.51°	0.47°	0.37°
296	36.86°	39.75°	38.00°	13.68°

4.2.6   PMS Calibration

The PMS response of the HUT-2D four element segment has also been measured for all eight channels ($4\times$ I/Q). The results of these measurements are presented as follows.

Warm & Cold Calibration

The PMS response of the HUT-2D receivers has been measured using the setup shown in figure 4.25. Two different input powers were injected through the port C of the receivers. The first input power was generated with a matched load at ambient temperature connected to the C-port. The second input power was generated connecting through a cable a matched load at the boiling temperature of liquid nitrogen (77K). The attenuation of the cable has been measured to be $L = 0.06$dB. The injected power can thus be computed with

$$T_{in} = \frac{T_{cold}}{L} + \frac{L-1}{L}T_0 \qquad (4.27)$$

The output power of the receivers was measured with a calibrated power meter. The PMS calibration curve was modelled with

$$P_{out} = k\left(T_R + T_{in}\right)B \qquad (4.28)$$

being $k = 1.38\times10^{-23}$ the Boltzman constant, T_R the receiver noise temperature and $B = 7.42$MHz the bandwidth of the receivers.
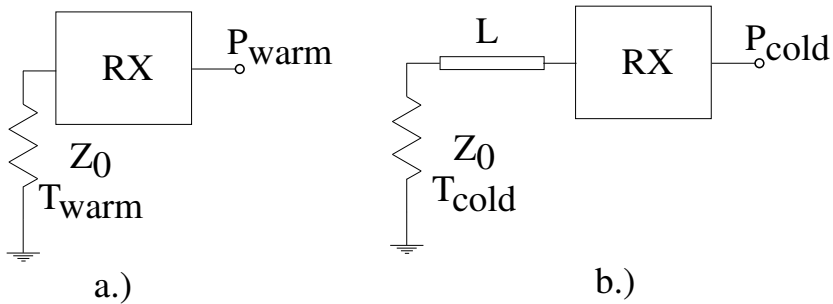

Figure 4.25: a.) *Warm* measurement setup. b.)*Cold* measurement setup.

Figure 4.26 shows the PMS response of receiver one for the I and Q channels. The measured receiver noise for all eight channels is between 283 K and 307 K depending on the channel. The receiver noise temperatures for the I and Q channels of a single receiver can vary as much as 11 K. The obtained gain in the measurements is between and 92.3dB and 94.6dB, which is well inside specification.
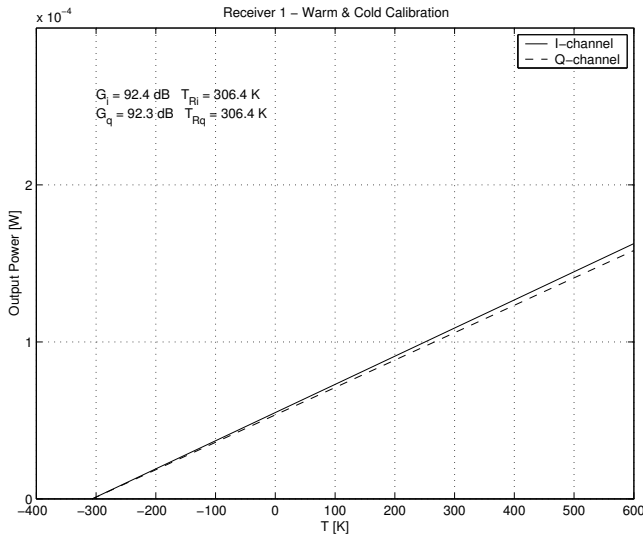

Figure 4.26: PMS responses of receiver 1, with warm & cold calibration.

4.3 Cold Correlated Noise Injection

The calibration of phase-errors consists of injecting correlated noise into the receivers and measuring the output correlation. Correlated noise is generated with a noise source, which gives equivalent hot noise. Injecting cold noise also gives correlated noise at the input of the receivers, but with less power than when using hot noise. This has been tested and positive results have been obtained.

4.3.1   Cooled Load Method

The cold noise injection has been done by connecting a matched load to the input of the NDN and cooling it down to 77K with liquid nitrogen. Another way to have an equivalent cold load is to connect an antenna to the input port of the NDN and point this antenna to the sky, in order to catch only the deep sky radiation. In this way the equivalent noise temperature at the input of the NDN is around 5K (Sky temperature).

The results when injecting cold noise generated with a cooled down load are presented first. The in-phase errors are shown in figure 4.27. About 200 calibration-measurements with a correlation time of 4000ms were done. The retrieved in-phase errors can be clearly distinguished. Their standard deviation is below 0.9 degrees for all four receivers. The results for the quadrature error are shown in figure 4.28. The standard deviation for the quadrature error retrieval is below 0.8 degrees for each receiver, a little bit better than for the in-phase errors. The results shown in the figures correspond to the results obtained using the calibration approach of [25].

Another measurement that has been done consisted in making calibrations while the load at the input of the receiver heated up slowly from 77 K to ambient temperature. Figure 4.29 shows the modulus of the phase-calibrated output correlation, while the amount of correlated noise at the input of the receiver decreases. The correlation time for the measurements was 4000ms. It can be clearly observed that when the difference between injected and physical temperatures $T_{ref} - T_{phy}$ approaches zero, so do the correlations, confirming Bosma's noise theory [31]. Equation (46) in chapter three of [26], which expresses Bosma's theory in a scalar way is repeated here

$$\mu_{ij}^C = \tilde{\mathbf{r}}_{ij}\left(0\right) e^{j(\phi_{i0}-\phi_{j0})}.$$

$$\cdot \frac{|S_{i0}||S_{j0}|\left(T_{ref}-T_{phy}\right)}{\sqrt{|S_{i0}|^2 T_{ref} + T_{phy}\left(1-|S_{i0}|^2\right)+T_{Ri}}\sqrt{|S_{j0}|^2 T_{ref} + T_{phy}\left(1-|S_{j0}|^2\right)+T_{Rj}}}$$

$$(4.29)$$

with ϕ_{i0} and ϕ_{j0} being the phase of the S-parameters of the NDN between port o and ports i and j, T_{ref} the noise temperature at the input of the NDN, T_{phy} the physical temperature of the NDN and T_{Ri} and T_{Rj} the equivalent noise temperatures input from the receiver into the NDN at ports i and j. This measurement shows the high sensitivity of the instrument.
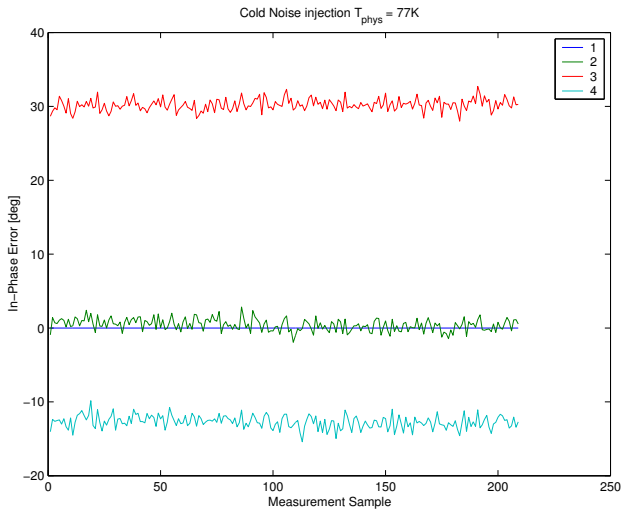
Figure 4.27: Retrieved in-phase error for cold noise injection.
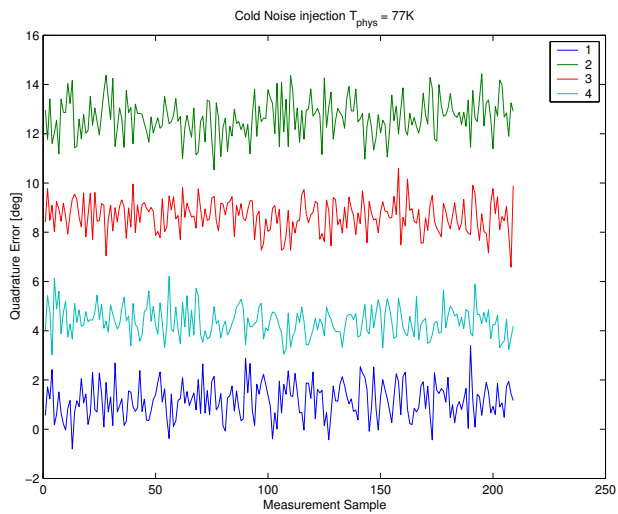

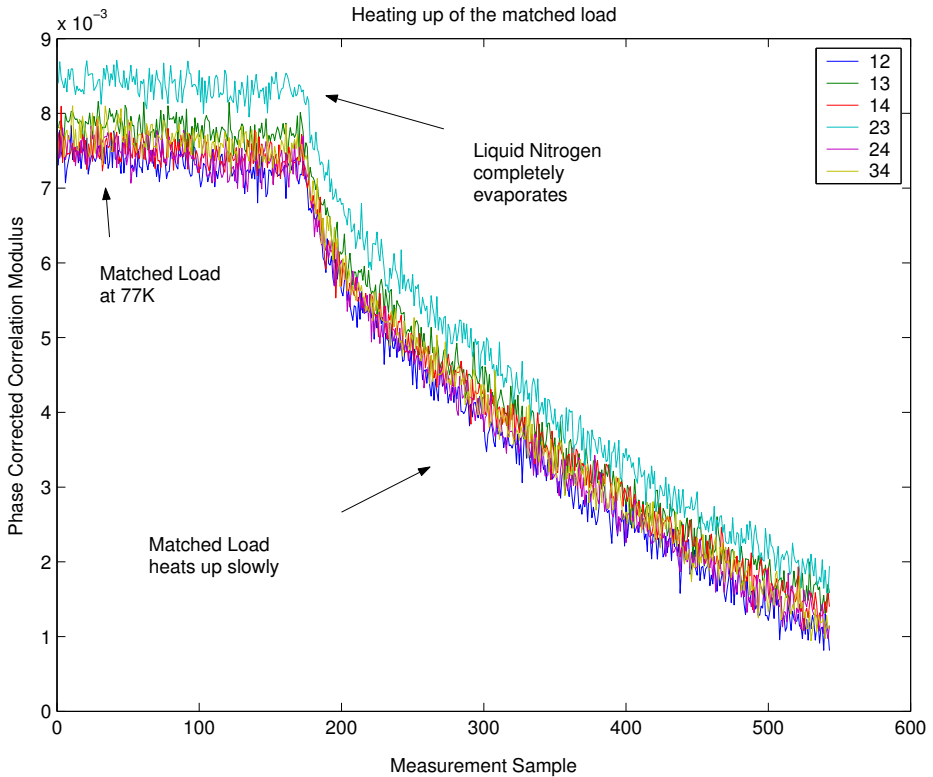Figure 4.28: Retrieved quadrature error for cold noise injection.

Figure 4.29: The correlation modulus decreases when the cold load at the input of the NDN heats up slowly.

4.3.2   Deep Sky Noise Injection

In order to improve the phase calibration with cold noise a method for injecting much colder noise into the input of the receivers has been setup. It consists in connecting the input port of the NDN to a horn antenna which is pointing to the sky. The equivalent temperature of the sky is around 2.7 K, if only cosmic noise is measured. Main lobe efficiency and the effect of surrounding buildings, the Sun, the clouds and other uncontrolled aspects may increase the equivalent antenna temperature. Figures 4.30 and 4.31 show the results that have been

obtained for the phase-calibration using this method. The quadrature error is
rather stable, but not the in-phase error. This can be due to many factors. The
first one being possible interference caught by the antenna. This interference
shows up in the measured correlations and has an effect on the computation
of the in-phase errors. Another effect can be the non ideal matching of the
antenna. This has an effect on the phase of the correlation at the input of the
receivers as can be seen from equation (B.6) in appendix B. From this results it
is clear that the use of an antenna to generate cold noise for phase-calibration
of HUT-2D is not a reliable method. Maybe for a space-borne interferometer
like MIRAS this solution would be feasible as its environment might be better
controlled being the instrument in space. In any case it seams a less reliable
method than injecting noise conventionally as it depends on an uncontrollable
environment. A solution for injecting cold noise in a space-borne instrument
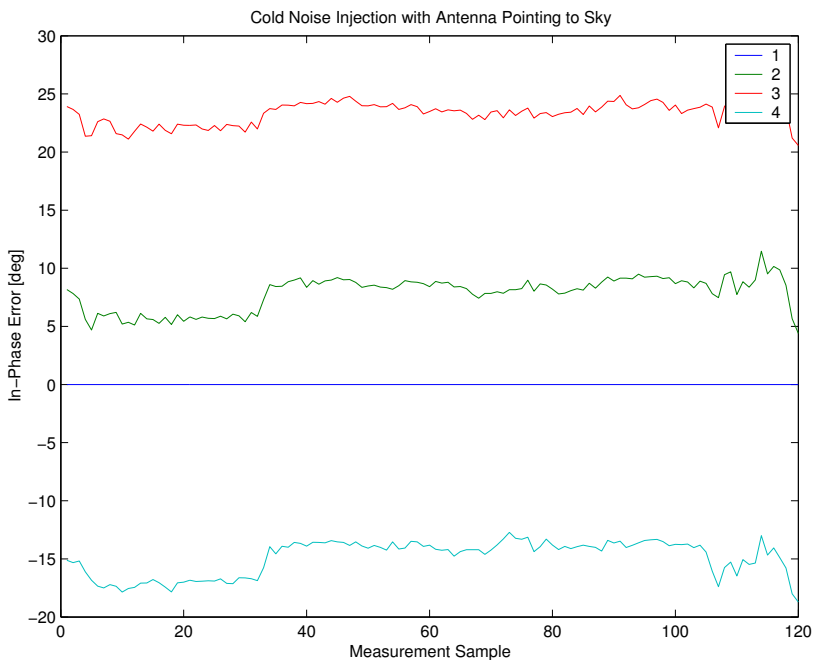

Figure 4.30: Retrieved in-phase error for cold sky noise injection.

would be to have a matched load attached to a heat-sink at the cold side of the satellite, in order to cool it down much below the physical temperature of the NDN.
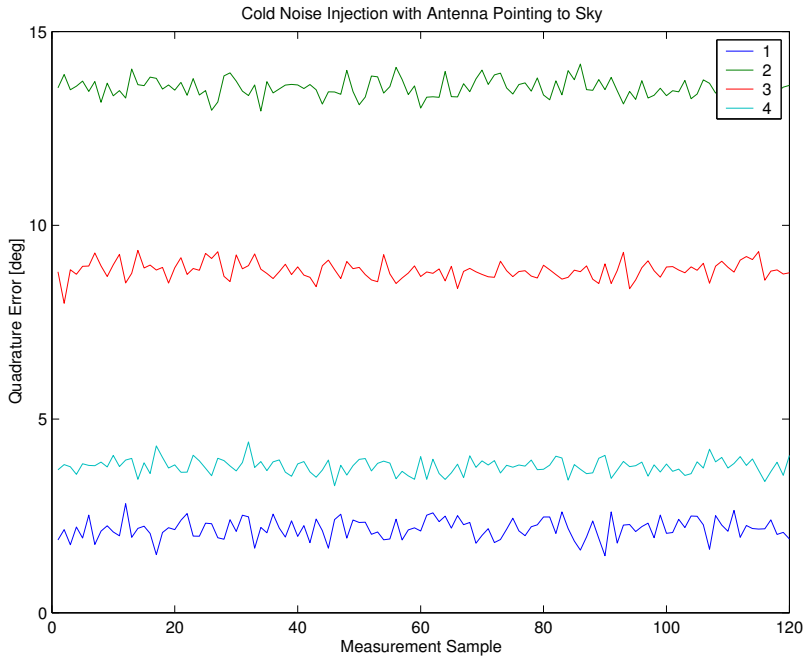

Figure 4.31: Retrieved quadrature error for cold sky noise injection.

4.4 Effect of a Receiver Failure on the Calibration

During calibrated noise injection one single noise source is injecting noise to a group of several receivers, through a passive power dividing network known as Noise Distribution Network (NDN). The value in amplitude and phase of the injected noise depends of

- Equivalent noise temperature of the noise source

- S-parameters of the NDN

- Physical temperature of the NDN

- Equivalent noise temperature injected by the receivers into the NDN

- Matching of all devices connected to the input/output ports of the NDN

as it is shown in [31] and reviewed in appendix B. A receiver failure could have as a consequence that its matching to the NDN suffers an important change. After failure it could present an open or short circuit to the NDN. This could happen, for instance, if the polswitch at the input of the receivers gets damaged.

In order to study this effect the setup shown in figure 4.32 has been used. Figure 4.33 shows the schematics of the setup.   Correlated noise is injected into a HUT-2D four receiver segment, through the NDN. In fact, only three receivers of the four available are used. Instead of the fourth receiver, a phase shifter ended with an open circuit is connected to the NDN. This simulates the
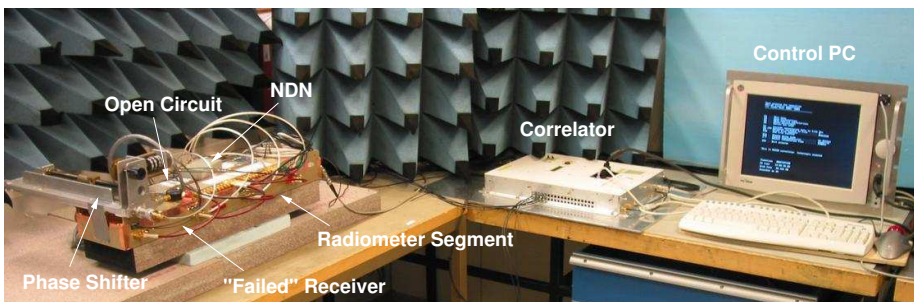
Receiver failure experiment

Figure 4.32: Experiment setup for measuring the effect of a receiver failure.
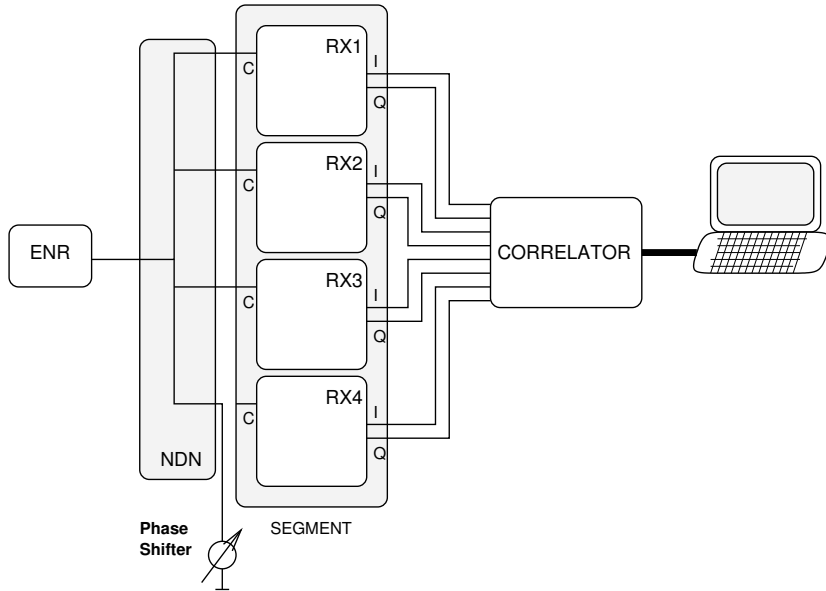
Figure 4.33: Experiment schematics for measuring the effect of a receiver failure.

failure in a controlled manner. The phase of the open circuit can be adjusted with the phase shifter.

The experiment consisted in calibrating the in-phase errors of the three *working* receivers with [26], for an extended set of phases of the simulated short circuit. In fact, during the experiment an open circuit was used instead of a short circuit, but this makes no difference, as only a 180° phase shift, which can be compensated by the phase shifter, differentiates them both. The phase of the simulated short circuit has covered the complete range of 360° in steps of 10° (from 50° to 410°). The retrieved phase errors are shown in figure 4.34 with red crosses. In fact, the figure shows the excursion of the phase errors, as its mean values has been subtracted. It can be noticed, that there is a clear dependence of the phase of the short circuit connected to the NDN.

The phase of the correlation at the input of the receivers has been computed using equation (B.7). Therefore it was necessary to measure the S-parameters of the NDN, the matching of the connected devices to the input/output ports, the physical temperature of the NDN and the equivalent injected temperature of the
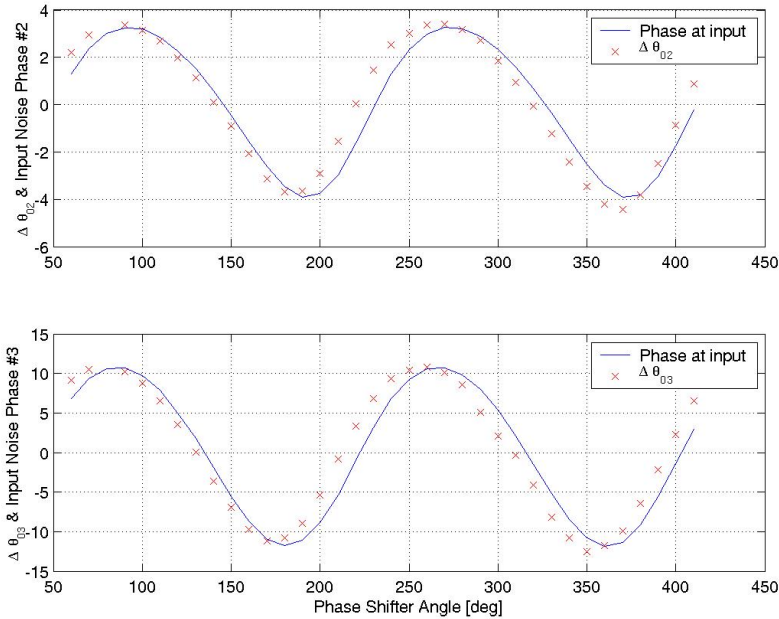
Figure 4.34: Experimental and predicted change of the phase errors due to receiver failure (Receivers 2 & 3).

noise source. The equivalent noise temperature of the receivers was assumed to be equal to the physical temperature of the NDN. The predicted phase excursion of the correlations at the output of the NDN before entering the receivers are also shown in figure 4.34 with a blue line. It can be observed that the calibration phase and predicted noise injection phase follow each other almost perfectly. Looking carefully at the results one can appreciate that predicted and measured phases are shifted $10°$ respect to each other, exactly the separation between measurements, which indicates that there has been a confusion when saving the experiment data.

This experiment demonstrates that Bosma's noise theory [31] may be used with confidence for calibration purposes of MIRAS. It also shows that the in-

phase error calibration procedure is very precise because predicted and measured excursions follow each other. The third result is that it shows that a receiver failure may have effects in the in-phase error estimation of all receivers connected to the same noise source. Notice that the phase excursions are very high, 7° and 23° for receivers two and three respectively, showing the potential importance of receiver failure on the calibration of the receivers. It has to be noted that the isolation between output ports of the used NDN was rather bad (≈ 18dB) compared to the transmission value from the input port to any output (≈ 23dB). With better isolation between output ports the effect of a receiver failure is minimised. This can be deduced developing (B.7). These experimental results confirm the simulations of [38].

4.5 SAM Calibration

In this section preliminary results on the four-point two-level baseline calibration are presented [35, 36, 37]. These measurements were done using the MIRAS Demonstrator Pilot Project 3 (MDPP-3) hardware of ESA, during its manufacturing and test phase. This project consists in the development of an airborne MIRAS prototype, known as SAM (Small Airborne MIRAS). Therefor previously manufactured hardware has been modified in order to be capable of implementing the two level noise injection calibration method, as it is the case with the LICEF-2 receivers, or the DICOS-2 correlator. In the case of the LICEF-2 receivers the attenuator at the IF stage has been implemented by changing the gain of the mixer by switching its power supply between two different voltages. The modifications of DICOS-2 consisted in changing the control of the polswitch signals, in order to be able to put the polswitch of all receivers to C or U position during calibration.

SAM EGSE description   The Electrical Ground Support Equipment (EGSE) has been designed and manufactured at IEEC for ESA, under subcontract with EADS-CASA *División Espacio*[5], who manufactures the antenna array itself. The aircraft that will fly this prototype is the Skyvan of the Laboratory of Space Technology of the Helsinki University of Technology. It consists of a power supply box, known as *Boltzmann*, a control electronic box, know as *Kelvin*, and a GPS receiver to timestamp all measurements. The control block has been implemented with an FPGA. This part makes the low level control of SAM. Figure 4.35 shows the block diagram of control part of the designed and manufactured EGSE. Also

---

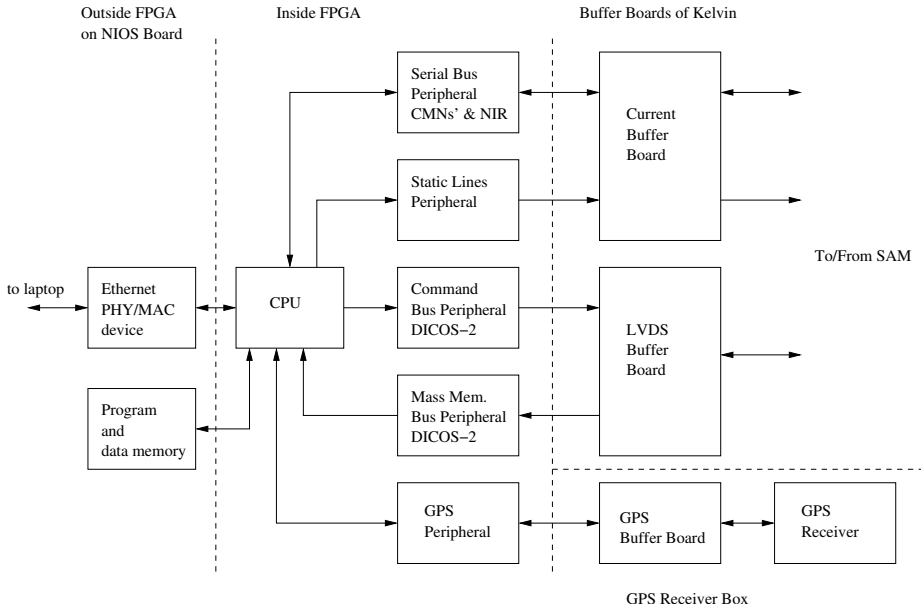[5]Space Division of EADS-CASA company.

Figure 4.35: Diagram of the control block of the EGSE of SAM.

auxiliary electronic boards have been designed. A laptop is used as the man-machine interface to send commands to the EGSE and to store the collected data. Figure 4.36 shows the manufactured EGSE of SAM. More information about the EGSE can be found in [45, 46].

The two-level calibration method test and data processing have been performed with the support of the UPC remote sensing group. The setup consisted of two LICEF receivers forming a baseline, the modified DICOS-2 correlator, the SAM EGSE and the CAS shown in figure 4.37. Correlated noise of two different power levels could be injected to the LICEFs using the attenuated and the non-attenuated paths of the NDN. The gain of the LICEFs could also be switched between two values, by activating the equivalent attenuator at the IF stage of the receivers. All these options were selectable directly from the EGSE. The LICEFs were distinguished from each other by a coloured sticker (*green* and *white*) at its radome.

The four PMS measurements described in section 3.3 were done. Two for hot noise injection (with and without attenuator) and two for warm noise in-

Four point amplitude calibration

Figure 4.36: EGSE of the Small Airborne MIRAS (SAM).
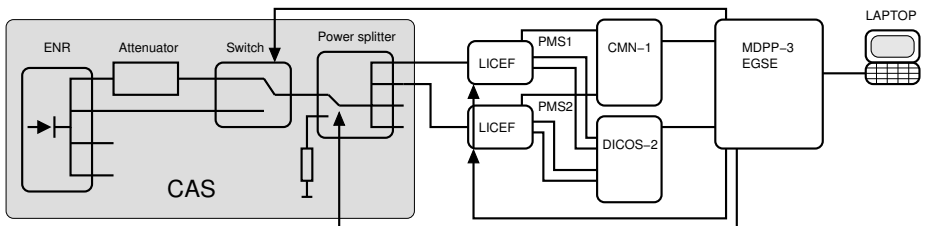
Figure 4.37: Setup for the four point calibration experiment.

jection, (also with and without attenuator). The hot and warm injected powers into the LICEFs were measured with a noise figure meter before starting the experiment. The injected temperatures are shown in table 4.15. The PMS voltage measurements for both receivers are given in figure 4.38. The four points measurement sequence can be clearly appreciated. It can be clearly observed

Table 4.15: Warm and hot temperatures injected into the LICEF during the four points PMS calibration

	Receiver 1 (green)	Receiver 2 (white)
HOT	1851K	1764K
WARM	355K	358K

Figure 4.38: PMS voltages of the four points measurement.

Figure 4.39: Ones and zeros unbalance in correlation units.
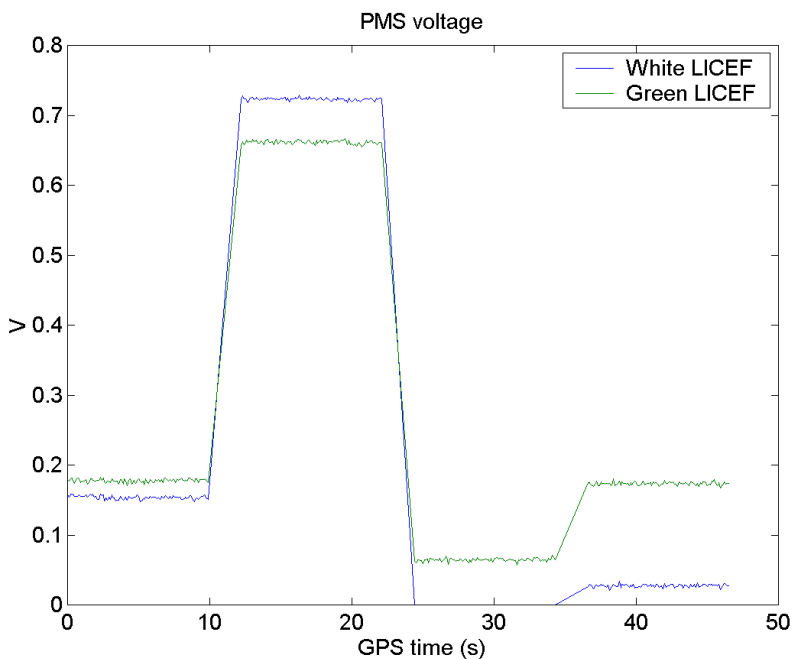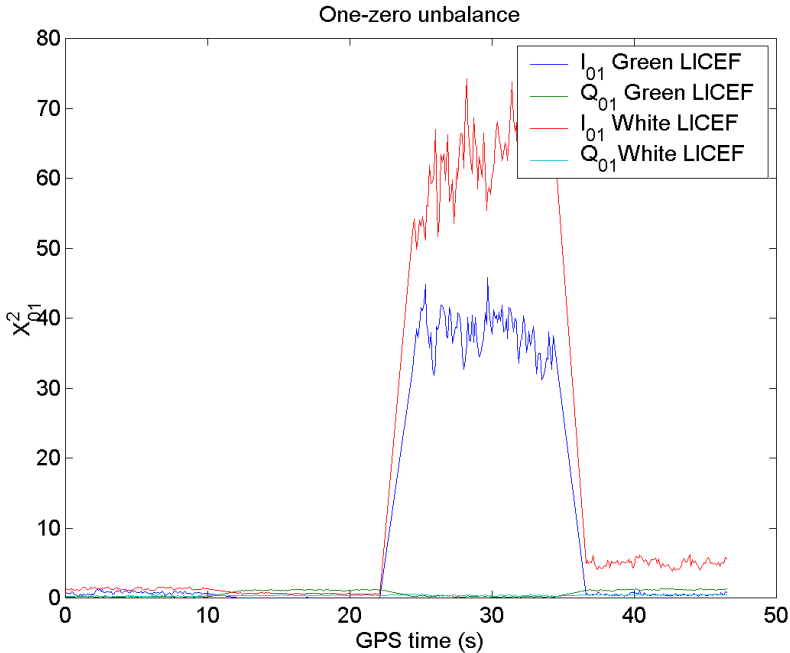
that the PMS voltage when the attenuator is on (steps three and four), is much lower for the *white* receiver than for the *green* receiver. This indicates a much higher attenuation value for receiver two than for receiver one.

<div style="float:left; font-weight:bold; font-size:small">A/D offset correction</div>

    The calibration procedure has been tested with this measurements. The correlation measurements were 100ms long. As a first step the one-zero unbalance due to the A/D offset has been measured. It can be seen in figure 4.39. The correlation results are given in correlation units ($1\mathrm{cu} = 1 \times 10^{-4}$). As expected, the lower the input power, the higher is the unbalance from equation (3.58). This is especially the case for the white LICEF during the warm noise injection with internal attenuation.

<div style="float:left; font-weight:bold; font-size:small">Quadrature error correction</div>

    The quadrature error has also been retrieved from cross-correlation between the in-phase and quadrature signal of the same receiver using equation (3.7) (see figure 4.40). This measurement reveals the known *problem* of LICEF-2
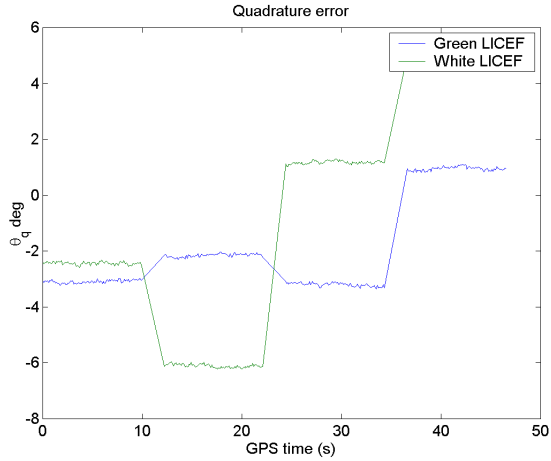
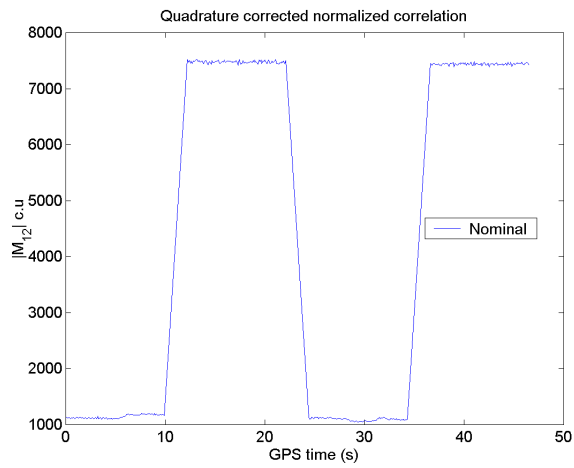Figure 4.40: Quadrature error for both LICEF-2 receivers.

Figure 4.41: Amplitude of the quadrature corrected correlation $|M_{ij}|$.
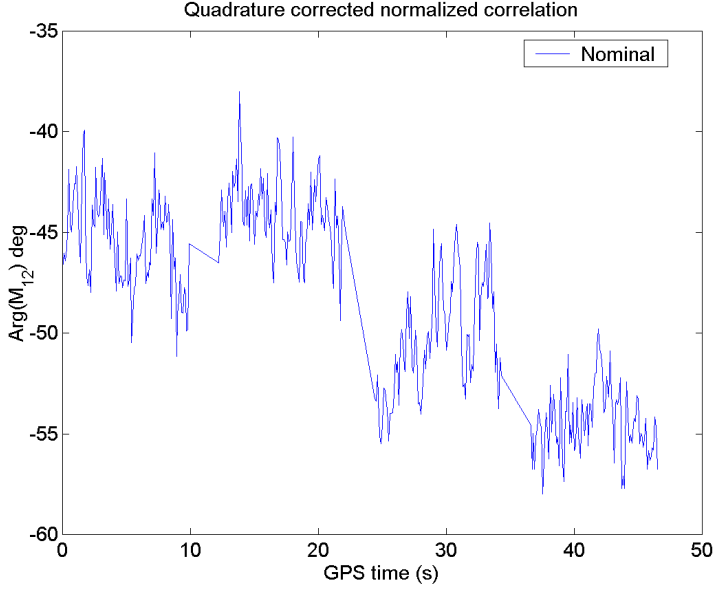
Figure 4.42: Phase of the quadrature corrected correlation $arg(M_{kj})$.

receivers, where the quadrature error is dependent on the input power due to the characteristics of the mixer inside the LICEFs. These results strengthen the importance of equation (3.7), where the quadrature error is calibrated individually for each measurement independently of the calibration or observation mode.

The amplitude of the quadrature corrected normalised correlation is shown in figure 4.41. Two distinct amplitudes can be observed, corresponding to the two injected power levels. Its phase is presented in figure 4.42. An important phase jitter can be observed. This problem is intrinsic to the LICEF-2 receivers and was already observed in previous measurements with this equipment [34].

The amplitude of the fringe-washing term G_{ij}^C, obtained from equation (3.51), is shown in figure 4.43. As the NDN S-parameters had not been measured, it has been assumed in (3.51), that $S_{i0} = S_{j0} = 1$. The measurements for the phase of G_{ij}^C are given in figure 4.44.

Receiver stability Measurements aimed at measuring the stability of the receivers were also
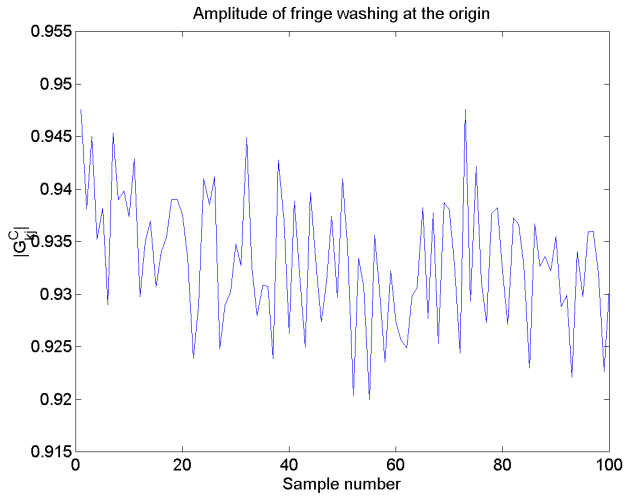
Figure 4.43: Amplitude of the fringe-washing term $|G_{ij}^C|$.
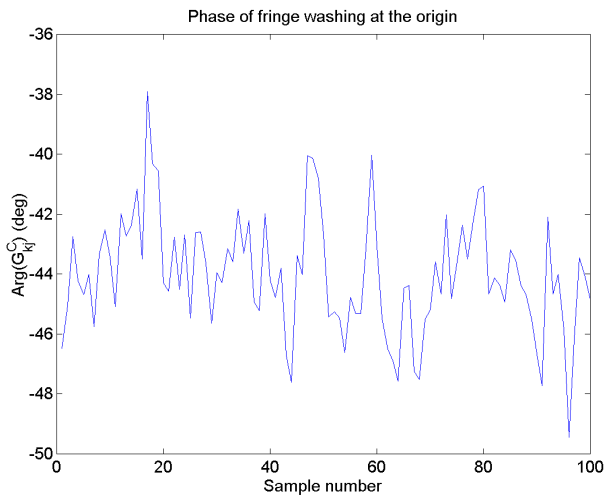
Figure 4.44: Phase of the fringe-washing term $arg(G_{ij}^C)$.

done. Correlated noise was injected into both LICEF receivers during one hour. Figures 4.45 and 4.46 show the amplitude and phase of the quadrature corrected correlations M_{ij}. The variation in amplitude of the mean value is only about 30cu over 7400cu, which corresponds to a variation of 0.4%. The phase of the quadrature corrected correlations does also show the phase jitter of the receivers, superimposed to a soft drift of $10°$, which shows a more stable behaviour to the end of the test.

Finally, the shape of the fringe-washing function has also been measured using the three delay method [41, 42], which has been shown in section 4.1.5. The amplitude is presented in figure 4.47, while the phase can be observed in figure 4.48.

Equation (3.36) has been used to obtain the voltage offset V_{off_i}. The gain G_{ij} has been obtained from (3.51), assuming that $S_{i0} = S_{j0}$, while the receiver
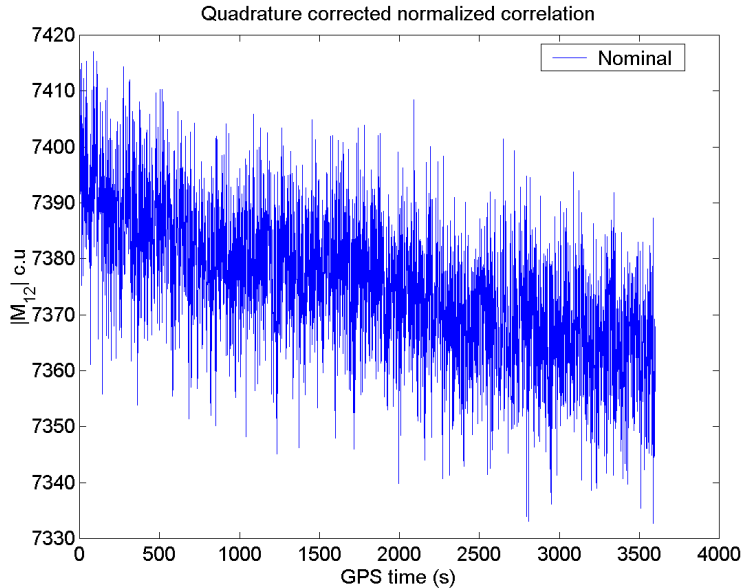
Figure 4.45: Amplitude stability of the quadrature corrected correlations $|M_{kj}|$.
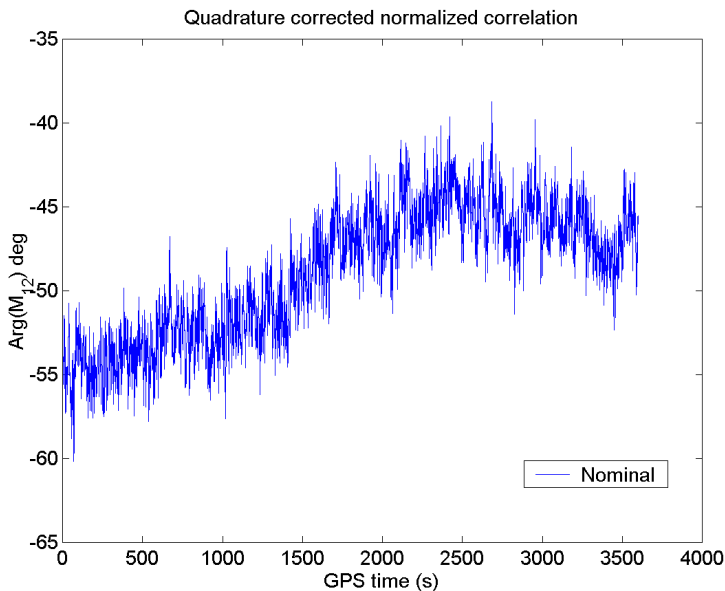
Figure 4.46: Phase stability of the quadrature corrected correlations $arg(M_{kj})$.

noise temperature has been estimated with

$$T_{R_i} = \frac{(V_{2_i} - V_{4_i})\,T_{C1_i} - (V_{1_i} - V_{3_i})\,T_{C2_i}}{(V_{1_i} - V_{3_i}) - (V_{2_i} - V_{4_i})} \qquad (4.30)$$

as the injected temperatures T_{C1_i} and T_{C2_i} have been measured with the noise figure meter. The results are shown in table 4.16. Gain and voltage offsets and attenuations are realistic values. Although attenuation for receiver two is much higher than expected it does fully agree with the PMS measurements. Receiver noise temperature is too low for both receivers, especially for receiver two. The measurements seem to indicate that some saturation effect is present at the lower side of the PMS scale and that the receivers will have to be overhauled.

These preliminary tests have shown that the measurement and data acquisition subroutines developed to control SAM perform as expected. Storage and data formats are also compatible to the data processing subroutines. Extensive functionality test, based on the hardware and calibration subroutines presented
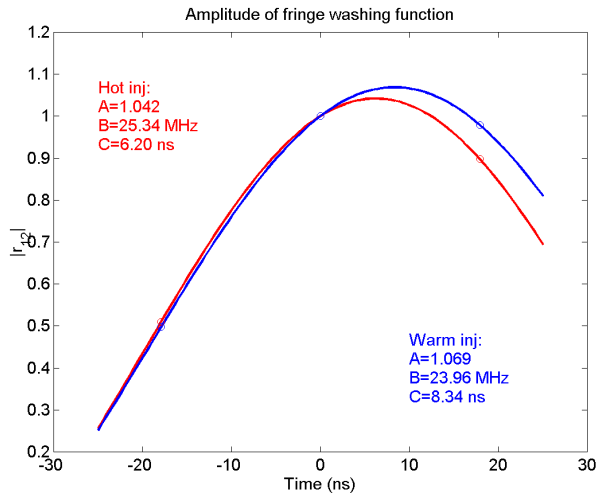
Figure 4.47: Amplitude measurement of the fringe-washing function.
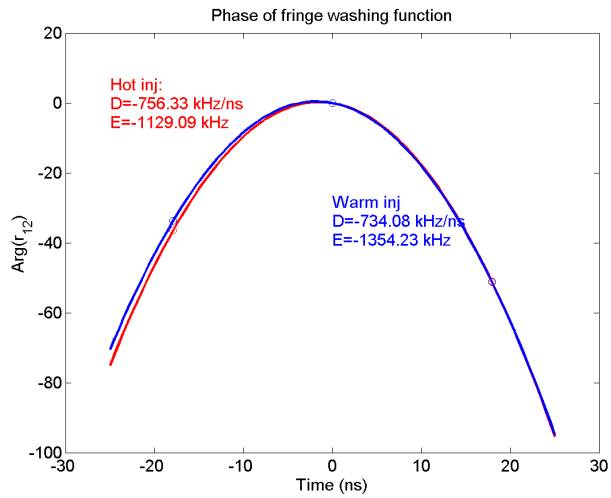
Figure 4.48: Phase measurement of the fringe-washing function.

Table 4.16: Four points PMS calibration results

	Receiver 1 (green)	Receiver 2 (white)
V_{off}	31.7mV	-7.8mV
G	0.323mV/K	0.404mV/K
T_R	97.6K	39.9K
$L^\dagger$	4.414	20.64

† The attenuation is given in linear scale.

so far, are now foreseen in the frame of the MDPP-3 project, at EADS-CASA laboratories, to take into account all baselines of SAM in order to perform the last hardware tuning, prior to start with the airborne experimental campaign.

Chapter 5

Polarimetric Mode of MIRAS

The fully polarimetric mode of a broad field of view 2D-interferometer has been formulated. It consists in measuring the cross-correlation of antenna pairs which have different polarisation vectors. In the dual-polarisation mode the cross-correlations between two equally polarised antennas are measured; one time for both antennas in H-polarisation and another time for both antennas V-polarisation; in that way two modified brightness temperature maps of the scene are obtained, HH and VV. In the fully polarimetric mode also the cross-correlation between differently polarised antennas is measured, obtaining from each scene four temperature maps: HH, VV, HV, VH. This has been explained comprehensively in [19, 20].

In this document the polarimetric Visibility function is expressed as

$$\mathbf{V}_{ij}^{pq}(u,v) = \frac{k_B B \alpha^2}{2\pi} \cdot$$
$$\iint_{\xi^2+\eta^2 \leq 1} G(\xi,\eta) \frac{T_B^{pq}(\xi,\eta)}{\sqrt{1-\xi^2-\eta^2}} \tilde{\mathbf{r}}_{\mathbf{h}}(-\frac{u\xi+v\eta}{f_0}) e^{-j2\pi(u\xi+v\eta)} \mathrm{d}\xi \mathrm{d}\eta \qquad (5.1)$$

where i,j refer to the receiver number, p,q to its polarisation status (vertical or horizontal), $G(\xi,\eta)$ is the antenna pattern gain, T_B^{pq} the modified brightness temperature for a specific receiver antenna polarisation, $\tilde{\mathbf{r}}_{\mathbf{h}}$ is the fringe-washing

function and

$$u = (x_j - x_i)/\lambda_0 \tag{5.2}$$
$$v = (y_j - y_i)/\lambda_0 \tag{5.3}$$

with (x,y) describing the position of the antenna elements in array. The modified temperature T_B^{pq} cannot be seen as a real brightness temperature when the polarisation for both antennas are different (hv or vh). It is only a way to use the same notation for hh, vv, hv, vh correlations, expressing their cross-correlation.

5.1 Pixel to Antenna Frame Conversion

When observing a scene from an antenna, the (h,v) polarisations of the antenna will not match the (H,V) polarisations of the patch on ground. The (H,V) ground-polarisation signals will get mixed at the antenna (h,v) polarisation. Correlating the antenna signals (h,v) will lead to a mixture of the modified brightness temperatures also.

Let $\mathbf{e^V}$ and $\mathbf{e^H}$ be the differential fields components radiated by a pixel in V and H polarisations. They generate the total field

$$\vec{E} = \mathbf{e^V}\hat{V} + \mathbf{e^H}\hat{H} \tag{5.4}$$

It has to be noted that all the parameters on this equation depend on the observed direction, but this has been omitted for simplicity. The vertical and horizontal components of the electric field in the polarisation of the antenna can be expressed by

$$\mathbf{E^v} = \hat{v} \cdot (\mathbf{e^V}\hat{V} + \mathbf{e^H}\hat{H}) \tag{5.5}$$
$$\mathbf{E^h} = \hat{h} \cdot (\mathbf{e^V}\hat{V} + \mathbf{e^H}\hat{H}) \tag{5.6}$$

where $\hat{v}$ and $\hat{h}$ are the unity effective lengths vector of the v and h polarisation of the antennas for a given direction

$$\hat{v} = \sin(\phi + m\pi)\hat{\theta} + \cos(\phi + m\pi)\hat{\Phi} \tag{5.7}$$
$$\hat{h} = -\cos(\phi + m\pi)\hat{\theta} + \sin(\phi + m\pi)\hat{\Phi} \tag{5.8}$$

following Ludwig's third definition [21]. It has to be noted from the above expressions that the unity effective length vectors $\hat{v}$ and $\hat{h}$ are expressed as a rotation by an angle ϕ of the frame determined by $\hat{\theta}$ and $\hat{\Phi}$.

Equations (5.5) and (5.6) can be written in matrix notation

$$\left(\begin{array}{c} \mathbf{E^h} \\ \mathbf{E^v} \end{array} \right) = \left[\begin{array}{cc} A & B \\ C & D \end{array} \right] \left(\begin{array}{c} \mathbf{E^H} \\ \mathbf{E^V} \end{array} \right) \tag{5.9}$$

with

$$A = \hat{h} \cdot \hat{H} \tag{5.10}$$

$$B = \hat{h} \cdot \hat{V} \tag{5.11}$$

$$C = \hat{v} \cdot \hat{H} \tag{5.12}$$

$$D = \hat{v} \cdot \hat{V} \tag{5.13}$$

The polarisation frame of the incident radiation coming from the Earth $(\hat{H}, \hat{V})$ can also be expressed as a rotation of the reference frame $(\hat{\theta}, \hat{\phi})$. In this case the rotation angle is defined as Φ. If Faraday rotation is present the polarisation axes suffer an additional rotation $\Delta\Phi$. The polarisation of the wave originated on the ground can be written as

$$\hat{V} = \sin(\Phi + \Delta\Phi + n\pi)\hat{\theta} + \cos(\Phi + \Delta\Phi + n\pi)\hat{\Phi} \tag{5.14}$$

$$\hat{H} = -\cos(\Phi + \Delta\Phi + n\pi)\hat{\theta} + \sin(\Phi + \Delta\Phi + n\pi)\hat{\Phi} \tag{5.15}$$

If the parameters of equations (5.10) to (5.13) are computed following result is obtained

$$A = D = \cos(\Phi + \Delta\Phi - \phi + l\pi) \tag{5.16}$$

$$B = -C = -\sin(\Phi + \Delta\Phi - \phi + l\pi) \tag{5.17}$$

Computing the correlation of the antenna polarisation hh, hv, vh and vv yields.

$$\left[\begin{array}{c} T_B^{hh}(\xi,\eta) \\ T_B^{hv}(\xi,\eta) \\ T_B^{vh}(\xi,\eta) \\ T_B^{vv}(\xi,\eta) \end{array} \right] = \left[\begin{array}{cccc} A^2 & AB & AB & B^2 \\ -AB & A^2 & -B^2 & AB \\ -AB & -B^2 & A^2 & AB \\ B^2 & -AB & -AB & A^2 \end{array} \right] \left[\begin{array}{c} T_B^{HH}(\xi,\eta) \\ T_B^{HV}(\xi,\eta) \\ T_B^{VH}(\xi,\eta) \\ T_B^{VV}(\xi,\eta) \end{array} \right] \tag{5.18}$$

The brightness temperatures on the left correspond to the antenna frame, the ones on the right to the brightness temperatures of the source frame. The transformation can be expressed as

Invertibility with full-pol mode v.s. dual mode

$$[M(\xi,\eta)] = \left[\begin{array}{cccc} A^2 & AB & AB & B^2 \\ -AB & A^2 & -B^2 & AB \\ -AB & -B^2 & A^2 & AB \\ B^2 & -AB & -AB & A^2 \end{array} \right] = \left[\begin{array}{c} \mathbf{m^1} \\ \mathbf{m^2} \\ \mathbf{m^3} \\ \mathbf{m^4} \end{array} \right] \tag{5.19}$$

where $\mathbf{m^1}$, $\mathbf{m^2}$, $\mathbf{m^3}$ and $\mathbf{m^4}$ are the row vectors which form $[M]$. It can be easily seen that the transform matrix $[M]$ is invertible as its inverse is itself transposed

$$\det [M] = 1 \tag{5.20}$$

$$[M] [M]^\top = [I] \tag{5.21}$$

If only the vv and hh polarisations for a dual polarimetric mode are measured and the cross-correlations HV and VH on ground are negligible it can be seen [19] that the system

$$\left(\begin{array}{c} T_B^{hh} \\ T_B^{vv} \end{array} \right) = \left[\begin{array}{cc} A^2 & B^2 \\ B^2 & A^2 \end{array} \right] \left(\begin{array}{c} T_B^{HH} \\ T_B^{VV} \end{array} \right) \tag{5.22}$$

is non invertible for some directions in space. From that point of view the fully polarimetric mode is better than the dual polarimetric mode.

5.2 Full Polarimetry with a Dual Channel Interferometer

Implementation of the full-pol mode

In a dual channel interferometric radiometer each receiver consist of two identical channels to measure the h and v polarised signals, as can be seen in figure 5.1. In a single channel interferometric radiometer like MIRAS the h and v signals can be selected through a switch, but only one can be measured at the same time. Because of this reason it is also impossible to measure all four needed cor-

Switching sequence

relations hh, hv, vh and vv between two receivers at the same instant. It can be shown that with a sequence of 4 steps all four correlations can be measured for an interferometer consisting of 2 receivers. Figure 5.2 shows the switching sequence for a single baseline. In that case as each receiver has two possible positions (h,v) and there are two receivers the total number of combinations is four and thus, four steps are needed. This can be extrapolated to an array of more receivers [47].

This switching scheme is valid if the observed scene does not change during the whole switching sequence. This is not the case for MIRAS, as it is moving along its orbit and thus, the observed part of the Earth changes with each new snapshot. This has been studied for the case of the MIRAS baseline.
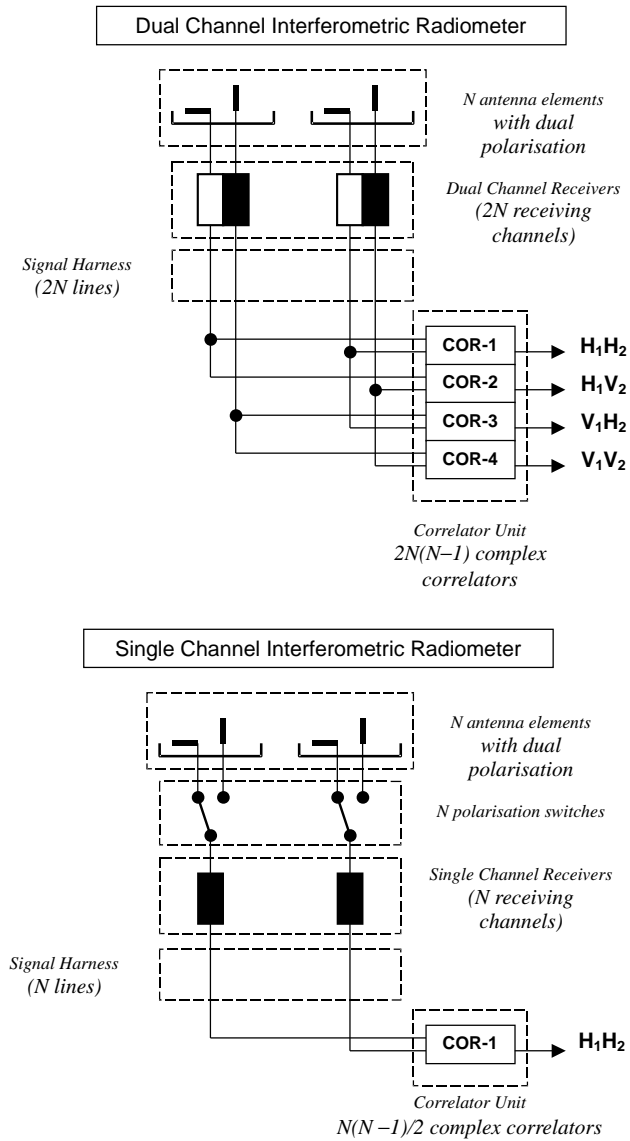
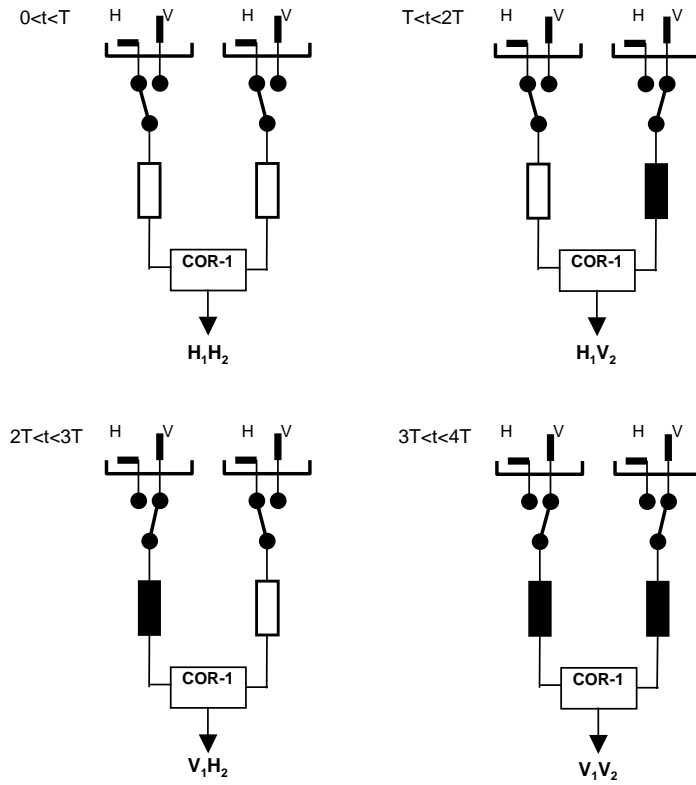Figure 5.1: Dual and single channel configurations for interferometric radiometers.

Figure 5.2: Switching sequence in polarimetric interferometric radiometer of two elements, using T as correlator integration time.

5.3 Full Polarisation Radiometry with Single Channel Receivers

The 4-step sequence shown in Figure 5.3 is used to generate the four baseline sets hh, hv, vh and vv, from which the polarimetric brightness temperature matrix is derived.

During Step-1 of the switching sequence the complete set of vv–baselines is obtained, as all receivers are connected to their v–probe (see Figure 5.5). Of concern in this case is the minimum integration time to avoid blurring due to the movement of the satellite along the orbit. A blurring of the system impulse response can be appreciated if the integration time is too long. A simulation has been carried out to show such a blurring effect for a nadir-pointed MIRAS flying at 755 km altitude when the integration time is $\tau = 3.6$ s, as an example. A point source has been simulated at bore sight with the satellite speed heading along the η direction cosine axis. Being the angular resolution of the sensor some 2° and the ground speed 7 km/s, the sub-satellite points moves 25 km over the integration time, that is, as much as the spatial resolution itself. This causes the main lobe to suffer distortion, stretching in the same direction as the velocity vector, as is presented on Figure 5.4(a). The same happens to the secondary lobes. Motion blurring

The elemental integration time of SMOS is $\tau = 1.2$ s and has been chosen to avoid the blurring just described. Figure 5.4(b) presents the result of the same scenario as Figure 5.4(a) but this time for the SMOS integration time of $\tau = 1.2$ s. It can be appreciated that the blurring diminishes considerably when reducing the integration time, to the point of making the distortion of the synthesised beam negligible.

Figure 5.6 shows Steps 2, 3 and 4 of the polarimetric switching sequence. At each one of the steps, just one third of the baselines of the hh, hv and vh–visibility stars are generated obtaining after the three steps three complete baseline sets. Looking in detail into Figure 5.6, it can also be seen that in a single step some of the baselines are measured for different polarisation combinations, for example hv and vh. This is due to the three redundant receivers placed along each inner arm extensions, in the central part of the array. This redundant receivers help not only to achieve polarimetric operation, but also to introduce redundancy in the baseline measurements.

The switching through Steps 2, 3 and 4 has to happen altogether in one single integration period $\tau = 1.2$ s, in order to fulfill the same blurring criterion as for Step 1. As a first approach, each step is given one third of the integration Main beam distortion
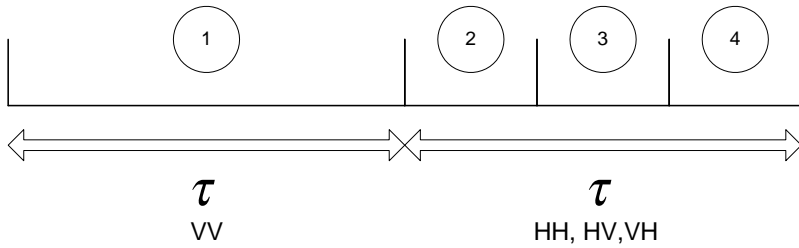
(a) Without interlacing of combined polarimetric measurements.
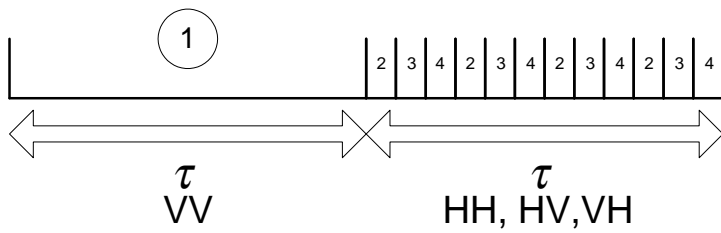
(b) With interlacing.
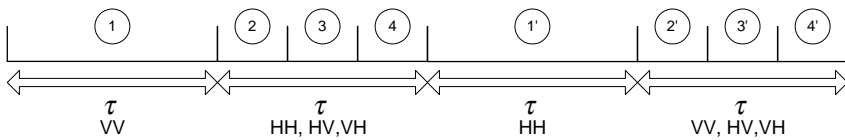
(c) Alternating polarisation concept to achieve equi-sensitivity.

Figure 5.3: MIRAS polarimetric mode switching sequences.
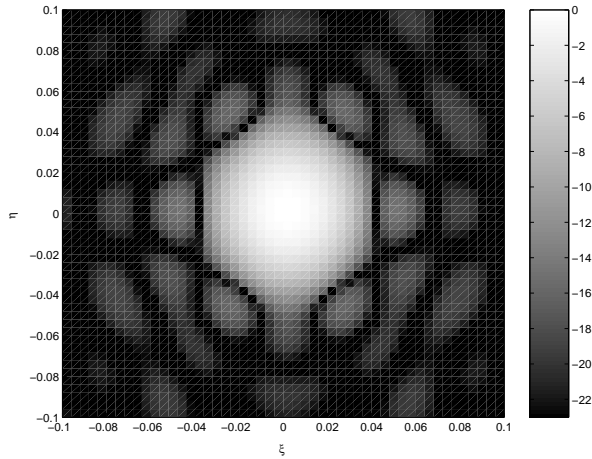
(a) Integration time = 3.6 s.
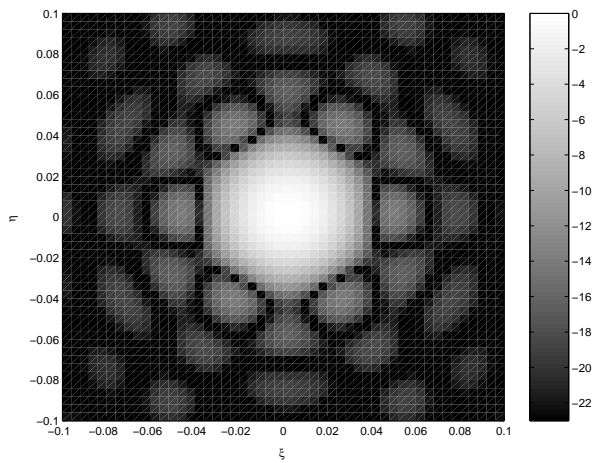
(b) SMOS integration time = 1.2 s.

Figure 5.4: Blurring of the T_{vv} impulse response due to satellite motion (along η).

time, i.e. $\tau/3 = 0.4$ s, as depicted in Figure 5.3(a). However a second distortion effect of the synthesised beam has to be taken into account for the images produced during Steps 2 through 4 as explained next. Let us take the case of T_{hh} as an example. The necessary baselines are acquired during the three steps 2, 3 and 4, while the observed scene changes from one step to the next due to the satellite motion relative to ground. Consequently the baselines acquired in different steps correspond to visibility samples of different images. When joining them together to generate a map of brightness temperature, the resulting image is distorted.

To illustrate such distortion in the images generated from Steps 2 through 4 of the polarisation sequence following the scheme in Figure 5.3(a), the same simulation scenario as for Step 1 has been run. The integration time corresponding to each step is 0.4 s. Figure 5.7(a) is the reconstructed T_{hh} image showing a distorted synthesised beam and secondary lobe pattern. The distortion is due to the fact that there is an inconsistency in the measured baselines.

Interlacing   In order to reduce this baseline inconsistency, an interlacing of Steps 2, 3 and 4 is proposed. The switching sequence is the one shown on Figure 5.3(b)

(a) All receivers switch to v–polarisation.

(b) Corresponding visibility map. All baselines are vv.
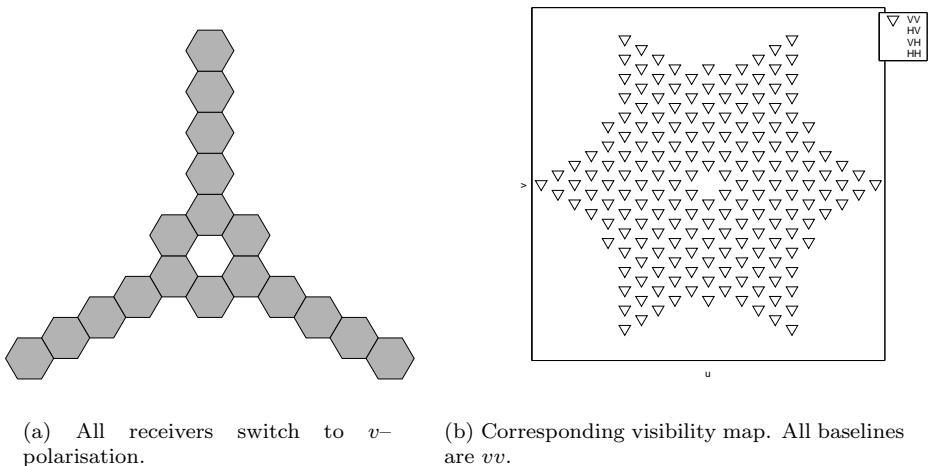
Figure 5.5: Step 1 of MIRAS' polarimetric mode.
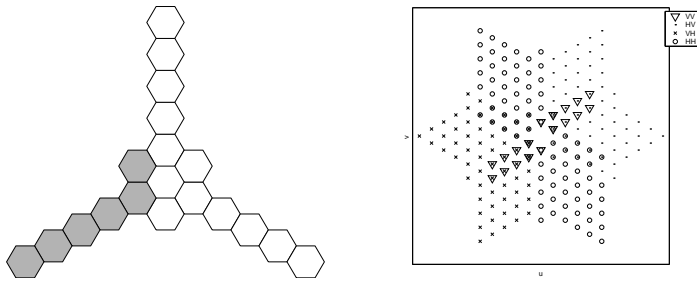
(a) Step 2: left arm in v–polarisation; others in h.
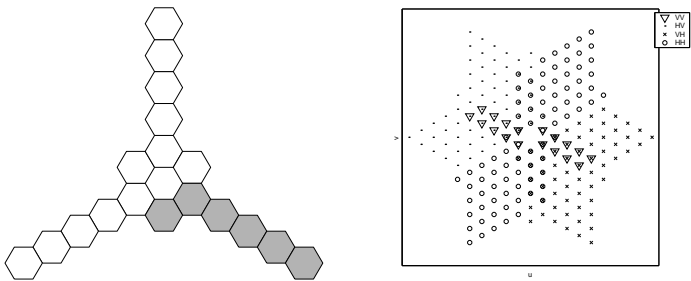
(b) Step 3: right arm in v–polarisation; others in h.
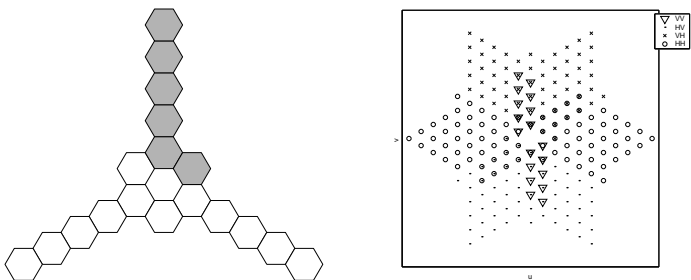
(c) Step 4: centre arm in v–polarisation; others in h.

Figure 5.6: Steps 2, 3 and 4 of MIRAS' polarimetric mode. All baselines hh, hv and vh can be obtained with this switching scheme.

for an interlacing depth of 4, meaning that Steps 2 through 4 are repeated four times within the elemental integration time τ. A new simulation has been performed with the same scenario as before. Obviously the observation time for each step slot is now shortened by one fourth, i.e. 0.1s instead of 0.4s (without interlacing) and every 0.3s a complete baseline set is produced for each polarimetric brightness temperature (hh, hv and vh). This way, all the baselines have information of the scene from the beginning, through the middle and until the end of the elemental integration time. The simulation result for T_{hh} is presented on Figure 5.7. The shape of the impulse response for T_{hh} resembles very much that of T_{vv}, obtained in Step 1 and shown in Figure 5.4(b). Both impulse responses are almost equal for practical purposes.

<div style="float:left; font-weight:bold; font-size:small">Sensitivity consideration</div>

One consideration on sensitivity is worthwhile. As seen from Figure 5.3(a), over a period of 2τ the integration time for vv is τ, while it is $\tau/3$ for hh, hv and vh. If the polarisations are reversed on the next 2τ–period, then the total integration time over 4τ is $4\tau/3$ for vv and hh and half of this ($2\tau/3$) for hv and vh. But as it has been shown in [20] the cross visibilities hv and vh are hermitic of each other and can therefore be combined, leading to an effective integration time of $4\tau/3$, the same as for vv or hh. The sensitivity of the vertical, horizontal and complex cross brightness temperatures in the MIRAS polarimetric mode is thus the same. The 4τ–switching sequence with alternating polarisations is shown on Figure 5.3(c), where interlacing has been omitted only for clarity reasons.

At this point it has to be recalled that MIRAS is an imaging radiometer with a broad field of view. Thus, each ground patch on the Earth is seen in many snapshots, at each one with a different incidence angle. The retrieval of the physical parameters is done using the polarimetric brightness temperature of the same ground patch measured for different incidence angles. It is therefore possible and interesting to avoid measurements with high noise level, as they would not add useful value to the whole sequence of measurements. This is what the switching sequence with alternating polarisation of Figure 5.3(c) achieves.

5.4   Multi-angular Fully Polarimetric Pixel Processing

<div style="float:left; font-weight:bold; font-size:small">Fully polarimetric mode simulator</div>

In order to gain some experience and to try to validate the above described procedure to measure fully polarimetric brightness temperatures some simulations have been performed. Figure 5.8 shows the structure of the small simulator that
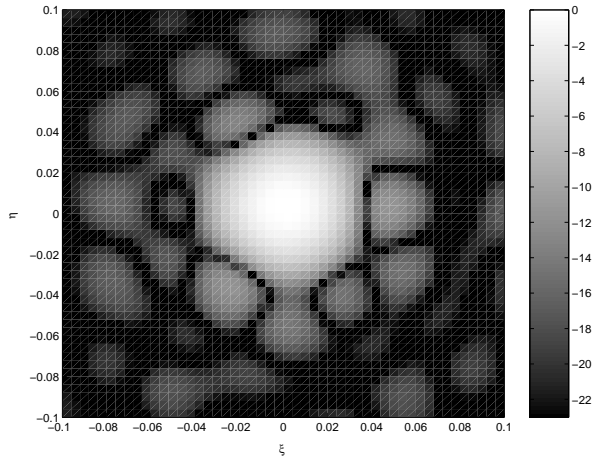
(a) Without interlacing.
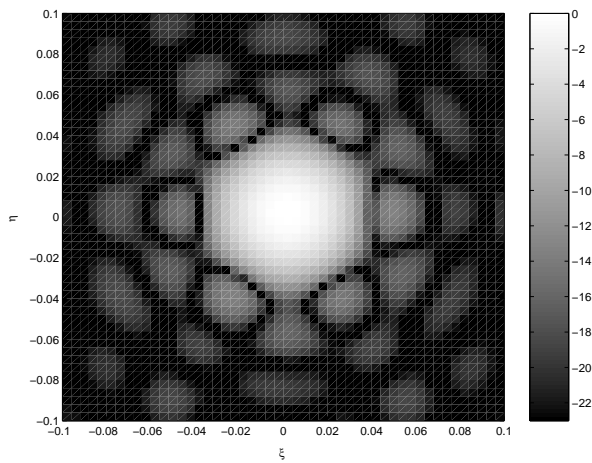
(b) Interlacing with a depth 4.

Figure 5.7: Blurring of the T_{hh} impulse response as a function of interlacing for SMOS integration time $\tau = 1.2$ s (satellite motion along η, scale in dB).
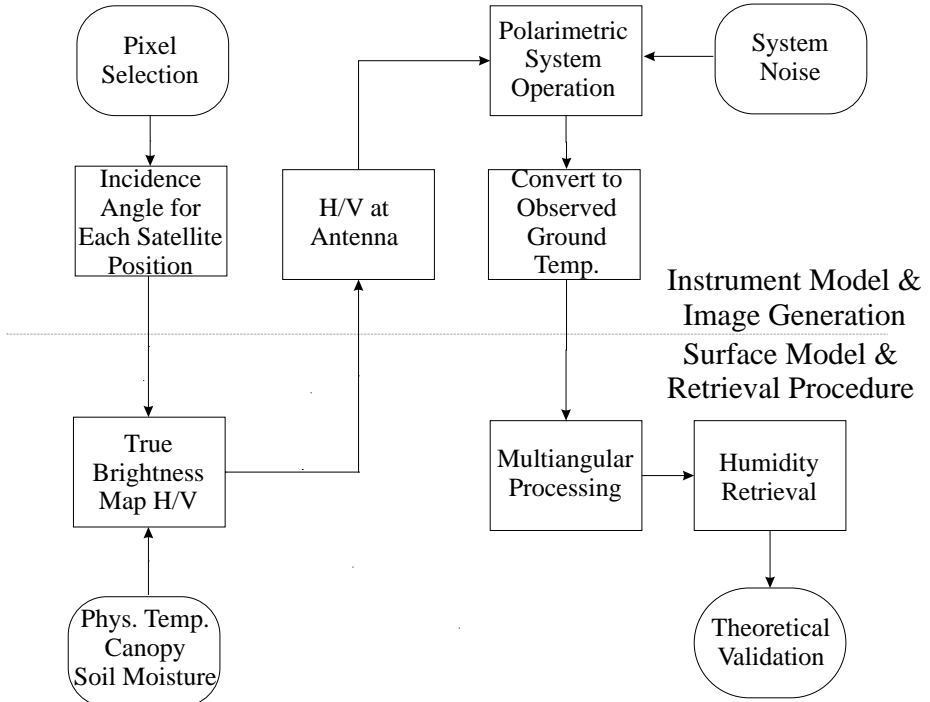
Figure 5.8: Fully polarimetric mode simulator scheme.

has been built. The procedure described in this picture is only for one ground pixel, when it is seen in different snapshots from the satellite. Figure 5.9 shows the Earth as it is seen from the satellite. The Earth horizon is clearly identified in the picture. The so-called *dwell lines* are the lines that a point on Earth follows in the field of view as the satellite moves along its orbit.

The simulator consists of 2 parts, the *Instrument Model* and the *Surface Model*. The former is the part drawn above the discontinuous line, the latter the part below in figure 5.8. The *Pixel Selection Block* computes the position on the field of view of MIRAS at which the pixel on ground will be seen for different snapshots, obtaining a list of pixel observations. A spherical non-rotating Earth and no satellite yaw-steering has been supposed for this computation. With that information and the satellite's tilt angle the incidence angle for each pixel

observation is computed in the next block (*Incidence Angle for Each Satellite Position Block*). The incidence angle data is necessary to generate the H and V brightness temperatures on Earth. This data is generated by the Surface Model of the simulator. Once the true brightness temperature on Earth has been computed the ground to antenna brightness temperature conversion of section 5.1 is done (*H/V at Antenna Block*). The instrument is modelled taking into account the antenna switching procedure of section 5.3 (*Polarimetric System Operation Block*). Noise is also added to the ideal antenna temperatures. No calibration procedure has been implemented in the simulator. Once
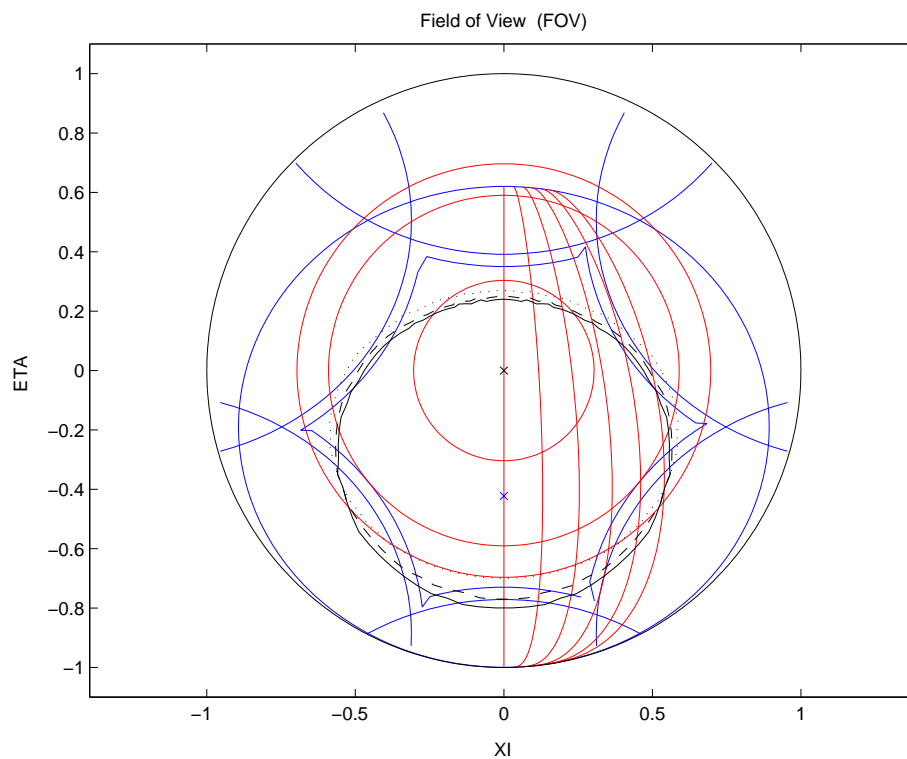
Figure 5.9: Earth as seen from MIRAS (of 21 elements per arm, spacing of 0.83λ, orbit height of 758km and tilt angle of $25°$) in the directing cosine domain.

the observed antenna brightness temperature have been obtained the retrieved ground brightness temperatures are computed. A multi-angular data processing of the obtained ground brightness temperatures is performed for the humidity retrieval. The derived physical parameters are compared with the original ones.

From equation (5.18) it is possible to obtain the fully polarimetric temperature set $(T_B^{hh}(\xi, \eta), T_B^{hv}(\xi, \eta), T_B^{vh}(\xi, \eta), T_B^{vv}(\xi, \eta))$ at the antenna, for any observed pixel. The 4-steps switching sequence of section 5.3 (figure 5.3, page 112) implies that not all 4 temperatures at the antenna can be measured at the same time. The simulator takes this into account and computes the temperatures on Earth for every of the 4 steps $(T_B^{HH}(\xi_i, \eta_i), T_B^{HV}(\xi_i, \eta_i), T_B^{VH}(\xi_i, \eta_i), T_B^{VV}(\xi_i, \eta_i))$ with $i = 1, 2, 3, 4$. The temperatures at the antenna are also computed for each step. The combination of steps 2, 3 and 4 in order to obtain the hh, hv and vh temperatures at the antenna is simulated by taking the mean value of the temperatures during the 3 steps

$$\overline{T}_B^{hh} = \frac{1}{3} \sum_{k=2}^{4} T_B^{hh}(\xi_k, \eta_k) \tag{5.23}$$

$$\overline{T}_B^{hv} = \frac{1}{3} \sum_{k=2}^{4} T_B^{hv}(\xi_k, \eta_k) \tag{5.24}$$

$$\overline{T}_B^{vh} = \frac{1}{3} \sum_{k=2}^{4} T_B^{vh}(\xi_k, \eta_k) \tag{5.25}$$

As the vertical antenna temperature is obtained in a single step

$$\overline{T}_B^{vv} = T_B^{vv}(\xi_1, \eta_1) \tag{5.26}$$

In matrix form this can be written as

$$
\begin{pmatrix} \overline{T}_B^{hh} \\ \overline{T}_B^{hv} \\ \overline{T}_B^{vh} \\ \overline{T}_B^{vv} \end{pmatrix} = \begin{bmatrix} 0 & 0 & 0 & 0 \\ 0 & 0 & 0 & 0 \\ 0 & 0 & 0 & 0 \\ & \mathbf{m_1^4} & & \end{bmatrix} \begin{pmatrix} T_B^{HH}(\xi_1, \eta_1) \\ T_B^{HV}(\xi_1, \eta_1) \\ T_B^{VH}(\xi_1, \eta_1) \\ T_B^{VV}(\xi_1, \eta_1) \end{pmatrix} +
$$

$$
\frac{1}{3} \sum_{k=2}^{4} \begin{bmatrix} & \mathbf{m_k^1} & & \\ & \mathbf{m_k^2} & & \\ & \mathbf{m_k^3} & & \\ 0 & 0 & 0 & 0 \end{bmatrix} \begin{pmatrix} T_B^{HH}(\xi_k, \eta_k) \\ T_B^{HV}(\xi_k, \eta_k) \\ T_B^{VH}(\xi_k, \eta_k) \\ T_B^{VV}(\xi_k, \eta_k) \end{pmatrix} \tag{5.27}
$$

In this equation it can be seen clearly that $\overline{T}_B^{vv}$ is obtained in the first switching step and $\overline{T}_B^{hh}$, $\overline{T}_B^{hv}$ and $\overline{T}_B^{vh}$ are obtained as a combination of the temperature for hh, hv and vh of steps 2, 3 and 4. In a simplified manner we can write

$$\mathbf{t} = [M_1]\,\mathbf{T_1} + \frac{1}{3}\sum_{k=2}^{4}[M_k]\,\mathbf{T_k} \tag{5.28}$$

where $\mathbf{t}$ refers to the temperatures at the antenna, $\mathbf{T_k}$ the temperatures on ground for steps k, $[M_i]$ are the transform matrices and the sub-indices indicate the corresponding step. It has to be noted that $[M_1]$ is zero except in the fourth row as it takes only into account the vv polarisation at the antenna and $[M_k]$ for $k = 2, 3, 4$ is zero in the fourth as it does not take into account the vv polarisation.

If the integration time is short enough, so that the position of the observed pixel does not change very much during one integration time, and the brightness temperatures on Earth can be considered constant the previous equation can be simplified yielding

$$\mathbf{t} = [M_A]\,\mathbf{T_A} + [M_B]\,\mathbf{T_B} \tag{5.29}$$

It is clear that $[M_A] = [M_1]$, $\mathbf{T_A} = \mathbf{T_1}$, $\mathbf{T_k} = \mathbf{T_B}$ for $k = 2, 3, 4$ and $[M_B] = [M_3]$. In this case the subindex 3 has been chosen as the matrix for the third switching step is the best approximation for the matrices of steps 2 and 4. If the temperatures on Earth $\mathbf{T_A}$ and $\mathbf{T_B}$ do not change very much as the incidence angles are very similar (differences of the order of tenth of degree) from one measurement to the next one, we can take them as equal

$$\mathbf{T} = \mathbf{T_A} = \mathbf{T_B} \tag{5.30}$$

obtaining

$$\mathbf{t} = ([M_A] + [M_B])\,\mathbf{T} = [M]\,\mathbf{T} \tag{5.31}$$

The brightness temperature on Earth can be estimated with

$$\hat{\mathbf{T}} = [M]'\,\mathbf{t} + \mathbf{n} = [M]'\,([M_A] + [M_B])\,\mathbf{T} + [M]'\,\mathbf{n} \tag{5.32}$$

where the noise of the instrument has been taken into account with $\mathbf{n}$ and having

$$[M]' = [M]^{-1} = \begin{bmatrix} \mathbf{m_3^1} \\ \mathbf{m_3^2} \\ \mathbf{m_3^3} \\ \mathbf{m_1^4} \end{bmatrix}^{-1} \tag{5.33}$$
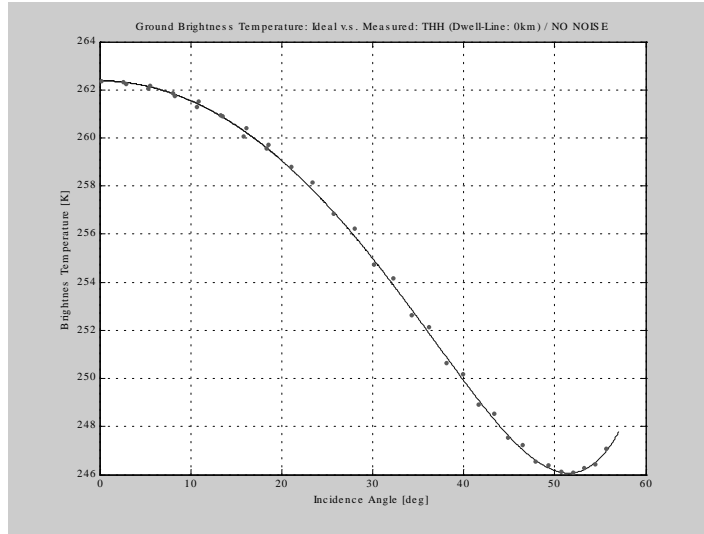
Figure 5.10: The retrieval of T_{HH} performance with the switching sequence approximations.

This matrix is not the ideal frame conversion matrix from the beginning as it takes into account that the vv measurement at the antenna has been taken in the first switching step, while the other three measurements have been taken approximately in step 3. As the ideal and the real $[M]$ are very similar no problems are expected.

Simlation results   The above described procedure has been simulated for a specific ground radiation signature and for a specific satellite setup, very similar to the SMOS baseline. The noise of the radiometer has been fixed to zero. Figure 5.10 shows the original simulated brightness temperature on Earth (solid line), and the ones obtained after programming the above expressions (dots). It can be seen that only very small difference between both values are obtained, justifying thus the above approximations. The data corresponds to the dwell line at 0km from the sub-satel.lite track.

When adding some noise according to the receiver model described above, it can be also seen that the retrieval of the ground temperatures gives good results. It can be also verified that the physical parameter retrieval seems feasible from the data presented in the following pictures. In figure 5.11 it is presented the original simulated and the retrieved temperatures on ground for HH and VV correlations. The noisy measurements follow perfectly the original temperature curve. From that curve a multi-angular processing of the temperatures to obtain the physical parameters seems totally feasible.

The retrieval of the physical parameters has also done, but only for one case. Thus it is not significant, but can give some idea about the capabilities of the method. Many simulations for several types of terrain and many noise realisations should be performed.

Dwell-lines at 0 km, 216 km and 389 km from the sub-satellite track have been simulated. The error in the retrieval of soil moisture was 1% for the 0 km dwell-line (36 incidence samples) and 2% for the 216 km dwell-line (32 incidence samples). No result could be obtained to for the 389 km dwell-line as only 8 incidence samples were on this line. This result is not conclusive at all, but indicates that at the border of the field of view it will be more difficult to obtain good results.

In figure 5.12 the original HV and VH temperatures are shown with their obtained results. The original temperatures HV and VH are supposed zero for any incidence angle. The result of the simulation shows that the noisy measured temperatures are also aligned to the zero Kelvin line.

The antenna temperatures T_{hh} and T_{vv} (and also T_{hh}, T_{vv}) may have different values for the same incidence angle on Earth. This can happen when a pixel on Earth is seen twice (in different measurements) with the same incidence angle, but in a different location in the field of view. In that case the transform $[M]$ of equation (5.19) is different for both observations and thus the resulting antenna temperatures are different. Figure 5.13 shows this.

Another interesting result is to observe the temperatures at the antenna. The simulations show clearly that even being the ground temperatures equal to zero for $T_{HV} = 0$ and $T_{VH} = 0$ the pixel to antenna transformation makes T_{hv} and T_{vh} different to zero when measured at the antennas. These antenna temperatures can even be negative, as they don't represent any physical equivalent temperature. These can be seen in figure 5.14.
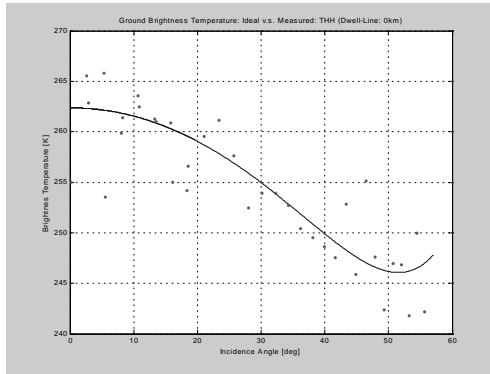
(a) T_{HH} ground temperature.
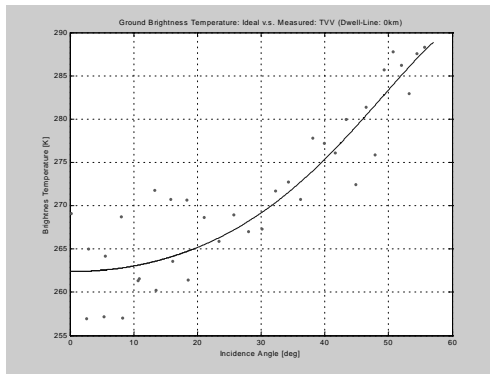
(b) T_{VV} ground temperature.

Figure 5.11: Retrieved T_{HH} and T_{VV} temperatures on ground with noisy receiver in fully polarimetric mode.
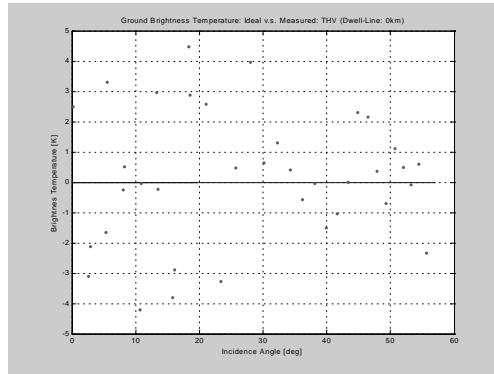
(a) HV Ground Temperature.
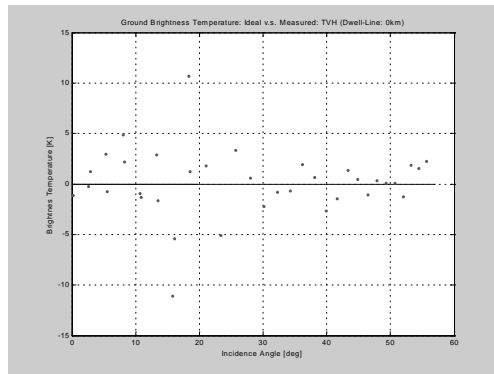
(b) VH Ground Temperature.

Figure 5.12: Retrieved T_{HV} and T_{VH} temperatures on ground with noisy receiver in fully polarimetric mode.
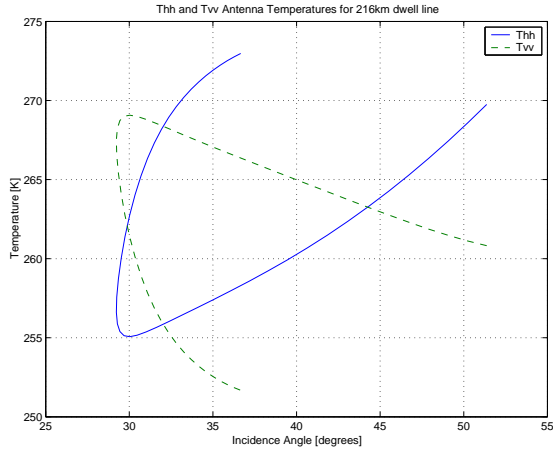
Figure 5.13: T_{hh} and T_{vv} temperatures at the antenna.
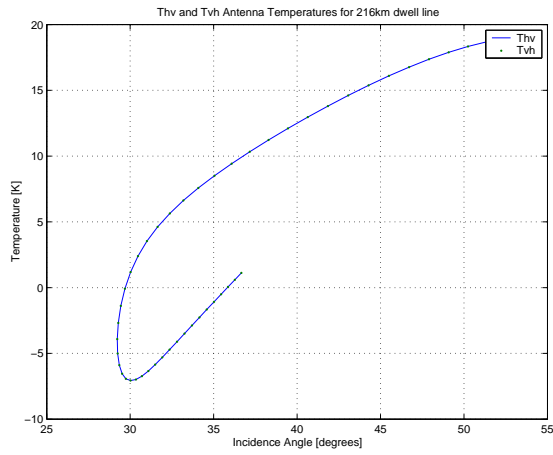
Figure 5.14: T_{hv} and T_{vh} temperatures at the antenna.

Chapter 6

Faraday Rotation Correction Method applied to MIRAS

6.1 Introduction

Faraday rotation is an important issue to be taken into account in earth observing space borne L-band radiometers as it may have a non-negligible effect on the retrieved physical parameters. This has been studied by other authors for ocean surface salinity [48, 49]. Different authors have proposed methods to compensate or measure the effect of Faraday rotation. In [50] a method that consists in measuring only the H and V polarisations in the antenna frame has been proposed. The sum of those two components corresponds to the first Stokes parameter, which is independent of the Faraday rotation. In [51], under the assumption that the ground emission is zero for the third and fourth Stokes parameters, and using polarimetric measurements it is shown how the actual Faraday rotation can be estimated. In [52] both previous methods are discussed and compared.

An original idea of this thesis is the alternative approach to those above that uses polarimetric measurements and assumes that the cross-correlation between H and V on ground is zero. As it is shown in the literature this assumption is valid for specific targets at L-band [53]. Instead of computing analytically the

Faraday rotation, we obtain the vertical and horizontal brightness temperatures by searching a polarisation basis that makes the cross-polarisation equal to zero. That is equivalent to diagonalising the measured brightness temperature coherency matrix. How this method might be used in the SMOS is has also been studied.

6.2   Mathematical Background

Rotation of brightness temperature matrices

Let the analytic field being emitted by an element of surface on ground be

$$d\tilde{\mathbf{E}} = \left(\begin{array}{c} d\mathbf{E}_H \\ d\mathbf{E}_V \end{array} \right) \tag{6.1}$$

with $d\mathbf{E}_H$ and $d\mathbf{E}_V$ the electric field components in the horizontal and vertical polarisation frame on ground. Its coherency matrix is described through

$$[\mathbf{J}_{HV}] = \left\langle \left(\begin{array}{c} d\mathbf{E}_H \\ d\mathbf{E}_V \end{array} \right) \left(\begin{array}{cc} d\mathbf{E}_H & d\mathbf{E}_V \end{array} \right)^* \right\rangle =$$

$$= \left[\begin{array}{cc} \mathbf{J}_{HH} & \mathbf{J}_{HV} \\ \mathbf{J}_{VH} & \mathbf{J}_{VV} \end{array} \right] \tag{6.2}$$

where $<>$ means expectation. In [20] it is shown that the electric field $(d\mathbf{E}_X \ d\mathbf{E}_Y)^\top$ at the antenna probes X,Y which define the polarisation frame of the antenna is related to the emitted field $(d\mathbf{E}_H \ d\mathbf{E}_V)^\top$ through a rotation matrix. This matrix includes the geometric rotation which arises when antenna and ground frames are not aligned, as well as the effect of the effective length of the antenna when the radiation does not incide the antenna from bore sight. An additional rotation angle will be present due to the Faraday rotation introduced by the ionosphere. The relationship between the emitted and inicident electric fields is then

$$\left(\begin{array}{c} d\mathbf{E}_X \\ d\mathbf{E}_Y \end{array} \right) = [R] \left(\begin{array}{c} d\mathbf{E}_H \\ d\mathbf{E}_V \end{array} \right) \tag{6.3}$$

where the rotation matrix $[R]$ is the product of two rotation matrices, the first one describing the rotation due to the geometry $[R_G]$ and the second one describing the Faraday rotation $[R_F]$

$$\begin{aligned} [R] &= [R_G] [R_F] = \\ &= \left[\begin{array}{cc} \cos\psi & -\sin\psi \\ \sin\psi & \cos\psi \end{array} \right] \left[\begin{array}{cc} \cos\Delta\Phi & -\sin\Delta\Phi \\ \sin\Delta\Phi & \cos\Delta\Phi \end{array} \right] \end{aligned} \tag{6.4}$$

being ψ the rotation angle due to geometry and $\Delta\Phi$ the Faraday rotation. From the above equations the coherency matrix at the antenna frame can be written as

$$[\mathbf{J}_{XY}] = [R]\,[\mathbf{J}_{HV}]\,[R]^\top \tag{6.5}$$

In [20] the proportionality between coherency matrix and antenna temperatures is written as

$$[\mathbf{J}_{HV}] = \frac{k_B T_{ph}}{\lambda_0^2}\frac{da}{r^2}\delta_a(0)\,[\mathbf{e}_{HV}] = \frac{k_B}{\lambda_0^2}\frac{da}{r^2}\delta_a(0)\,[\mathbf{T}_{HV}] \tag{6.6}$$

where $k_B = 1.38 \times 10^{-23}\,J/K$ is the Boltzmann's constant, T_{ph} is the physical temperature, da is the element of radiating area, r is the distance to the radiometer, $\delta_a(0)$ is the analytic delta function evaluated at zero, $[\mathbf{e}_{HV}]$ is the polarimetric spectral emissivity matrix and $[\mathbf{T}_{HV}]$ is the polarimetric brightness temperature matrix. Using this proportionality property equation (6.5) can be rewritten as

$$[\mathbf{T}_{XY}] = [R]\,[\mathbf{T}_{HV}]\,[R]^\top \tag{6.7}$$

and polarimetric brightness temperatures can be used directly.

6.3 Faraday Rotation Compensation

In order to invert equation (6.7) it is necessary to know the rotation matrix $[R]$. The first rotation due to geometry $[R_G]$ can be deduced from the position and attitude of the satellite and the observed point on earth. The rotation due to the Faraday rotation is not known, as it depends on the actual Total Electron Content (TEC) at the time of measurement. Thus an additional TEC measurement would be necessary to invert (6.7).

Diagonalisation of the brightness temperature matrix

However, for the special case where the radiation on ground has no cross-polarisation between H and V it is not necessary to know the TEC. The temperature matrix $[\mathbf{T}_{HV}]$ is diagonal ($\mathbf{T}_{HV} = \mathbf{T}_{VH} = 0$) and equation (6.7) is a simple diagonalisation equation. Thus the inversion of the coherency matrix $[\mathbf{T}_{XY}]$ reduces to the computation of its corresponding diagonal matrix [54]. As an important consequence the Faraday rotation needs not to be estimated using a TEC measurement, in order to obtain the coherency matrix on ground, furthermore Faraday rotation can be estimated from the obtained $[R]$ matrix with

$$[R_F] = [R_G]^\top\,[R] \tag{6.8}$$

as $[R_G]$ is obtained from the geometry of the observation.

The diagonalisation process takes advantage of the polarisation state of the wave to find a polarisation reference frame that does not show cross-correlation between orthogonal channels. The eigenvalues describe the power in each polarisation of the wave on ground.

The assumption of no cross-polarisation between H and V channels can be accepted at L-band when observing the ocean. Experimental results show that the cross-polarisation is below 0.2K for the complete azimuth range at a wind speed of 11m/s and at an incidence angle of 45° [53], while the instrumental sensitivity of the inverted temperatures is of the order of 3-4K (see section 6.5.3). When observing a terrestrial scene this is not true at least for ploughed and crop fields [55]. Fortunately for the SMOS mission azimuthal dependence may cancel out due to the large pixel size (30-50km).

The impact of an existing cross-polarisation on the diagonalisation method has been studied. It means that the coherency matrix $[\mathbf{T}_{HV}]$ is not diagonal and has the form

$$[\mathbf{T}_{HV}] = \begin{bmatrix} \mathbf{T}_{HH} & \mathbf{T}_{HV} \\ \mathbf{T}_{HV}{}^{*} & \mathbf{T}_{VV} \end{bmatrix} \qquad (6.9)$$

Note that the off-diagonal elements are complex conjugates of each other.

Now we diagonalise the coherency matrix at the antenna $[\mathbf{T}_{XY}]$, taking into account that the original coherency matrix on ground has the from (6.9). The eigenvalues of $[\mathbf{T}_{XY}]$ are the same as from $[\mathbf{T}_{HV}]$ because they are related through a similarity transformation (6.7) [54]. It is easy to prove that the eigenvalues of $[\mathbf{T}_{HV}]$ will be

$$\lambda_{1,2} = \frac{\mathbf{T}_{HH} + \mathbf{T}_{VV}}{2} \mp \frac{\sqrt{(\mathbf{T}_{HH} - \mathbf{T}_{VV})^2 + 4|\mathbf{T}_{HV}|^2}}{2} \qquad (6.10)$$

From this expression it can be seen that the estimated brightness temperatures will be

$$\hat{\mathbf{T}}_{HH} = \lambda_1$$
$$\hat{\mathbf{T}}_{VV} = \lambda_2$$

and will correspond to $\mathbf{T}_{HH}$ and $\mathbf{T}_{VV}$ respectively when the term $\mathbf{T}_{HV}$ is zero (ideal case). The accuracy of the diagonalisation procedure when applied to non-ideal targets can be obtained by taking the difference between the ideal temperatures $\mathbf{T}_{HH}$, $\mathbf{T}_{VV}$ and the estimated temperatures $\hat{\mathbf{T}}_{HH}$, $\hat{\mathbf{T}}_{VV}$. From

equation (6.10) it can be seen that a worse case accuracy will be obtained when $\mathbf{T}_{VV} = \mathbf{T}_{HH}$ (normal incidence) and it will be equal to $|\mathbf{T}_{HV}|$. For $|\mathbf{T}_{HV}| \approx 0.5\text{K}$ at $45°$ incidence angle and $\mathbf{T}_{VV} \approx 115\text{K}$, $\mathbf{T}_{HH} \approx 65\text{K}$ the accuracy will be better than 5mK.

This result can be further improved if we notice that the imaginary part of T_{HV} corresponds to the fourth Stokes parameter (disregarding a proportionality factor) and that the fourth Stokes parameter is invariant to rotation. The imaginary part of equation (6.7) corresponds uniquely to the contribution of $Im\{T_{HV}\}$. It can be easily shown that the imaginary parts at both sides of the matrix equations are equal, showing the invariant property of the fourth Stokes parameter. Thus the imaginary part can be directly separated from this equation. The new resulting equation would be now

$$Re\{[\mathbf{T}_{XY}]\} = [R]\,Re\{[\mathbf{T}_{HV}]\}\,[R]^{\top} \tag{6.11}$$

6.4 Effect of the Atmosphere

Now the emission and absorption effects of the atmosphere are addressed. Absorption by the atmosphere of the ground radiation is modelled by a reduction of the amplitude of the radiated fields. Up welling emission by the atmosphere is expressed with an additive electric field, while down welling emission is reflected on the earth's surface and propagates then through the attenuating atmosphere to the sky. These effects have been modelled with

Atmospheric effects

$$\begin{pmatrix} d\mathbf{E}'_H \\ d\mathbf{E}'_V \end{pmatrix} = \begin{pmatrix} d\mathbf{E}_{A_H} \\ d\mathbf{E}_{A_V} \end{pmatrix} +$$
$$a\left(\begin{bmatrix} \gamma_H & 0 \\ 0 & \gamma_V \end{bmatrix} \begin{pmatrix} d\mathbf{E}_{D_H} \\ d\mathbf{E}_{D_V} \end{pmatrix} + \begin{pmatrix} d\mathbf{E}_H \\ d\mathbf{E}_V \end{pmatrix} \right) \tag{6.12}$$

where $(d\mathbf{E}'_H\,d\mathbf{E}'_V)^{\top}$ is the total electric field at the top of the atmosphere expressed in the ground frame, $(d\mathbf{E}_H\,d\mathbf{E}_V)^{\top}$ is the field emitted by the ground, a is a factor which models attenuation ($0 \leq a \leq 1$), $(d\mathbf{E}_{A_H}\,d\mathbf{E}_{A_V})^{\top}$ is the up welling emission from the atmosphere and $(d\mathbf{E}_{D_H}\,d\mathbf{E}_{D_V})^{\top}$ is the down welling atmospheric emission. Finally, γ_H and γ_V are the Fresnel reflection coefficients for horizontal and vertical polarisations. It has been assumed, that if the surface emission matrix is diagonal it is also reasonable to think that so will be its scattering matrix. Therefore, the Fresnel reflection coefficients have been used to

model the reflection of the down welling atmospheric emission on earth. Substituting this new field vector into (6.7), the polarimetric brightness temperature $[\mathbf{T}_{XY}]$ at the antenna frame yields

$$[\mathbf{T}_{XY}] =$$
$$[R]\left([\mathbf{T}_{A_H A_V}] + a^2\left([\mathbf{T}_{HV}] + [\Gamma_{HV}][\mathbf{T}_{D_H D_V}]\right)\right)[R]^{\top} \qquad (6.13)$$

where $[\mathbf{T}_{HV}]$ is the temperature matrix of the ground radiation and $[\mathbf{T}_{A_H A_V}]$ is the temperature matrix of the up welling atmospheric emission, $[\mathbf{T}_{D_H D_V}]$ is the down welling atmospheric emission and $[\Gamma_{HV}] = \mathrm{diag}(|\gamma_H|^2, |\gamma_V|^2)$ is a diagonal matrix modelling the reflection on earth of the down welling atmospheric emission. The coherency matrices of the atmospheric up and down welling emission will also be diagonal matrices. Thus, the overall emission at the top of the atmosphere will have a diagonal coherency matrix and the diagonalisation procedure can be used to invert equation (6.13). In this case the eigenvalues (diagonal elements) of the total temperature matrix will be the sum of powers of attenuated ground emission plus atmospheric up welling emission plus reflected and attenuated down welling emission.

6.5   Simulation Results

6.5.1   General Overview

Several computer simulations have been done using the above expressions. The goal is to see if this procedure can also be used in combination with MIRAS' fully-polarimetric mode implementation [20].

Simulation description

The simulator computes the position of the satellite at any time and takes also into account the rotation of the earth. The chosen orbit during the simulations has been the SMOS baseline configuration, a dawn-dusk orbit at 755km height and with and array tilt of 32°. No yaw-steering has been used in the simulations. In the simulator the satellite's position at $t = 0$ is Lat.=0°, Long.=0° (ascending orbit).

For each time instant the antenna frame and the local incidence frame are calculated. These are used to reckon the incidence angle on ground from which the brightness temperature on ground is obtained following a simple emission model (using Fresnel's reflection coefficients) for a flat dielectric surface [56] with $\epsilon_r = 72.1 - j74.5$, which is equivalent to a sea surface salinity of 38psu at 20°C using Blanch & Aguasca's permittivity model for sea water [57]. At this point also the effect of the atmosphere on the brightness temperature is

taken into account following what has been explained in section 6.4 and the absorption and emission models described in [58]. Therefore the *U.S. Standard Atmosphere, 1962* (without rain) has been used, which is also described in [58]. The rotation matrix due to the geometry $[R_G]$ can be computed with the known antenna and ground frames.

To obtain the Faraday rotation the approach shown in [48] has been followed and adapted to the needs of the MIRAS sensor. It consists in considering 400km as the height of the ionosphere. The point where the emitted ground radiation crosses the ionosphere in its path to the antenna has been reckoned. At this point the Vertical Total Electron Content (VTEC) [59] and the geomagnetic field [60] have been calculated. This leads to the Faraday rotation angle $\Delta\Phi$ in degrees that can be computed as

$$\Delta\Phi \approx 6950 B(400) \cos\Theta \sec\iota VTEC \qquad (6.14)$$

where $B(400)$ is the magnetic field in tesla, Θ is the angle between the ray path and the magnetic field and ι is the angle respect to zenith. The geomagnetic field has been computed for the 2002 epoch, while the ionospheric model has been run for January 1st, 2002, at 6:00h UT.

Due to the broad field of view of MIRAS a pixel on earth may be observed in many snapshots while the satellite moves along its orbit, each time with a different incidence angle. The collection of all these observations is known as dwell-line. Several simulations have been run for two selected pixels on earth: (Lat.=0°, Long.=0°) and (Lat.=0°, Long.=1°). Their dwell-lines can be seen in figure 6.1 which shows MIRAS' field of view in the direction cosine domain. The unit circle corresponds to the visible field of view, also known as *sky horizon*. The ellipse in the centre of the image corresponds to the earth. The dotted and dashed lines correspond to *sky aliases* and *earth aliases* respectively, which appear during the image generation process [61]. The dashed-dotted ellipses correspond to constant incidence circles on ground for 20° and 50° incidence angles. The cross is the sub-satellite point.

A dwell-line that crosses the centre of the field of view consists of approximately 60 measurements. This number arises from the fact that the satellite observes a pixel when it's incidence angle is in the range of 0° − 60°. This corresponds to an arc on the earth's surface of about 9°. Taking into account the angular velocity of the satellite for the 755 km orbit, the pixel is in the field of view during about 150 seconds. At 1.2s per snapshot and two snapshots to obtain the complete polarimetric brightness temperature matrix with MIRAS the above mentioned number of points per dwell-line is obtained.
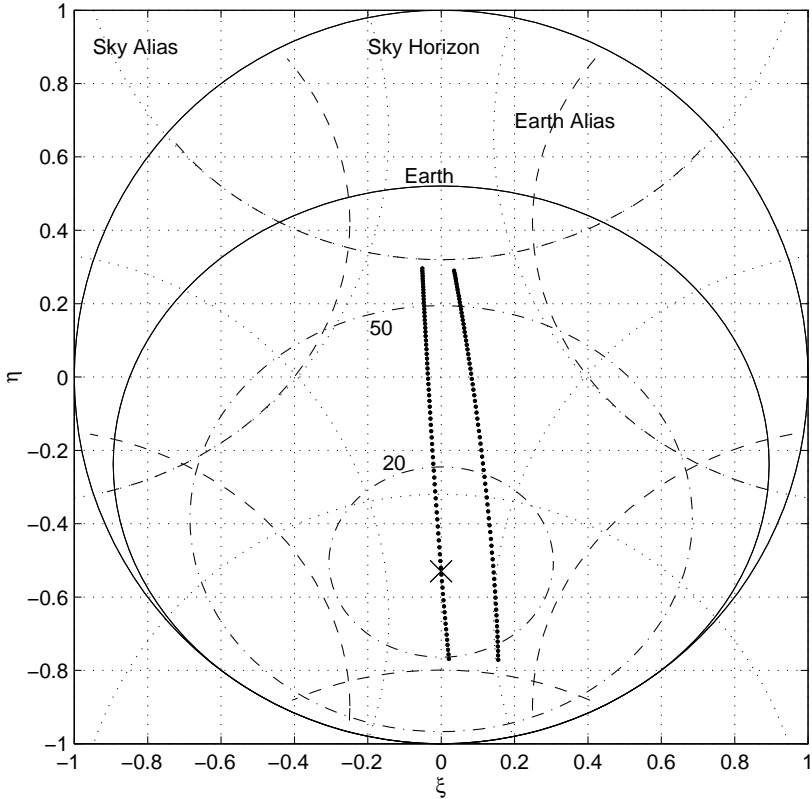
Figure 6.1: Dwell-lines of pixels (Lat.$=0°$, Long.$=0°$) and (Lat.$=0°$, Long.$=1°$).

6.5.2   Ideal Cases

Ideal
measurement

The first simulation consisted in applying the diagonalisation inversion explained above to each single snapshot. Implicitly this assumes that in each snapshot all four elements of the coherency matrix of (6.7) can be measured. That would be the case for an interferometric radiometer where each receiver is fully polarimetric. No noise has been added to these simulated measurements. Figure 6.2 shows in a solid line the emitted radiation from ground (without atmospheric effects) and in a dashed line the retrieved brightness temperatures at the top of the atmosphere. An expected small increment of about 2K (not constant
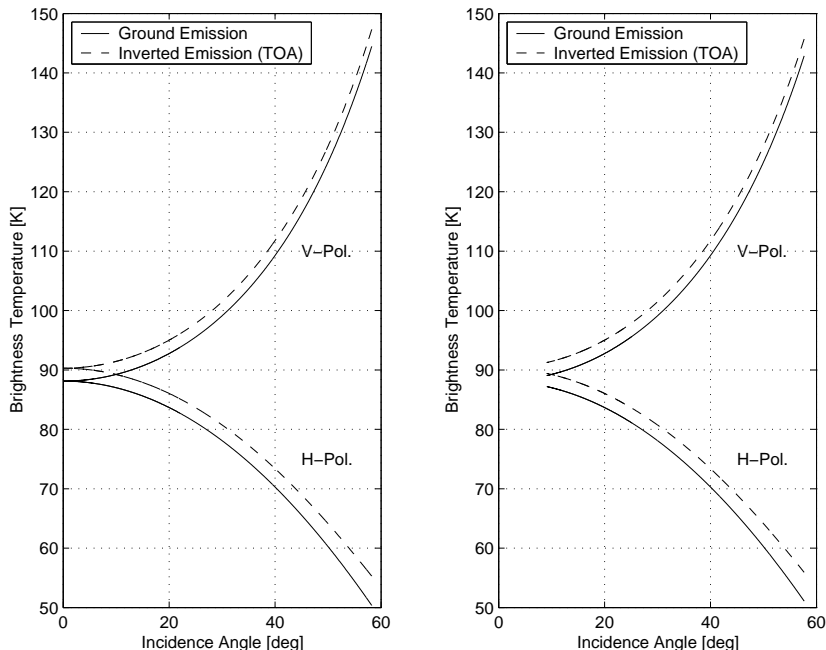
Figure 6.2: Emitted (ground) and inverted (Top Of the Atmosphere, TOA) brightness temperature for an ideal polarimetric radiometer. The retrieved brightness temperature at the top of the atmosphere is about 2K larger (not constant over the whole incidence angle range) than the emission on ground due to the atmospheric emission. Left: pixel (Lat.=0°, Long.=0°). Right: pixel (Lat.=0°, Long.=1°).

over the whole incidence angle range) in the retrieved temperatures due to the atmospheric emission and absorption of the atmosphere can be observed. It should be noted that in each simulation presented in this paper the inversion has been done until the brightness at the top of the atmosphere (TOA) has been obtained (diagonalisation of (6.13)) as the correction of the atmospheric effects is not the issue of this paper. To correct the atmospheric emission and absorption it would be necessary to know the state of the atmosphere during the measurement. The left-hand plot corresponds to the data of point (Lat.=0°, Long.=0°) and the right-hand plot to the point (Lat.=0°, Long.=1°).

　　The second simulation consisted in applying the antenna switching procedure of [20], which achieves a polarimetric operation of MIRAS using its dual polarised single-channel receivers. In that switching procedure each receiver is connected to one specific antenna probe (H or V) in order to obtain the complete set of polarimetric visibilities (HH,HV,VH,VV) in four switching steps. It means that the four elements of the coherency matrix are measured at consecutive instants, which causes some distorting effects. For instance, the brightness temperature T_{xx} at the antenna is measured in the first integration interval of 1.2s, the remaining T_{xy}, T_{yx} and T_{yy} are measured all three in a second interval of 1.2s. The interlacing of the polarimetric mode of MIRAS has also been taken into account taking the mean value of measured brightness temperatures during the integration intervals. During the simulation no visibilities have been computed, assuming that the radiometer is ideal and that all systematic receiver errors can be calibrated perfectly.

With the four polarimetric brightness temperatures the coherency matrix has been built and inverted with the proposed diagonalisation method. Again the atmospheric contribution has not been corrected for after diagonalisation and thus the inverted temperatures present a slightly higher value than the emitted ground temperatures. The incidence angle has been taken as the mean incidence angle during the two integration intervals of 1.2s. Figure 6.3 shows the retrieved brightness temperatures (with dots) compared to the ones obtained in the first simulation (dashed line). The obtained values present a slight deviation (0.2K or less hardly appreciable in the figure) from the ideal inversion due to the fact that the polarimetric brightness temperatures have not been taken at the same instant of time. The ground emission is shown in the figure with a continuous line.

6.5.3　Realistic Cases

　In the third simulation radiometric noise has been added to the brightness temperatures at the antenna, taking into account the effective integration time for each polarimetric brightness temperature. The integration time to compute the radiometric noise has been 1.2s for T_{vv} and thus 3 times longer than for the other three brightness temperatures, as these have to share one integration interval of 1.2s. The radiometric noise has been computed following [62] and [5].
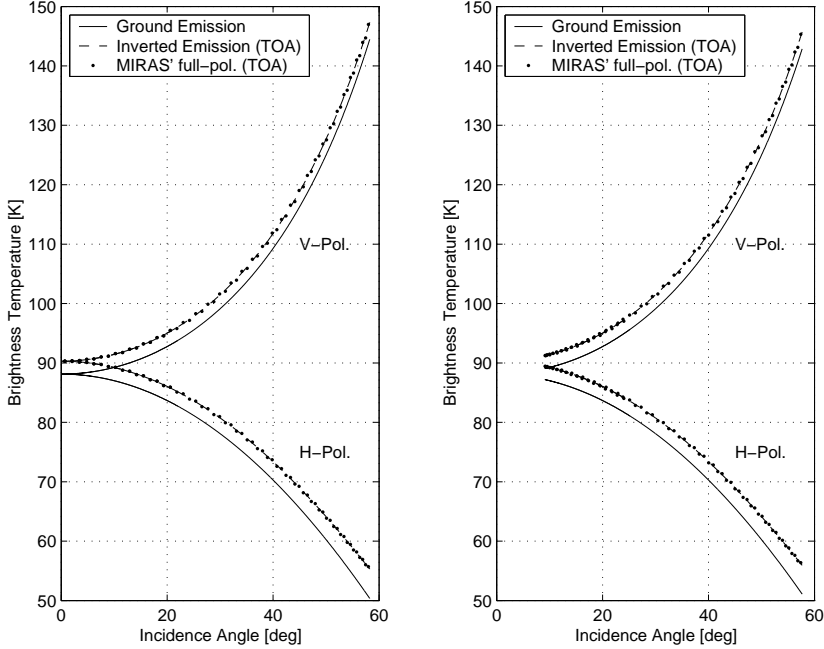
Figure 6.3: Emitted (ground), Ideal Inverted (TOA) brightness temperatures plus inverted brightness temperatures (TOA) for a noiseless MIRAS in polarimetric operation. Left: pixel (Lat.=0°, Long.=0°). Right: pixel (Lat.=0°, Long.=1°).

The sensitivity in the field of view is

$$\Delta T(\xi, \eta) \approx \frac{4\pi}{G(\xi, \eta)} \sqrt{1 - \xi^2 - \eta^2}$$
$$\frac{\sqrt{3}}{2} d^2 \frac{T_A + T_R}{\sqrt{B\tau_{eff}}} \alpha_w \frac{w_{ol}}{\alpha_f} \sqrt{N_V} \qquad (6.15)$$

where d is the distance between antenna elements expressed in wave-lengths, T_A and T_R are the antenna and receiver temperatures, the noise figure of the receivers have been assumed to be $F = 2dB$, B is the receiver bandwidth, $\tau_{eff} = \tau/Q$ the effective integration time that takes into account the use of 1bit-2level digital correlators, being $Q = 2.46$ and $\tau = 1.2s$ (or $\tau = 1.2s/3$
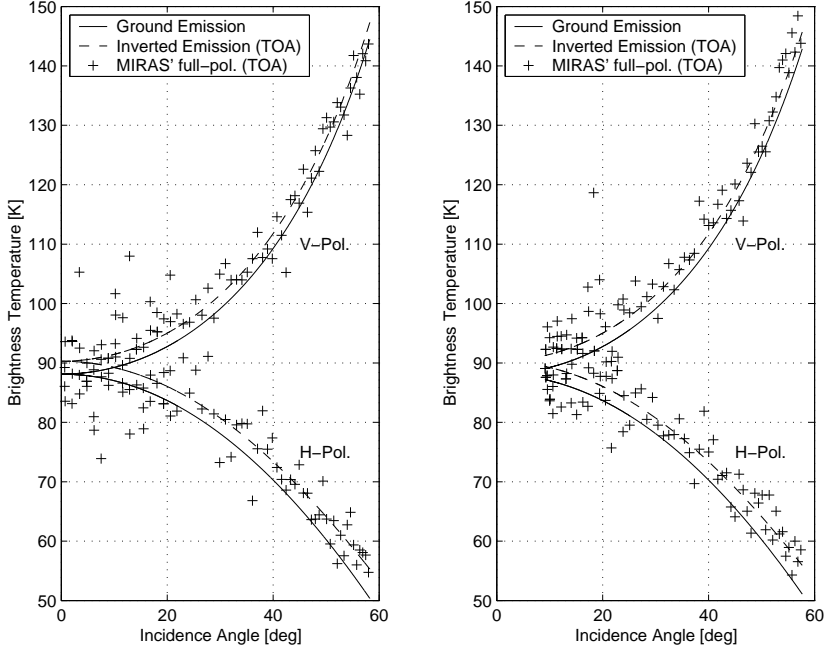
Figure 6.4: Emitted (ground), Ideal inverted (TOA) brightness temperatures plus inverted brightness temperatures (TOA) for a noisy MIRAS in polarimetric operation. Left: pixel (Lat.=0°, Long.=0°). Right: pixel (Lat.=0°, Long.=1°).

depending on the snapshot), $\alpha_w = 0.4517$ as Blackman window is assumed in the processing of the data, $\alpha_{lo} = 1$ for single side band receiver and $\alpha_f = 1.11$ as a rough estimation of the filter coefficient. $G(\xi, \eta)$ is the receiver antenna pattern and (ξ, η) the direction cosines. The element antenna pattern has been approximated by $G = G(0,0) \cos^4 \theta$ being $G(0,0) = 7.228$ the receiver antenna gain at bore sight. In the simulations instead of T_A the corresponding brightness temperatures T_{xx}, T_{xy}, T_{yx} and T_{yy} for each direction (ξ, η) have been used as no estimation for the overall antenna temperature has been computed.

It should be noted from (6.15) that the pixels at the centre of the field of view will be less noisy than the pixels at the border of it. In figure 6.1 it can be observed that measurements at low incidence angles are taken twice, one at the border of the field of view and the other one more centred. This is
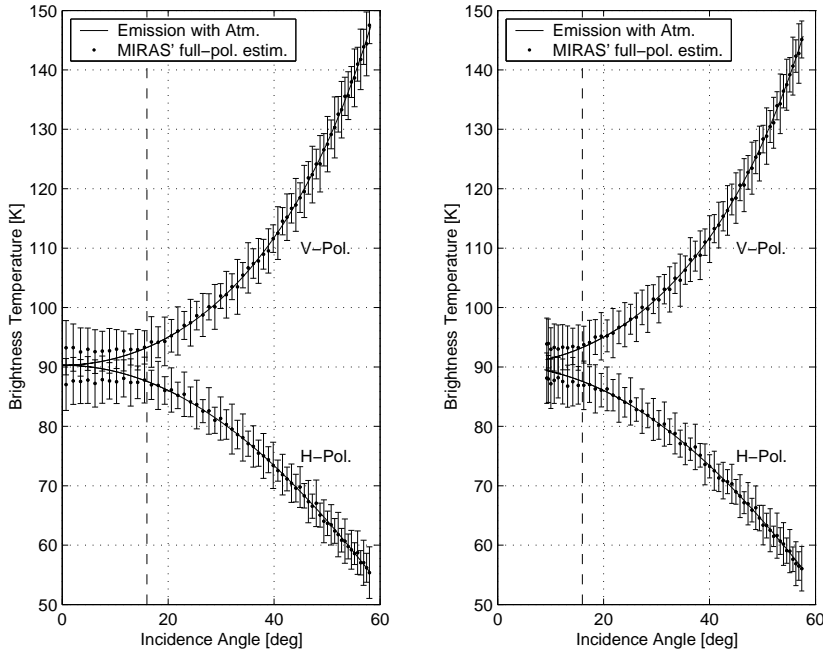
Figure 6.5: Brightness temperature estimation performance for noisy MIRAS in polarimetric operation. Left: pixel (Lat.=0°, Long.=0°). Right: pixel (Lat.=0°, Long.=1°). At low incidence angles the mean value has an offset.

reflected in figure 6.4 where the results of the inversion are shown. Some noisy measurements at lower incidence angles can be observed.

A series of 100 simulations have been run in order to obtain an estimate of the mean value and standard deviation of the retrievals. The results are shown in figure 6.5. At low incidence angles when duplicate measurements were available only the ones taken at the centre of the field of view have been used. The standard deviation of the brightness temperature estimation is between 3-4K in the incidence angle range from $20° - 40°$ and the corresponding error bars have been drawn in the figure. There it can be seen that the mean value of the estimation agrees very much with the temperatures at the antenna, except for incidence angles below $16°$ approximately. This is explained as follows.

It should be noted that the diagonalisation matrix $[R]$ of (6.13) is not unique,

Retrieval
performance
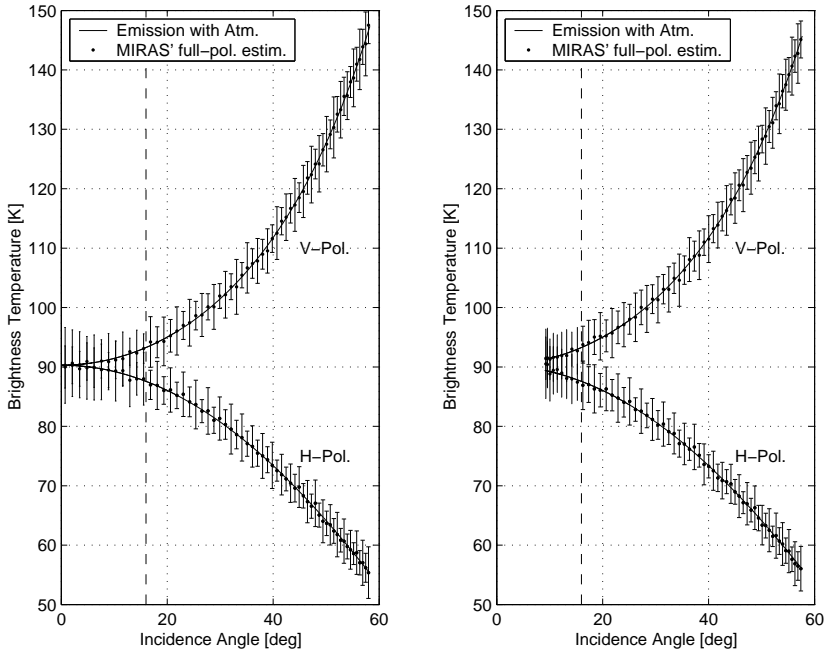
Figure 6.6: Brightness temperature estimation performance for noisy MIRAS in polarimetric operation. Estimating first the VTEC gives better results for low incidence angles. Left: pixel (Lat.=0°, Long.=0°). Right: pixel (Lat.=0°, Long.=1°).

as both diagonal elements may swap their position depending on the rotation angle used in the inversion. To distinguish between the H and V polarisations a priori information can be used to assign the largest value to V as this is the normal case. But this decision may be wrong when the target is observed at small incidence angles where H and V are very similar. In this situation the measurement uncertainty is comparable to the difference between both brightness temperatures. If this decision scheme is used anyway a small positive(negative) bias of the retrieved brightness temperature for the V(H) polarisation at low incidence angles appears.

VTEC
estimation

A solution to avoid the bias at low incidence angles due to the polarisation ambiguity is presented next. From figure 6.5 it can be seen that the wave is

relatively strongly polarised between $35°$ and $60°$ as the H and V temperatures are rather different and it is thus this data that will be used to determine the VTEC. In a first step the measured coherency matrix $[\mathbf{T}_{XY}]$ of (6.7) can be corrected for the rotation matrix $[R]$. Then the Faraday rotation can be estimated for these observations using (6.4). Once the Faraday rotation for each measurement has been obtained the VTEC can be estimated from (6.14). This VTEC value can then be used to estimate again the Faraday rotation but at lower incidence angles, which in its turn is used to completely invert (6.7) for small incidence angles. This assumes that the VTEC does not change during the time it takes to make all the measurements and that it is constant over the whole field of view. Figure 6.6 shows the estimation of the H and V brightness temperatures, where for incidence angles below $16°$ the above described method has been used. For the rest of incidence angles the diagonalisation procedure has been used. It can be seen that the estimation is not anymore biased at low incidence angles. Error bars are also shown in the figure. The standard deviation of the simulated measurements is also between 3-4K.

6.6   Non ideal Antennas

In the previous analysis it has assumed that the antennas were ideal. Now the case of non ideal antennas is addressed, for the case of a zero baseline interferometer, that is, a real aperture polarimetric radiometer. *Effect of the antennæ*

   Real antennas are not perfectly polarised, they show some degree of cross-coupling between H and V probes. The electric fields at X and Y probes of a real antenna can be related to the electric fields of an ideal antenna with

$$
\begin{pmatrix} d\mathbf{E}_x \\ d\mathbf{E}_y \end{pmatrix} = \begin{bmatrix} \sqrt{1-a^2} & b \\ a & \sqrt{1-b^2} \end{bmatrix} \begin{pmatrix} d\mathbf{E}_X \\ d\mathbf{E}_Y \end{pmatrix} = [P] \begin{pmatrix} d\mathbf{E}_X \\ d\mathbf{E}_Y \end{pmatrix} \tag{6.16}
$$

where the upper case subscripts X and Y correspond to the electric field at the ideal antenna, while the lower case subscripts x and y to the real antenna. Note that the form of the $[P]$ matrix in equation (6.16) corresponds to the case where the antenna is lossless. Thus only the cross-coupling between different polarisations has been taken into account.

   The coherency matrix of the acquired field can be easily computed and it is

$$
[\mathbf{J}_{xy}] = [P] [R] [\mathbf{J}_{HV}] [R]^{-1} [P]^{*\top} \tag{6.17}
$$

Note that now we don't have a diagonalisation equation anymore, because $[P]^{*\top} \neq [P]^{-1}$, as $[P]$ is not a rotation matrix. However, matrix $[P]$ can be

rewritten as

$$[P] = \begin{bmatrix} \cos\alpha & -\sin\beta \\ \sin\alpha & \cos\beta \end{bmatrix} \tag{6.18}$$

Angles α and β will be close to zero for a well manufactured antenna, as we want $[P]$ to be close to the identity matrix. $[P]$ can further be expressed as

$$[P] = \begin{bmatrix} \cos\rho & -\sin\rho \\ \sin\rho & \cos\rho \end{bmatrix} \begin{bmatrix} \cos\delta & \sin\delta \\ \sin\delta & \cos\delta \end{bmatrix} \tag{6.19}$$

being

$$\alpha = \rho + \delta \tag{6.20}$$
$$\beta = \rho - \delta \tag{6.21}$$
$$\tag{6.22}$$

Thus, $[P]$ can be separated into two matrices

$$[P] = [P_\rho][P_\delta] \tag{6.23}$$

being $[P_\rho]$ a *rotation* matrix and $[P_\delta]$ a *deformation* matrix. $[P_\rho]$ describes how the antenna frame is rotated respect to the ideal axes. $[P_\delta]$ describes how the polarisations deviate from the ideal orthogonal state. If equation (6.16) is rewritten

$$\begin{aligned} [\mathbf{J}_{xy}] &= [P][R][\mathbf{J}_{HV}][R]^{-1}[P]^{*\top} \\ &= [P_\rho][P_\delta][R][\mathbf{J}_{HV}][R]^{-1}[P_\delta][P_\rho]^{-1} \end{aligned} \tag{6.24}$$

we see that it is not a diagonalisation equation, due to the influence of $[P_\delta]$. Note that on the right hand side we don't have its inverse, but the matrix itself.

A way of compensating the effect of $[P]$ would be simply to measure the antenna in order to obtain its value and invert it before diagonalising. That is, measure $[\mathbf{J}_{xy}]$, compute

$$[P]^{-1}[\mathbf{J}_{xy}][P]^{*\top^{-1}} = [R][\mathbf{J}_{HV}][R]^{-1} \tag{6.25}$$

and finally diagonalise the obtained matrix in order to get the eigenvalues of $[\mathbf{J}_{HV}]$.

Another approach could try to invert using the diagonalisation method without measuring $[P]$. Therefore it is useful to know what would be the accuracy of the obtained results. Equation (6.24) tells us that the eigenvalues of $[\mathbf{J}_{xy}]$ will

be different from that of $[\mathbf{J}_{HV}]$, because it represent *not* related by a similarity transform. Notice that on the right hand side of the product there is not the inverse of $[P_\delta]$. Let us see what will be the eigenvalues of $[\mathbf{J}_{xy}]$. We assume that the eigenvalues of $[\mathbf{J}_{HV}]$ are H and V. The eigenvalues of $[\mathbf{J}_{xy}]$ are the same as the eigenvalues of

$$[P_\delta]\,[\mathbf{J}_{HV}]\,[P_\delta] = \begin{bmatrix} \cos\delta & \sin\delta \\ \sin\delta & \cos\delta \end{bmatrix} \begin{bmatrix} H & 0 \\ 0 & V \end{bmatrix} \begin{bmatrix} \cos\delta & \sin\delta \\ \sin\delta & \cos\delta \end{bmatrix} \tag{6.26}$$

It has been taken into account that in (6.24) $[R]$ does not change the eigenvalues of $[\mathbf{J}_{HV}]$ because they are a similarity transform. The same happens with $[P_\rho]$. The eigenvalues are computed straightforward yielding

$$\lambda_1 = \frac{V+H}{2} + \frac{1}{2}\sqrt{(V+H)^2 - 2VH\,(1+\cos 4\delta)} \tag{6.27}$$

$$\lambda_2 = \frac{V+H}{2} - \frac{1}{2}\sqrt{(V+H)^2 - 2VH\,(1+\cos 4\delta)} \tag{6.28}$$

If the antenna is perfectly orthogonal from the polarisation point of view, $\delta = 0$ and thus the eigenvalues of equations (6.27) and (6.28) will be equal to the emitted values H and V.

The conclusion that can be drawn is that the proposed Faraday rotation correction method is robust to uncalibrated rotations of the antenna frame, but it is not to non-orthogonal antenna probes. This first part of the conclusion is obvious, as the proposed method is able to compensate any rotation between the emission frame and the antenna frame. The second part means that special care must be taken in the antenna design and manufacturing in order to assure that both antenna polarisation axes are orthogonal.

Chapter 7

Conclusions

This dissertation has tackled several aspects related to the calibration of MIRAS and its polarimetric mode of operation. In a first introductory part, the fundamentals of radiometry and the basic interferometric equations upon which the operation of MIRAS is based have been presented.

The thesis followed with a second part devoted to calibration aspects of MIRAS. Single power and two power noise injection methods have been reviewed, as well as comparators offset calibration. These calibration methods have been experimentally tested on different pieces of hardware.

The first experiments that were done with the LICEF-1 receiver and the correlator system DICOS-3 demonstrated the robustness of the 1&0 comparator offset correction. Quadrature and in-phase error calibration methods also proved to be valid. On the contrary, it was shown that amplitude calibration needed a further refinement. The shape of the fringe-washing function was also measured with the three delay method, showing good coincidence with the predicted values obtained from the front-end filter responses. The image validation test also showed the imaging capabilities of MIRAS at off-bore sight directions, where the impulsional response of MIRAS was measured. The obtained image showed a clear main lobe, part of the secondary lobes and the sky horizon.

The tests done with the HUT-2D hardware re-confirmed some of the previous results, particularly the 1&0 offset correction method and the quadrature and in-phase error calibrations. It was further demonstrated that it is better to obtain the quadrature error independently from the in-phase error as it yields better results and does not depend on the injected power. The quadrature error will thus be obtained from the self-correlation between in-phase and quadrature

components of each receiver.

The calibration experiments injecting cold noise allowed to experimentally confirm Bosma's noise theory, where the correlation amplitude depends on the difference between the injected temperature and the physical temperature of the NDN. The receiver failure experiment did also experimentally confirm the need of having a good isolation between the output ports of the NDN.

Preliminary results of the two-level noise injection method have also been presented. The designed and manufactured SAM EGSE, with full capability of implementing this novel calibration scheme, was used to calibrate a LICEF-2 receivers baseline using the DICOS-2 correlator. These preliminar results do re-confirm again the previous knowledge in 1&0 offset compensation method, the quadrature and in-phase error calibration, and they are the first experimental validation of the two-level four-point calibration method.

In the third part of the thesis the non-invertibility of the dual polarisation mode of MIRAS in some parts of its field of view has been tackled and a solution, consisting in the proposal of the full-polarimetric mode of MIRAS, has been given. It was shown that off-bore sight measurements result in a rotation of the effective antenna polarisation frame. As the dual-polarisation mode does an incomplete measurement of the polarisation state of the incident wave it is not capable of inverting the measurements at some parts of the field of view (where this rotation is equal to 45°). The fully polarimetric mode solves this problem by measuring the complete polarimetric brightness temperature matrix.

The interlacing scheme in the polarimetric mode of MIRAS has also been proposed in this thesis in order to overcome the synthetic beam distortion that appears when fully polarimetric measurements of a moving target with a single channel interferometer like MIRAS are done.

The polarimetric mode of MIRAS has also opened the door to new calibration methods. In particular, a simple mathematical method has been proposed for compensating the effect of the Faraday rotation, under the assumption that the target does have a negligible cross-correlation between the horizontal and vertical polarisations. The method consists of diagonalising the measured polarimetric brightness temperature matrix (with the polarimetric mode of MIRAS) obtaining the emitted power for the horizontal and vertical polarisations.

7.1 Future Work

Future research lines can be found in the two directions this dissertation points to, namely calibration related issues and polarimetric radiometry.

Related to the development of SAM, several measurement campaigns are foreseen in the near future. Anechoic chamber tests with SAM are planned in order to verify the two-level calibration method using natural targets. An open air campaign devoted to image with SAM the night sky and the Milky Way is expected to be done during 2005. After these tests, the array will be embarked in the Skyvan aircraft of HUT and some demonstrator flights with SAM will be done. The objective of these tests is to demonstrate SAM capabilities in measuring the brightness temperatures for sea water, lake water and differently moistured soil.

The polarimetric mode of MIRAS has not been tested yet. The availability of SAM and the planned campaigns will be an excellent opportunity for making the first polarimetric experiments with MIRAS.

Appendix A

Calibration Equations

In this appendix the calibration equations for the single temperature noise injection calibration are given.

In [26, 25] the equations relating the normalised equations at the output of the receiver and the normalised correlations at its input are given as

$$\begin{pmatrix} \mu_{ii} \\ \mu_{qi} \end{pmatrix} = \tilde{g}_{mn} \begin{bmatrix} \cos(\alpha_{mn} + Q_{mn}) & \sin(\alpha_{mn} + Q_{mn}) \\ -\sin(\alpha_{mn} + Q'_{mn}) & \cos(\alpha_{mn} + Q'_{mn}) \end{bmatrix} \begin{pmatrix} V_{Re} \\ V_{Im} \end{pmatrix} \quad (A.1)$$

$$\begin{pmatrix} \mu_{qq} \\ \mu_{iq} \end{pmatrix} = \tilde{g}_{mn} \begin{bmatrix} \cos(\alpha_{mn} - Q_{mn}) & \sin(\alpha_{mn} - Q_{mn}) \\ \sin(\alpha_{mn} - Q'_{mn}) & -\cos(\alpha_{mn} - Q'_{mn}) \end{bmatrix} \begin{pmatrix} V_{Re} \\ V_{Im} \end{pmatrix} \quad (A.2)$$

where the baseline gain factor $\tilde{g}_{mn}$ has been included. Equation (A.1) corresponds to the solution when using the μ_{ii} and μ_{qi} correlations; equation (A.2) to the redundant case with μ_{qq} and μ_{iq}.[1]

The normalised correlations on the right hand side of the equation, V_{Re} and V_{Im} represent the real and imaginary part of the measured normalised correlations if the receiver would be noiseless and with no phase errors, that is, at the input of the receiver. The angular terms are

$$\alpha_{mn} = \theta_n - \theta_m - \theta_{mn} \quad (A.3)$$

---

[1]Sub-indices m and n have been dropped from the measured normalised correlations $\mu_{i_m i_n}$, $\mu_{q_m i_n}$, $\mu_{q_m q_n}$ and $\mu_{i_m q_n}$ for simplicity in the notation. The first signal corresponds always to receiver m, while the second signal corresponds to receiver n, yielding the notation μ_{ii}, μ_{qi}, μ_{qq} and μ_{iq} for the measured normalised correlations.

$$Q_{mn} = \frac{1}{2}(\theta_{qn} - \theta_{qm}) \tag{A.4}$$

$$Q'_{mn} = \frac{1}{2}(\theta_{qn} + \theta_{qm}) \tag{A.5}$$

with θ_m, θ_n and θ_{qm}, θ_{qn} being the phase and quadrature errors of the receivers and θ_{mn2} the un-separable phase term of the baseline.

A.1   Quadrature Error

The quadrature error of each receiver can be obtained by cross-correlating the in-phase and quadrature signals of one receiver. If we say that $m = n$ in equations (A.1) and (A.2) we have that we are computing the correlations between signals of a single receiver. Thermal noise signals have always uncorrelated in-phase and quadrature components, thus, $V_{Im} = 0$ always, while $V_{Re} = 1$.[2] In such a case the equation can be simplified and the quadrature error can be obtained from

$$\mu_{i_m q_m} = -\sin\theta_{q_m} \tag{A.6}$$

where $\mu_{q_m i_m}$ is the cross correlation between the in-phase and quadrature components of receiver m [26].

A.2   In-phase error

The phase term α_{mn} of the baseline can be determined from (A.1) in the case we use the IIQI correlations. Breaking up the matrix notation and writing down the two equations we notice that taking the quotient of both we get rid of the gain term $\tilde{g}_{mn}$. This gain term will always be larger than zero. In fact, a gain term equal to zero would mean that our receivers have an infinite noise factor, which obviously would make any measurement impossible. The quotient yields

$$\frac{\mu_{ii}}{\mu_{qi}} = \frac{V_{Re}\cos(\alpha_{mn} + Q_{mn}) + V_{Im}\sin(\alpha_{mn} + Q'_{mn})}{-V_{Re}\sin(\alpha_{mn} + Q'_{mn}) + V_{Im}\cos(\alpha_{mn} + Q_{mn})} \tag{A.7}$$

multiplying by both numerators we obtain get

$$-\mu_{ii}V_{Re}\sin(\alpha_{mn} + Q'_{mn}) + \mu_{ii}V_{Im}\cos(\alpha_{mn} + Q'_{mn}) =$$
$$\mu_{qi}V_{Re}\cos(\alpha_{mn} + Q_{mn}) + \mu_{qi}V_{Im}\sin(\alpha_{mn} + Q_{mn}) \tag{A.8}$$

---

[2]Remember that these are *normalised* correlations.

Using the trigonometric formulas for angle sums and operating we can separate the in-phase terms from the quadrature ones yielding

$$
\sin\alpha_{mn}\left[-\mu_{ii}V_{Re}\cos Q'_{mn} - \mu_{ii}V_{Im}\sin Q'_{mn} + \mu_{qi}V_{Re}\sin Q_{mn} - \mu_{qi}V_{Im}\cos Q_{mn}\right] =
$$
$$
\cos\alpha_{mn}\left[\mu_{ii}V_{Re}\sin Q'_{mn} - \mu_{ii}V_{Im}\cos Q'_{mn} + \mu_{qi}V_{Re}\cos Q_{mn} + \mu_{qi}V_{Im}\sin Q_{mn}\right]
$$

$$(A.9)$$

The bracket on the left hand side of the equation can be re-written in a more compact form like

$$
-\mu_{ii}V_{Re}\cos Q'_{mn} - \mu_{ii}V_{Im}\sin Q'_{mn} + \mu_{qi}V_{Re}\sin Q_{mn} - \mu_{qi}V_{Im}\cos Q_{mn} =
$$
$$
\begin{pmatrix} V_{Re} & V_{Im} \end{pmatrix}
\begin{bmatrix} -\cos Q'_{mn} & \sin Q_{mn} \\ -\sin Q'_{mn} & \sin Q_{mn} \end{bmatrix}
\begin{pmatrix} \mu_{ii} \\ \mu_{qi} \end{pmatrix} =
$$
$$
\begin{pmatrix} V_{Re} & V_{Im} \end{pmatrix} [B]
\begin{pmatrix} \mu_{ii} \\ \mu_{qi} \end{pmatrix}
$$

$$(A.10)$$

while the bracket on the right hand side can be simplified with

$$
\mu_{ii}V_{Re}\sin Q'_{mn} - \mu_{ii}V_{Im}\cos Q'_{mn} + \mu_{qi}V_{Re}\cos Q_{mn} + \mu_{qi}V_{Im}\sin Q_{mn} =
$$
$$
\begin{pmatrix} V_{Re} & V_{Im} \end{pmatrix}
\begin{bmatrix} \sin Q'_{mn} & \cos Q_{mn} \\ -\cos Q'_{mn} & \sin Q_{mn} \end{bmatrix}
\begin{pmatrix} \mu_{ii} \\ \mu_{qi} \end{pmatrix} =
$$
$$
\begin{pmatrix} V_{Re} & V_{Im} \end{pmatrix} [A]
\begin{pmatrix} \mu_{ii} \\ \mu_{qi} \end{pmatrix}
$$

$$(A.11)$$

yielding

$$
\sin\alpha_{mn}\left(\mathbf{v}^T[B]\mu_{iiqi}\right) = \cos\alpha_{mn}\left(\mathbf{v}^T[A]\mu_{iiqi}\right)
$$

$$(A.12)$$

Putting all the terms with α_{mn} at one side of the equation we finally obtain the solution

$$
\tan\alpha_{mn} = \frac{\mathbf{v}^T[A]\mu_{iiqi}}{\mathbf{v}^T[B]\mu_{iiqi}}
$$

$$(A.13)$$

where we can obtain the in-phase error angle α_{mn} from the measured correlations, the correlations at the input of the receivers and the measured quadrature

errors, being

$$[A] \;=\; \begin{bmatrix} \sin Q'_{mn} & \cos Q_{mn} \\ -\cos Q'_{mn} & \sin Q_{mn} \end{bmatrix} \qquad\qquad \text{(A.14)}$$

$$[B] \;=\; \begin{bmatrix} -\cos Q'_{mn} & \sin Q_{mn} \\ -\sin Q'_{mn} & -\cos Q_{mn} \end{bmatrix} \qquad\qquad \text{(A.15)}$$

$$\mathbf{v}^T \;=\; \begin{pmatrix} V_{Re} & V_{Im} \end{pmatrix} \qquad\qquad\qquad\quad \text{(A.16)}$$

$$\mu_{iiqi} \;=\; \begin{pmatrix} \mu_{ii} \\ \mu_{qi} \end{pmatrix} \qquad\qquad\qquad\quad \text{(A.17)}$$

We can proceed in a similar way for the QQIQ correlations. In this case the in-phase error is obtained with

$$\tan \alpha_{mn} = \frac{\mathbf{v}^T [C] \mu_{qqiq}}{\mathbf{v}^T [D] \mu_{qqiq}} \qquad\qquad \text{(A.18)}$$

being

$$[C] \;=\; \begin{bmatrix} \sin Q'_{mn} & \cos Q_{mn} \\ \cos Q'_{mn} & -\sin Q_{mn} \end{bmatrix} \qquad\qquad \text{(A.19)}$$

$$[D] \;=\; \begin{bmatrix} \cos Q'_{mn} & -\sin Q_{mn} \\ -\sin Q'_{mn} & -\cos Q_{mn} \end{bmatrix} \qquad\qquad \text{(A.20)}$$

$$\mathbf{v}^T \;=\; \begin{pmatrix} V_{Re} & V_{Im} \end{pmatrix} \qquad\qquad\qquad\quad \text{(A.21)}$$

$$\mu_{iiqi} \;=\; \begin{pmatrix} \mu_{ii} \\ \mu_{qi} \end{pmatrix} \qquad\qquad\qquad\quad \text{(A.22)}$$

A.3   Gain factor

Gain factor   The gain factor $\tilde{g}_{mn}$ can be obtained from equation (A.1). Therefore the matrix containing the trigonometric terms has to be broken up into two matrices, one containing only quadrature error term and a second one containing only in-phase error terms. The matrix of equation (A.1) can be rewritten as

$$\begin{bmatrix} \cos(\alpha_{mn}+Q_{mn}) & \sin(\alpha_{mn}+Q_{mn}) \\ -\sin(\alpha_{mn}+Q'_{mn}) & \cos(\alpha_{mn}+Q'_{mn}) \end{bmatrix} \;=$$

$$\begin{bmatrix} \cos(Q_{mn}) & \sin(Q_{mn}) \\ -\sin(Q'_{mn}) & \cos(Q'_{mn}) \end{bmatrix} \begin{bmatrix} \cos(\alpha_{mn}) & \sin(\alpha_{mn}) \\ -\sin(\alpha_{mn}) & \cos(\alpha_{mn}) \end{bmatrix} \;=$$

$$[M_Q] \, [M_\alpha] \qquad\qquad\qquad\qquad \text{(A.23)}$$

being M_Q the matrix containing the quadrature terms and M_α the matrix with the in-phase terms. Thus equation (A.1) can be rewritten in a more compact form as

$$\mu_{iiqi} = \tilde{g}_{mn} [M_Q] [M_\alpha] \mathbf{V} \tag{A.24}$$

The quadrature error matrix can be moved to the left hand side of the equation yielding

$$[M_Q]^{-1} \mu_{iiqi} = \tilde{g}_{mn} [M_\alpha] \mathbf{V} \tag{A.25}$$

were $[M_Q]^{-1}$ can be computed easily

$$[M_Q]^{-1} = \frac{1}{\cos(Q'-Q)} \begin{bmatrix} \cos Q' & -\sin Q \\ \sin Q' & \cos Q \end{bmatrix} \tag{A.26}$$

The matrix equation (A.25) can be expressed as two equations. This gives

$$\mu_{ii} \cos Q' - \mu_{qi} \sin Q = \tilde{g}_{mn} \cos(Q'-Q) [V_{Re} \cos \alpha + V_{Im} \sin \alpha] \tag{A.27}$$
$$\mu_{ii} \sin Q' + \mu_{qi} \cos Q = \tilde{g}_{mn} \cos(Q'-Q) [-V_{Re} \sin \alpha + V_{Im} \cos \alpha] \tag{A.28}$$

If both equations are squared and added together, after some simplification the result for $\tilde{g}_{mn}$ is obtained

$$\tilde{g}_{mn}^2 = \frac{\mu_{ii} + \mu_{qi} + 2\mu_{ii}\mu_{qi} \sin(Q'-Q)}{(V_{Re}^2 + V_{Im}^2) \cos^2(Q'-Q)} \tag{A.29}$$

Exactly the same result is obtained when equation (A.2) is used and proceeded in the same way.

From the above equations (A.6), (A.13), (A.18) and (A.29), it can be seen that all calibration parameters (quadrature errors, in-phase errors and gain factor) of each baseline can be obtained, independently of the input correlation. The quadrature error is obtained from the cross correlation between the in-phase and quadrature signal of each receiver. This can be done for any input signal it is not necessary to have noise injection, even for antenna measurements this can be done.

The in-phase error of the baseline can be obtained from the measurements (μ_{iiqi} or μ_{qqiq}), the estimated quadrature errors and the correlation of the noise at the input of the receivers (V_{Re} and V_{Im}). This input correlation during noise injection can be obtained using Bosma's noise theory [31], which is revised in appendix B.

Finally, the gain factor $\tilde{g}_{mn}$ of the baseline can be obtained from the measurements (μ_{iiqi} or μ_{qqiq}), the estimated quadrature errors and the correlation

of the noise at the input of the receivers (V_{Re} and V_{Im}). As for the in-phase error the correlation at the input of the receivers during noise injection can be obtained using Bosma's noise theory.

Note that in-phase errors and gain factors can be obtained individually from each other. This is coherent with their physical origin. The in-phase error is caused by the phase of the local oscillator of the receiver, while the gain factor is due to the receiver noise.

Note also that it is necessary to know the quadrature error of the receivers, in order to be able to estimate the in-phase error and the gain factor. In fact, we are observing a two dimensional signal (in-phase and quadrature components). These components are orthogonal (zero cross-correlation between them) as the signal has its origin in thermal noise. We are observing them with our demodulated in-phase and quadrature components, which are not the same due to the quadrature and in-phase errors. The quadrature error makes that we observe the signal space in a non orthogonal basis and thus the space seems deformed. This deformation has to be taken into account, and it is why the quadrature error of the receivers appear in equations (A.13), (A.18) and (A.29). On the contrary the phase error does only rotate the space without transforming it. This is the reason why the in-phase error does not appear in equation (A.29).

Appendix B

Effect of the NDN on Phase and Amplitude Calibration

Calibration in HUT-2D and MIRAS has been defined using a hot noise source at the input of the Noise Distribution Network in order to inject correlated noise at input the receivers. Bosma shows in his thesis [31] that correlated noise coming out of a passive multi-port can be generated just by having its terminations connected to matched loads at different physical temperature. The condition for no correlation between the output signals is that the matched loads have to be at the same physical temperature as the multi-port. Correlated noise can be obtained with only one of the ports being at a different physical temperature, higher or lower than the physical temperature of the network. Non-perfect matching results also in correlated noise at the output of the multi-port.

B.1 Noise Correlation Matrix of Linear Passive Multi-Ports

In this section Bosma's approach is reviewed shortly to provide to the reader a better insight of the problem.

A passive linear multi-port S, operating at a single frequency, or within a narrow band, is perfectly described by its scattering matrix $[S]$. Its ports can be connected to another passive linear multi-port Q defined by a scattering matrix $[Q]$. Both multi-ports have $N + 1$ ports numbered from zero to N.

Figure B.1 shows the multi-port S with its terminations connected to the multi-port Q. The noise waves generated by the S network are described by the vector $\mathbf{X} = (x_0, x_1, \ldots, x_N)^\top$, being x_j the output noise-wave amplitude of port j. The correlation between these waves is described by the noise-wave power matrix $[G]$

$$[G] = \mathbf{X}\mathbf{X}^\times \tag{B.1}$$

where $^\times$ means conjugate transpose. It is clear that the matrix $[G]$ is hermitian. The noise waves generated by the Q network are equivalently described by $\mathbf{Y} = (y_0, y_1, \ldots, y_N)^\top$, being y_j the output noise-wave amplitude of port j. The correlation between the output noise-waves is given by

$$[H] = \mathbf{Y}\mathbf{Y}^\times \tag{B.2}$$

$[H]$ is also a hermitian matrix. The diagonals of $[G]$ and $[H]$ will be the power that is output at each port. The off-diagonal elements represent the correlation between the output noise of two different ports.

A reasonable assumption is to suppose that the noise waves generated by the different multi-ports are uncorrelated as they have their thermal origin at different circuits. Thus

$$\mathbf{X}\mathbf{Y}^\times = 0 \tag{B.3}$$

The noise waves $\mathbf{A}$ and $\mathbf{B}$ which transport energy between both multi-ports, will be the sum of the output waves and the scattered waves by the multi-ports.
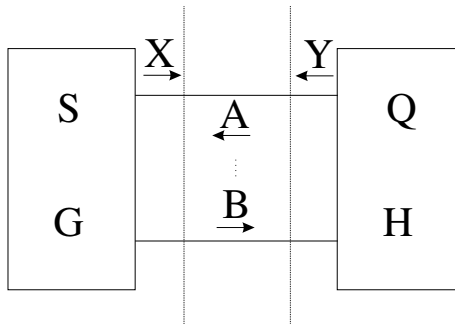

Figure B.1: Linear passive multi-port S terminated with another linear passive multi-port Q.

This can be written as

$$\mathbf{A} \;=\; \mathbf{Y} + [Q]\,\mathbf{B} \tag{B.4}$$
$$\mathbf{B} \;=\; \mathbf{X} + [S]\,\mathbf{A} \tag{B.5}$$

The correlation between the incident $\mathbf{A}$ waves on the multi-port S can be computed directly yielding the correlation matrix

$$\mathbf{A}\mathbf{A}^{\times} = ([I] - [Q]\,[S])^{-1}([H] + [Q]\,[G]\,[Q]^{\times})([I] - [S]^{\times}\,[Q]^{\times})^{-1} \tag{B.6}$$

where $[I]$ is the identity matrix. Similarly for the $\mathbf{B}$ waves incident on the Q multi-port its correlation matrix is

$$\mathbf{B}\mathbf{B}^{\times} = ([I] - [S]\,[Q])^{-1}([G] + [S]\,[H]\,[S]^{\times})([I] - [Q]^{\times}\,[S]^{\times})^{-1} \tag{B.7}$$

The correlation between the waves $\mathbf{A}$ travelling in opposite direction respect to the $\mathbf{B}$ waves can also be computed directly obtaining

$$\mathbf{A}\mathbf{B}^{\times} = ([I] - [Q]\,[S])^{-1}([Q]\,[G] + [H]\,[S]^{\times})([I] - [Q]^{\times}\,[S]^{\times})^{-1} \tag{B.8}$$

It is clear from equations (B.6) to (B.8) that the correlation between the noise waves travelling in both directions can be computed from the original correlation of the source waves $\mathbf{X}$ and $\mathbf{Y}$ and knowing the scattering parameters of both multi-ports.

The question that arises at this point is how the power and the correlation of the source-waves can be computed. This problem has already been solved by Bosma [31]. The internally generated noise-waves can be computed with

$$[G] = \mathbf{X}\mathbf{X}^{\times} = k_B T_{phys}\,[N_S] \tag{B.9}$$

where k_B is the Boltzmann constant, T_{phys} the physical temperature of the multi-port (at constant temperature) and $[N_S]$ the noise matrix of multi-port S defined as

$$[N_S] = [I] - [S]\,[S]^{\times} \tag{B.10}$$

If multi-port Q is at the same constant temperature

$$[H] = \mathbf{Y}\mathbf{Y}^{\times} = k_B T_{phys}\,[N_R] \tag{B.11}$$

with

$$[N_S] = [I] - [Q]\,[Q]^{\times} \tag{B.12}$$
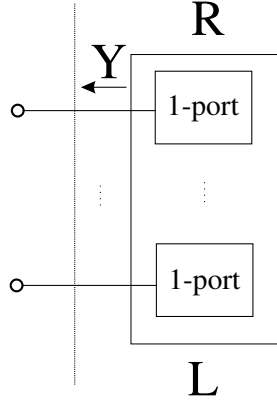
Figure B.2: Diagonal linear passive multi-port with scattering matrix $[R]$ and noise-wave power matrix $[L]$.

Bosma defines also the diagonal multi-port. Its model is shown in figure B.2. It consists in a series of 1-ports, which do not have any interaction among them. The scattering matrix $[R]$ of a diagonal multi-port is thus diagonal. The elements of the diagonal are the matching of each port.

$$[R] = \text{diag}(\rho_i) \tag{B.13}$$

with $i = 0, \ldots N$. The noise distribution matrix of a diagonal port will be also diagonal.

$$[N_R] = [I] - [R][R]^{\times} = \text{diag}(1 - \rho_i \rho_i^*) \tag{B.14}$$

To reckon the noise-wave power matrix the physical temperature of each 1-port can be taken into account, being thus, the noise-power matrix of a diagonal multi-port

$$[L] = k_B [T][N_R] \tag{B.15}$$

with

$$[T] = \text{diag}(T_i) \tag{B.16}$$

holding on its diagonal the equivalent noise temperatures of each port of R.

B.2   NDN Model Using Bosma's Approach

The NDN of the calibration system of HUT-2D is a linear passive network that can be perfectly characterised by its scattering matrix $[S]$. Each port is connected to a 1-port, the input of the NDN to the noise source and each output port to a receiver. So the model of the diagonal multi-port can be used as the termination of the NDN. The setup in that case can be seen in figure B.3. In order to use Bosma's expressions not only the scattering parameters of the NDN have to be measured but also the ones of the diagonal multi-port R, that is, the matching of the 1-ports forming the network R. Once both networks have been characterised only the equivalent temperatures of the 1-ports forming the network R have to be known. The equivalent temperature for port zero will be the equivalent noise temperature provided by the noise source. The equivalent temperature of the other ports will be their physical temperature.
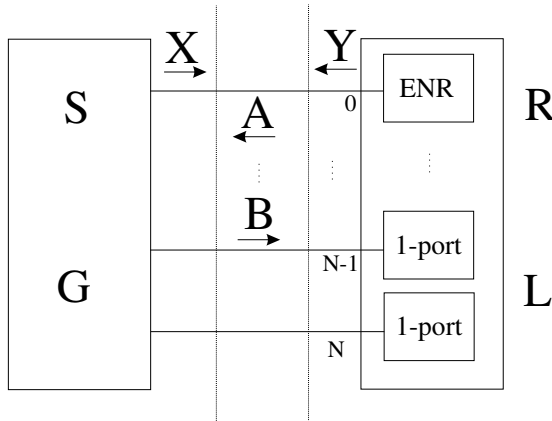

Figure B.3: Noise distribution network connected to an equivalent diagonal linear passive multi-port.

Appendix C

Publications, Conferences and Others

C.1 Papers

Ignasi Corbella, Francesc Torres, Adriano Camps, Andreas Colliander Manuel Martín-Neira, Serni Ribó, Kimmo Rautiainen, Nuria Duffo and Mercè Vall-llossera: *MIRAS End-to-End Calibration: Application to SMOS L1 Processor*, Transactions on Geoscience and Remote Sensing, vol. 43, no. 5, pp. 1126-1134, May 2005.

Serni Ribó and Manuel Martín-Neira: *Faraday Rotation Correction in the Polarimetric Mode of MIRAS*, Transactions on Geoscience and Remote Sensing, vol. 42, no. 7, pp. 1405-1410, July 2004.

Manuel Martín-Neira, Serni Ribó and Arturo Martín-Polegre: *Polarimetric Mode of MIRAS*, IEEE Transactions on Geoscience and Remote Sensing, vol. 40, no. 8, pp. 1755-1768, August 2002.

M. Martín-Neira, P. Piironen, S. Ribó, E. Panaro, J. Font-Roselló, J. Martí-Canales, I. Zayer, A. Martín-Polegre, P. Iversen, A. Rivada, R. Roumeas, M. Aguirre, P. Silvestrin: *The MIRAS demonstrator Pilot Project - Towards SMOS*, ESA Bulletin, no 111, August 2002.

C.2 Conference Papers

S. Ribó, M. Martín-Neira, F. Torres: *Faraday rotation correction using the polarimetric brightness temperature matrix*, Microrad'04, February 2004, Rome.

M. Martín-Neira, S. Ribó, K. Rautiainen: *0-1 Correction of Comparator Threshold in 1-bit Interferometric Radiometers*, Microrad'04, February 2004, Rome.

S. Ribó, M. Martín-Neira, L. Sempere: *Calibration of the Impulsional Response of a Small MIRAS*, SP-525 - EuroSTARRS, WISE, LOSAC Campaigns First Result Workshop, ESA Publications Division, March 2003.

J. Lahtinen, S. Ribó, M. Martín-Neira, and L. Sempere: Two-dimensional Interferometric Radiometry: Image Validation Using Celestial Objects, Proceedings of the IEEE International Geoscience and Remote Sensing Symposium, II: 1229 - 1231, July 2003, Toulouse, France.

C.3 Posters

F. Torres, N. Duffo, I. Corbella, A. Camps, M. Vall-llosera, S. Ribó: *MIRAS-SMOS, the Relative Instrumental Error Correction Approach*, Microrad'04, feb 2004, Rome.

S. Ribó, K. Rautiainen, J. Kainulainen, M. Hallikainen, M. Martín-Neira: *The effect of Receiver Failure in Noise Injection Calibration in HUT-2D and MIRAS*, 4th SMOS Workshop, March 2003, Oporto, Portugal.

C.4 Reports

Serni Ribó: *Detailed Design. MDPP-3 Electric Ground Support Equipment (EGSE) version 1.1.* May 2005. IEEC.

Serni Ribó: *User Manual. MDPP-3 Electric Ground Support Equipment (EGSE) version 1.1.* May 2005 IEEC.

Serni Ribó: *Research on Image Validation and Signal Processing of Aperture Synthesis Radiometry. Internal ESTEC Working Paper No. 2182*, January 2003, ESTEC, ESA.

Serni Ribó: *Research on HUT-2D. Internal paper*, October 2002. LST/HUT.

M. Martín-Neira, S. Ribó, A. Martín-Polegre: *Introduction to Two-dimensional Aperture Synthesis Microwave Radiometry for Earth Observation: Polarimetric Formulation of the Visibility Function. Internal ESTEC Working Paper no 2130*, October 12th, 2001. ESTEC, ESA.

C.5   Awards

Second Price from the Associació Catalana de Comunicació Científica to the popular science paper 2003: *El desenvolupament de MIRAS.*

Bibliography

[1] J. T. Houghton, Y. Ding, D. J. Griggs, , M. Noguer, P. J. van der Linden, X. Dai, K. Maskell, and C. A. Johnson, editors. *Climate Change 2001: The Scientific Basis*. Cambridge University Press, 2001.

[2] Yann Kerr, Jordi Font, Philippe Waldteufel, and Michael Berger. The Second of ESA's Opportunity Missions: The Soil Moisture and Ocean Salinity Mission - SMOS. *Earth Observation Quarterly*, (66):18–26, 2000.

[3] Michael Berger, Adriano Camps, Jordi Font, Yann Kerr, Jerry L Miller, J. Johannessen, Jaquelin Boutin, Mark R.Drinkwater, Niels Skou, Nicolas Floury, M. Rast, H. Rebhan, and E. Attema. Measuring Ocean Salinity with ESA's SMOS Mission - Advancing the Science. *ESA Bulletin*, (111):113–121, 2002.

[4] Michael Berger, Yann Kerr, Jordi Font, Jean-Pierre Wigneron, Jean-Christophe Calvet, Kauzar Saleh, Ernesto López-Baeza, Lester Simmonds, Paolo Ferrazzoli, Bart van den Hurk, Philippe Waldteufel, Francois Peticolin, Adriaan van de Griend, Evvert Attema, and Michael Rast. Measuring the Soil Moisture in the Earth's Soil - Advancing the Science with ESA's SMOS Mission. *ESA Bulletin*, (115):40–45, August 2003.

[5] Adriano Camps. *Application of Interferometric Radiometry to Earth Observation*. PhD thesis, Dept. Teoria del Senyal i Comunicacions, Universitat Politècnica de Catalunya, November 1996.

[6] Karl G. Jansky. Electrical Distrubances Apparently of Extraterrestrial Origin. *Proc. IRE*, 1933.

[7] Grote Reber. Cosmic static. *Astrophysical Journal*, 100:279, 1944.

[8] P. J. Napier, A. R. Thompson, and R. D. Ekers. The Very Large Array - Design and performance of a modern synthesis radio telescope. *IEEE Proceedings*, 71:1295–1320, November 1983.

[9] A.W. Straiton, C.W. Tolbert, and C.O. Britt. Apparent Temperatures of Some Terrestrial Materials and the Sun at 4.3-Millimeter Wavelenths. *Journal of Applied Physics*, 1958.

[10] Fawwaz T. Ulaby, Richard K. Moore, and Adrian K. Fung. *Mircrowave Remote Sensing*, volume 1, chapter 1, pages 12–17. Artech House Inc., 1981.

[11] Christopher S. Ruf, Calvin T. Swift, Alan B. Tanner, and David M. Le Vine. Interferometric Synthetic Aperture Microwave Radiometry for the Remote Sensing of the Earth. *IEEE Transactions on Geoscience and Remote Sensing*, 26(5):597–611, September 1988.

[12] David M. Le Vine, Andrew J. Griffis, Calvin T. Swift, and Thomas J. Jackson. Estar: A Synthetic Aperture Microwave Radiometer for Remote Sensing Applications. *Proceedings of the IEEE*, 82(12):1787–1801, December 1994.

[13] Thomas J. Jackson, David M. Le Vine, Ann Y. Hsu, Anna Oldak, Patrick J. Starks, Calvin T. Swift, John D.Isham, and Michael Haken. Soil Moisture Mapping at Regional Scales Using Microwave Radiometry: The Southern Great Plain Hydrology Experiment. *IEEE Transactions on Geoscience and Remote Sensing*, 37(5):2136–2151, September 1999.

[14] David M. Le Vine, Thomas J. Jackson, Calvin T.Swift, Michael Haken, and Steven W. Bidwell. ESTAR Measurements During the Southern Great Plains Experiment (SGP99). *IEEE Transactions on Geoscience and Remote Sensing*, 39(8):1680–1685, August 2001.

[15] David M. Le Vine, Calvin T. Swift, and Michael Haken. Development of the synthetic aperture microwave radiometer. *IEEE Transactions on Geoscience and Remote Sensing*, 39(1):199–202, January 2001.

[16] David M. Le Vine, Michael Haken, and Calvin T. Swift. Development of the Synthetic Aperture Radiometer ESTAR and the Next Generation. In *Geoscience and Remote Sensing Symposium, 2004. IGARSS '04. Proceedings.*, pages 1260 – 1263. IEEE International, 20-24 Sept 2004 2004.

[17] Bjorn Lambrigtsen, William Wilson, Alan Tanner, Todd Gaier, Cris Ruf, and Jeff Piepmeier. GeoSTAR - A Microwave Sounder for Geostationary Satellites. In *Geoscience and Remote Sensing Symposium, 2004. IGARSS '04. Proceedings.*, volume 2. IEEE International, 20-24 Sept. 2004.

[18] Fawaz T. Ulaby, Richard K. Moore, and Adrian K. Fung. *Mircrowave Remote Sensing*, volume 1, chapter 4, pages 186–255. Artech House Inc., 1981.

[19] Manuel Martín-Neira, Serni Ribó, and Arturo Martín-Polegre. Introduction to Two-Dimensional Aperture Syntheris Microwave Radiometry for Earth Observation: Polarimetric Formulation of the Visibility Function. Technical Report 2130, ESTEC, ESA, October 2001.

[20] M. Martín-Neira, S. Ribó, and A. Martín-Polegre. Polarimetric Mode of MIRAS. *IEEE Transactions on Geoscience and Remote Sensing*, 40(8):1755–1762, August 2002.

[21] A. C. Ludwig. The definition of cross polarization. *IEEE Transactions on Atennas and Propagation*, January 1973.

[22] Ignasi Corbella, Nuria Duffo, Mercè Vall-llosera, Adriano Camps, and Francesc Torres. The visibility function in interferometric aperture synthesis radiometry. *IEEE Transactions on Geoscience and Remote Sensing*, 2004.

[23] Francesc Torres, Adriano Camps, Javier Bará, and Ignasi Corbella. Impact of receiver errors on the radiometric resolution of large two-dimensional aperture synthesis radiometers. *Radio Science*, 32(2):629–642, March-April 1997.

[24] Ignasi Corbella, Adriano Camps, Miguel Zapata, Fernando Marcos, Francisco Martínez, Francesc Torres, Mercé Vall-llossera, Nuria Duffo, and Javier Bará. End-to-end simulator of two-dimensional interferometric radiometry. *Radio Science*, 32(3):MAR 32–1, 2002. 8058.

[25] F. Torres, A. Camps, J. Bará, I. Corbella, and R. Ferrero. On-board Phase and Modulus Calibration of Large Aperture Synthesis Radiometers: Study Applied to MIRAS. *IEEE Transactions on Geoscience and Remote Sensing*, 34(4):1000–1009, July 1996.

[26] J. Bará, A. Camps, J. Capdevila, I. Corbella, and F. Torres. MIRAS Calibration System Definition and Interference Analysis (CAS-D). Technical report, Universitat Politècnica de Catalunya, May 1998.

[27] M. Martín-Neira. Review of Offset Correction. Technical report, ESTEC, ESA, 2001.

[28] Adriano Camps, Francesc Torres, Ignasi Corbella, Javier Bará, and J. A. Lluch. Threshold and timing errors of 1 bit/2 level digital correlators in earth observation synthetic aperture radiometry. *IEEE Electronics Letters*, 33(9):812–814, April 1997.

[29] S. Ribó. Research on Image Validation and Signal Processing of Aperture Synthesis Radiometry. Internal ESTEC Working Paper. Technical Report 2182, ESTEC, ESA, January 2003.

[30] Manuel Martín-Neira, Serni Ribó, and Kimmo Rautiainen. 0-1 Correction of Comparator Treshold in 1-bit Interferometric Radiometers. In *Proceedings MicroRad '04 Conference*, Rome, February 2004.

[31] H. Bosma. *On the Theory of Linear Noisy Systems*. PhD thesis, Technische Hogeschool te Eindhoven, January 1967.

[32] Serni Ribó, Manuel Martín-Neira, and Luis Sempere. Calibration of the Impulsional Response of a Small MIRAS. In *First Results Workshop: EuroSTARRS, WISE, LOSAC*, number SP-525, pages 191–195. CESBIO, France, ESA, November 2002.

[33] Janne Lahtinen, Serni Ribó, Manuel Martín-Neira, and Luis Sempere. Two-dimensional interferometric radiometry: Image validation using celestial objects. In *Proceedings of the IEEE International Geoscience and Remote Sensing Symposium*, pages 1129–1131, 2003.

[34] UPC & EADS-CASA. Image Validation Test Report. Technical report, UPC & EADS-CASA.

[35] Francesc Torres, Nuria Duffo, Ignasi Corbella, Adriano Camps, Mercè Vall-llossera, and Serni Ribó. MIRAS-SMOS, the relative instrumental error correction approach. In *Proceedings Microrad '04 Conference*, Rome, February 2004.

[36] Ignasi Corbella, Francesc Torres, Adriano Camps, Andreas Colliander, Manuel Martín-Neira, Serni Ribó, Kimmo Rautiainen, Nuria Duffo, and Mercè Vall-llossera. MIRAS end-to-end calibration. Application to SMOS L1 processor. *IEEE Transactions on Geoscience and Remote Sensing*, 43(5):1126–1134, May 2005.

[37] Petri Piironen. PMS offset determination using an IF attenuator. Technical report, ESA-ESTEC, 2002.

[38] Ignasi Corbella, Adriano Camps, Francesc Torres, and Javier Bará. Analysis of noise-injection networks for interferometric-radiometer calibration. *IEEE Transactions on Geoscience and Remote Sensing*, 48(4):545–552, April 2000.

[39] J. B. Hagen and D. T. Farley. Digital-correlation techniques in radio science. *Radio Science*, 8(8-9):775–784, 1973.

[40] J. Meeus. *Astronomical Algorithms*. Willmann-Bell, 2nd edition, 1999.

[41] Adriano Camps, Francesc Torres, Javier Bará, Ignasi Corbella, and F. Monzón. Automatic calibration of channels frequency response in interferometric radiometers. *Electronic Letters*, 35(2):115–116, January 1999.

[42] R. Butora, M. Martín-Neira, and Angel-Luis Rivada-Antich. Fringe-washing function calibration in aperture synthesis microwave radiometry. *Radio Science*, 38(2), April 2003.

[43] Kimmo Rautiainen, H. Valmu, P. Jukkala, G. Moren, and Martti Hallikainen. Four-Element Prototype of HUT Interferometric Radiometer. In IEEE International, editor, *Geoscience and Remote Sensing Symposium, 1999. IGARSS '99 Proceedings*, volume 1, pages 234–236, 1999.

[44] Kimmo Rautiainen, Robert Butora, Tuomo Auer, N. Mononen, J. Salminen, Simo Tauriainen, Martti Hallikainen, Josu Uusitalo, and P. Jukkala. The Helsinki University of Technology/Ylinen Electronics Airborne L-band Interferometric Radiometer. In IEEE International, editor, *Geoscience and Remote Sensing Symposium, 2000. Proceedings IGARSS 2000.*, volume 7, pages 2978–2980, 2000.

[45] Serni Ribó. Detailed Design MDPP-3 EGSE. Technical report, Institut d'Estudis Espacials de Catalunya (IEEC), 2005. ver 1.0.

[46] Serni Ribó. User Manual MDPP-3 EGSE. Technical report, Institut d'Estudis Espacials de Catalunya (IEEC), 2005. ver 1.0.

[47] Manuel Martín-Neira and Quiterio García. Pol-switching: Switching Scheme for Single Channel Polarimetric Aperture Snthesis Radiometers. Technical Report 2062, ESTEC, ESA, December 1999.

[48] David M. Le Vine and Saji Abraham. The Effect of Ionosphere on Remote Sensing of Sea Surface Salinity From Space: Absorption and Emission at L Band. *IEEE Transactions on Geoscience and Remote Sensing*, 40(4):771–782, April 2002.

[49] Simon H. Yueh, Richard West, William J. Wilson, Fuk K. Li, Eni G Njoku, and Yahya Rahmat-Samii. Error sources and feasibility for microwave remote sensing of ocean surface salinity. *IEEE Transactions on Geoscience and Remote Sensing*, 39(5):1049–1060, May 2001.

[50] A. Camps, N. Duffo, M. Vall-llosera, and B. Vallespín. Sea surface salinity retrieval using multi-angular L-band radiometry: Numerical study using the smos end-to-end performance simulator. In *Proceedings of the IEEE International Geoscience and Remote Sensing Symposium*, volume 2, pages 1367–1369, June 2002.

[51] Simon H. Yueh. Estimates of Faraday rotation with passive microwave polarimetry for microwave remote sensing of earth surfaces. *IEEE Transactions on Geoscience and Remote Sensing*, 38(5):2434–2438, September 2000.

[52] Niels Skou. Faraday rotation and L-band oceanographic measurements. *Radio Science*, 38(4), 2003.

[53] Sten Schmidl Søbjærg and Niels Skou. An airborne campaign measuring wind signatures from sea surface using an L-band polarimetric radiometer. In *Proceedings of the IEEE International Geoscience and Remote Sensing Symposium*, volume 4, pages 2738–2740, July 2003.

[54] J. H. Wilkinson. *The Algebraic Eigenvalue Problem*. Oxford University Press, 1992.

[55] Sten Schmidl Søbjærg and Niels Skou. Polarimetric signatures from a crop covered land surface measured by an L-band polarimetric radiometer. In *Proceedings of the IEEE International Geoscience and Remote Sensing Symposium*, volume 4, pages 2626–2628, July 2003.

[56] Fawaz T. Ulaby, Richard K. Moore, and Adrian K. Fung. *Mircrowave Remote Sensing*, volume 1, chapter 4, pages 229–232. Artech House Inc., 1981.

[57] Sebastián Blanch and Albert Aguasca. Dielectric permittivity measurements of sea water. In *SP-525- EuroSTARSS, WISE, LOSAC Campaigns*, pages 137–141. ESTEC, ESA, nov 2002.

[58] Fawaz T. Ulaby, Richard K. Moore, and Adrian K. Fung. *Mircrowave Remote Sensing*, volume 1, chapter 5, pages 256–343. Artech House Inc., 1981.

[59] Dieter Bilitza. International reference ionosphere 2000. *Radio Science*, 36(2):261–275, 2001.

[60] National Space Science Data Center. International geomagnetic reference field - epoch 2000. Revision of the IGRF for 2000-2005. http://www.ngdc.noaa.gov/IAGA/wg8/igrf.html.

[61] Adriano Camps, Javier Bará, Ignasi Corbella, and Francesc Torres. The processing of hexagonally sampled signals with standard rectangular techniques: Application to 2-D large aperture synthesis interferometric radiometers. *IEEE Transactions on Geoscience and Remote Sensing*, 35(1):183–190, January 1997.

[62] Adriano Camps, Ignasi Corbella, Javier Bará, and Francesc Torres. Radiometric sensitivity computation in aperture synthesis interferometric radiometry. *IEEE Transactions on Geoscience and Remote Sensing*, 36(2):680–685, March 1998.